Dynamic modelling of radar seaclutter

Dynamic modelling of radar seaclutter

Proefschrift

ter verkrijging van de graad van doctor
aan de Technische Universiteit Delft,
op gezag van de Rector Magnificus prof. dr. ir. J.T. Fokkema,
voorzitter van het College voor Promoties,
in het openbaar te verdedigen op vrijdag 17 november 2006 om 10.00 uur
door

Herman Willem MELIEF

doctorandus sterrenkunde
geboren te Huissen

Dit proefschrift is goedgekeurd door de promotoren:

Prof. ir. P. van Genderen
Prof. ir. P. Hoogeboom

Samenstelling promotiecommissie:

Rector Magnificus,	Voorzitter
Prof. ir. P. van Genderen,	Technische Universiteit Delft, promotor
Prof. ir. P. Hoogeboom,	Technische Universiteit Delft, promotor
Prof. dr. S. Watts,	University College London
Prof. dr. G.J. Komen,	Universiteit Utrecht
Prof. dr. ir. A.P.M. Zwamborn,	Technische Universiteit Eindhoven
Prof. dr. ir. G.S. Stelling,	Technische Universiteit Delft
Dr. H.S.F. van Wimersma Greidanus,	EC Joint Research Centre (JRC)

This research was supported by TNO Defence, Security, and Safety.

ISBN-10: 90-9021172-1

ISBN-13: 978-90-9021172-5

Cover design by H.W. Melief

Contents

Chapter 1

Introduction

1.1 Background

Since the end of the Cold War, naval operations have increasingly shifted from open ocean to littoral water. As the locations shifted, so have the mission tasks. During the Cold War most missions were focused on the threat from large naval vessels on the open ocean. Most radar systems were designed with these types of environments and targets in mind: systems capable of monitoring large stretches of surrounding ocean surface. As such, these types of systems often have low resolution, both in space and time.

Current operations, which are increasingly perfomed in coastal regions, have other goals: for instance peacekeeping missions and the monitoring of illegal activities, such as piracy and drug trafficking. These missions all have one demand in common: the need to detect small and/or weak (SW) targets on the ocean surface. For most coastal operations the risk from such targets is significant. Near the coast fishing boats and floating debris present objects that need to be evaded. Otherwise, monitoring of illegal activities often involves SW targets, as pirates and drug-smugglers mostly use small ships. Moreover, in recent years terrorist threats make scenarios involving attacks from small boats more likely. Because of the proximity of the coast, the region that needs to be monitored is often smaller, but tends to be more complex.

Summarising, the shift from blue to brown water operations means a shift from the detection of large targets over very long distances to the detection of SW targets over medium and short distances. This has led to the formulation of new requirements for radar systems by the Royal Netherlands Navy (KM). TNO Defensie en Maatschappelijke Veiligheid (TNO-DMV), formerly TNO Fysisch en Electron-

isch Laboratorium (TNO-FEL), is trying to support the KM in fulfilling this need through a number of projects. One of these projects is the project Model Hoge Resolutie Zeeclutter (MHRZC), i.e. Model High Resolution Seaclutter, which has formed the basis of this thesis. The aim of this project is to improve models of radar reflections from the ocean surface, i.e. radar seaclutter, to aid in the detection of SW targets against a background of seaclutter. Due to the fact that the project is aimed at naval operations, the radar wavelengths used in this thesis are restricted to 1 to 10 GHz. Moreover, as naval radar observations are made at the ocean surface, the physical parameters that are used in this thesis are assumed to have values standard for this domain.

This project ties in with one of the main problems with detecting SW targets on the sea surface. The nature of these targets requires the improvement of both the resolution and the sensitivity of detection systems. Apart from the technical issues of designing such systems, it also gives rise to an observational problem. At high resolutions and sensitivities reflections from the ocean surface itself start playing an important role. This may lead to two problems from a detection point of view. Firstly, the SW targets may be weak enough to disappear in the background. Secondly, the clutter can lead to 'false' alarms, i.e. events on the ocean surface may falsely be identified as targets. To improve detection and reduce false alarm rates it is important to be able to distinguish between the targets and the clutter. For that purpose, a better understanding and good models of the clutter are necessary, which is the main goal of this thesis. From this aim follow the thesis objectives:

1. Identify the gaps in knowledge of seaclutter through a literature study.
2. Build a comprehensive seaclutter model that fills these gaps.
3. Validate the model through a comparison with radar seaclutter data.

The first objective is treated in the next section as well as in chapters 2 and 3. The second and third objectives are expanded upon in section 1.3 and will be taken up in chapters 4 through 7.

1.2 Seaclutter research

Radar seaclutter research can be roughly divided into three categories, observations, statistical (empirical) modelling and analytical modelling. The first category measures the ocean surface with a radar system and, if available, a number of supporting instruments such as wave buoys, lidars or optical and infrared cameras. The so-recorded data are interpreted and theories about the nature of the clutter are deduced. This is treated in more detail in section 1.2.1.

As mentioned above, there are two types of models, statistical and analytical. The first type of model tries to describe the nature of seaclutter as a statistical distribution where both the longer periodic features and the shorter spikiness are taken into account, see for instance [64, 98, 110, 111]. Analytical models, on the other hand, use mostly physical considerations to model the ocean surface and the scattering on it. As a result they combine two different disciplines, electromagnetism and oceanography. Both these fields of research are treated in considerate detail in chapters 2 and 3.

In this thesis the main focus lies on the analytical modelling of radar seaclutter. This is treated in chapters 2 to 5. Statistical models will not be used as such, but some results from that type of research are used throughout this work. Moreover, a significant effort was made to analyse radar seaclutter data in chapter 6, which is used to validate the analytical model in chapter 7. In the next section an in-depth exploration of the goals of this thesis is made. For that purpose some knowledge of the state-of-the-art in radar seaclutter analysis and modelling is needed. Therefore, a short overview of those topics is given in the following subsections.

1.2.1 Radar seaclutter observations

Radar seaclutter observations are made either on the open sea, see [47, 48, 49, 57, 89, 91, 112, 113], or in wavetanks [25, 30, 50, 49, 51, 85, 87, 97]. The former approach measures true seaclutter, but groundtruthing may be difficult. The latter approach has the advantage that the conditions can be very tightly controlled. However, wavetanks are necessarily restricted, so that only small stretches of ocean can be simulated and effects from the sides of the tank need to be taken into account. Wavetank measurements are usually employed to study certain specific problems, such as wave breaking.

In general, seaclutter consists of two main components. On the one hand there is a diffuse background component, which may form a banding pattern in range-time diagrams. These banding patterns are most often associated with tilt-modulated Bragg-scattering in combination with shadowing behind wavecrests. This observation is well-modelled by composite surface models in combination with shadowing calculations. On the other hand, superimposed on this diffuse background so-called sea spikes may be observed [47, 52, 42, 43, 44, 89]. These spikes are events that develop very quickly, typically within a few hundreds ms, and last rather shortly, 1 to 3 s. They are characterised by high power, polarisation ratios and Doppler velocities. Many theories have been proposed about the nature of these events. The currently accepted view is that they are caused by the scattering on steepened or breaking waves [30, 97]. In chapter 6 a thorough analysis of radar seaclutter data will be made.

1.2.2 Oceanographical modelling

The ocean surface is made up out of many different hydrodynamic features. However, as most of these features occur only infrequently, in this thesis I focus on the two most common ones: linear and breaking waves. Linear waves are those waves that are a direct solution of the wave equation. Usually, three types are identified: sinusoidal, Stokes and Gerstner waves, see [2, 46]. The Stokes wave is slightly pointed at the crest and as a result gives the best approximation of true gravity waves. The Gerstner wave, on the other hand, is slightly pointed in the trough and as such is shaped more like capillary waves. The sinusoidal wave is the most commonly used solution of the wave equation, for two reasons. Firstly, it approximates both the capillary and the gravity waves reasonably well, while the other two only approximate either type. Secondly, the fact that they are sinusoidal allows them to be analysed using standard Fourier theory.

The surface is a collection of many such waves, most of which move independently from each other. This process is commonly described through spectral theory, see [3, 24, 41, 77, 78, 56, 105]. The usual way of determining the spectrum is by measuring a large stretch of surface or a long time series of one point of the surface and subsequently applying a Fourier transform. The result is a function giving the amplitude of the waves in terms of their wavenumber, i.e. the spectrum. There have been some attempts to model the non-linearity of the larger waves, see [18], but that approach is only approximate. The spectral approach has the advantage that it can easily be used to generate ocean surface realisations as will be shown in chapters 2 and 5.

Another type of oceanic feature that will be considered in this thesis is the breaking wave. There are two types of breaking waves: plunging and spilling ones. The former type occurs in shallow water when sea-bottom run-up triggers steepening and breaking, [2]. In this thesis, however, the main interest is in the second type of breaking wave, the spilling breaker, see [7] for a good review. They occur in deep water when the steepness of the wave becomes too high. Consequently, the wave needs to dissipate energy, which it does through a breaking process. Much research has been done on these types of breaking waves, both on their shape and on their dynamical structure [17, 53, 54, 55, 109, 122]. It was found that when the breaking wave exceeds its vertical phase, i.e. when a jet forms, no analytical solution of its shape or dynamics can be found. However, with the improved computing power of the past decades, numerical simulations of these objects have become feasible. The results of one of these simulations, [109], is presented in chapter 2 and will be used throughout this thesis to model breaking waves.

The main unknown about breaking waves remains the specific conditions under which the breaking will occur. Much research has been devoted to this topic, see for instance [4, 8, 9, 7, 40, 122], but no consensus has been reached beyond the fact that the steepness of the wave cannot exceed a certain value. Nonetheless, to

be able to predict radar seaclutter a breaking wave criterion is essential. This is discussed in more detail in chapters 2 and 5.

1.2.3 Electromagnetic modelling

This thesis focuses on the low-grazing angle (LGA) monostatic scattering from the ocean surface at X-band (3 cm radar wavelength). Under those restrictions the scattering from the ocean surface can be divided into two distinct parts. Firstly, there is the scattering on the linear wave-field and, secondly, the scattering on breaking waves that may occur on that surface.

LGA scattering from the linear wave-field is in essence rough-surface scattering. For most incidence angles rough surface scattering is well described by classical Bragg scattering, [19, 72, 103, 104], and composite surface models, [31, 32, 68, 106, 121]. However, for very high incidence angles additional non-linear effects, such as shadowing, multiple scattering and refraction start playing an important role. Many authors have used more advanced full-wave scattering models, such as the Method of Moments (MoM), [11, 16, 22, 62, 63, 74, 83, 90, 93, 114, 117], to evaluate such scattering and indeed some deviations from standard composite surface theory were shown.

Other approaches to scattering from complex surfaces are hybrid models. These types of models combine different scattering approximations to obtain more efficient evaluations of these complex objects. For smooth objects combinations of ray optics and physical optics have been used, see [14, 15] and for partly rough, partly smooth objects a geometric optics/MoM methodology has been shown to give good results, see [114, 115].

The scattering from breaking waves is more complicated than from rough surfaces due to the complex shape of the former objects. Especially the vertical front face and the jet are features that cannot be treated with analytical or approximative methods. As a result more complex scattering methods have been used for evaluating these types of objects: full-wave methods, [38, 39, 99], as well as the earlier mentioned hybrid methods, [58, 118, 115, 116]. In the research that has resulted in this thesis, the approach from [58] was initially followed to evaluate such objects and a reasonable match was found. The added advantage of that approach was that it was capable of evaluating three-dimensional objects and it could, therefore, be used to study the azimuthal scattering pattern of a breaking wave. However, this method only allows the evaluation of larger and relatively smooth objects, i.e. objects whose fine structure is larger than the radar wavelength. Therefore, to analyse the scattering from different scales of breaking wave objects a full-wave method is preferable. This is discussed further in chapters 4 and 5.

1.3 In-depth exploration of the thesis objectives

In section 1.1 the three main goals of this thesis were posed. Taking the information of the previous section about existing models into account, the goals can now be specified in more detail. The first objective of section 1.1, i.e. to identify the gaps in knowledge of seaclutter, was answered in the previous section. It was shown that the main hiatus in current seaclutter research is the combination of composite-surface-like models with models of sea spikes.

The second objective was to build a model that fills these gaps. This model will be presented in chapter 5 of this thesis. Given the main hiatus in seaclutter research, the model needs to fulfil the following requirement:

2a. The model must be a combination of composite surface theory, i.e. tilt-modulated Bragg scattering, and sea spike theory, i.e. semi-specular scattering on breaking waves.

An important part of the combination is supplying the missing link between the two models: a breaking wave criterion. As there seems to be no real consensus in the literature about such a criterion, one will be derived in this Ph.D. thesis.

An additional field of research that has not been sufficiently studied, is dynamics, especially for the spikes. This leads to the second requirement for the model:

2b. The model must be dynamic.

The dynamics part of the model should have two aspects. Firstly, it should be capable of modelling both the spatial and the temporal properties of radar seaclutter and, secondly, the output of the model should, besides power, also give Doppler velocity. Both these aspects will be incorporated into the model in the following manner. The model starts with a spectral surface, that is evolved in time. For this evolving surface, the spatial and temporal locations of the breaking waves are determined with the new breaking wave criterion. Subsequently, the scattering on the so-generated dynamic surface is calculated, which leads to a seaclutter simulation. Besides the scattered power, the model will also be capable of determining the Doppler velocity of the simulated radar seaclutter.

The third main goal of this thesis is:

3. Validate the model through a comparison with radar seaclutter data.

This goal is carried out in chapters 6 and 7. The analysis of seaclutter data will show that velocity is a better indicator for the physical processes underlying the clutter than power is. Consequently, for a thorough understanding of radar seaclutter, dynamics are essential. This fact is further underlined by the validation of the model by the comparison of the simulated with the measured data.

1.4 Thesis structure

This thesis is built up in the following manner. Chapter 2 describes the oceanographic theory that is used in this thesis. It treats the following subjects: standard wave theory, spectral theory and wave breaking. Chapter 3 discusses standard electromagnetic theory. It starts from Maxwell's equations, derives the wave equation and treats various approximations of scattering of these waves on diverse surfaces. Finally, it will discuss full-wave techniques. One of these techniques, the Method of Moments (MoM), is treated in detail in chapter 4. Here the relevant surface integral equation is derived and solved using MoM.

The different theories and techniques described in chapters 2 to 4 are then combined in chapter 5. In that chapter the full radar seaclutter model that fulfils the second goal of this thesis is described. It incorporates spectral theory and breaking wave simulations to model the ocean surface and uses ray tracing, Bragg theory and the MoM code from chapter 4 to model the scattering from that surface. Chapter 6 deals with the analysis and (physical) interpretation of three sets of high resolution X-band radar data. The results from this chapter are used in chapter 7 to fine-tune and validate the seaclutter model from chapter 5. Chapter 8, finally, gives a summary of chapters 1 to 7 and draws the general conclusions of this thesis.

Chapter 2

Ocean surfaces

In this chapter the shape and movement of the ocean surface, the free boundary between the water and the atmosphere, is treated. Essentially, this is a hydrodynamic boundary problem. Therefore, firstly, the governing equations for hydrodynamic behaviour are defined (section 2.1). Secondly, the single water wave problem is defined and two solutions of this problem are derived, the sinusoidal and the Stokes' wave (section 2.2). It will be shown that as a first order approximation the ocean surface can be described as a large collection of such sinusoidal waves, moving essentially without mutual interaction over the surface. This means that the surface under this approximation can be treated by Fourier analysis and spectral theory. This is described in more detail in section 2.3. Finally, in the last section, some non-linear hydrodynamic processes, which occur at the surface, will be treated, with a special interest in breaking waves.

2.1 Hydrodynamic theory

In this section the basic elements of hydrodynamic theory are described. For more information on this topic the reader is referred to standard works on this topic, see for instance [3, 46]. In the next section the properties of two solutions of this wave equation will be treated.

Conservation of mass

Consider a volume of water, V bounded by a surface, S, as is shown in figure 2.1. Let us further consider a small element inside this volume. This element has a density ρ, a position $\mathbf{r} = (x, y, z)$ and a velocity $\mathbf{u} = (u, v, w)$. The element is

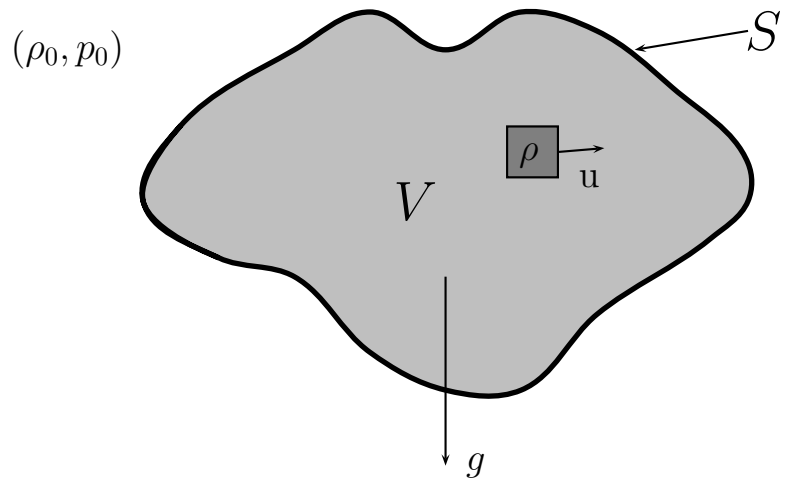

Figure 2.1: Hydrodynamic definitions

subject to the equation of mass conservation,

$$\frac{\partial \rho}{\partial t} + \nabla \cdot (\rho \mathbf{u}) = 0. \tag{2.1}$$

Introducing the material or convective derivative,

$$\frac{D}{Dt} \equiv \frac{\partial}{\partial t} + \mathbf{u} \cdot \nabla, \tag{2.2}$$

equation 2.1 can also be written as,

$$\frac{D\rho}{Dt} + \rho \nabla \cdot \mathbf{u} = 0. \tag{2.3}$$

For many fluids incompressibility, $\rho =$ constant, may be assumed, which means that

$$\frac{\partial \rho}{\partial t} = 0 \quad \rightarrow \quad \nabla \cdot (\rho \mathbf{u}) = 0 \quad \rightarrow \quad \nabla \cdot \mathbf{u} = 0. \tag{2.4}$$

Equation of motion (The Navier-Stokes equation)

On the fluid element a pressure p is working, both from the surrounding water and from the atmosphere outside the volume of water. Moreover, most fluids have a certain viscosity, i.e. internal friction. Finally, a number of forces may be working on the fluid, both surface and body forces. The former are forces working only on the surface of the fluid, the latter are forces working on the entire fluid element.

The rest of this chapter is restricted to fluids on the earth surface. This allows the identification of the forces working on the fluid. At the earth surface three forces are working, gravity and the centrifugal and Coriolis forces.

The motion of a fluid element due to these forces is described by the Navier-Stokes equation,

$$\frac{D\mathbf{u}}{Dt} = -\underbrace{2\Omega \times \mathbf{u}}_{\text{Coriolis}} - \underbrace{\nabla\Phi}_{\text{Gravity}} - \underbrace{\frac{1}{\rho}\nabla p}_{\text{Pressure}} + \underbrace{\frac{1}{\rho}\nabla \cdot \mathbf{A} \cdot \nabla \mathbf{u}}_{\text{Viscosity + Eddies}}. \tag{2.5}$$

Studying the Navier-Stokes equation it can be seen that it is in fact Newton's second law applied to a fluid element on the surface of the earth. The left hand side is the time derivative of the velocity, the acceleration, of the fluid. The right hand side sums up the classical forces working on the fluid divided by the mass in the form of the density.

In the study of ocean surface waves the effects of both Coriolis and viscosity can be neglected, so that these terms may be set to zero. An additional simplification can be made for the effects of gravity and centrifugal force. It is possible to define the effective gravitational acceleration, $\mathbf{g} = \hat{\mathbf{z}}g$, which combines the effects of both the gravity and the centrifugal forces on the surface of the earth. The value of g on different parts of the earth can easily be looked up in available tables. Applying these simplifications the Navier-Stokes equation becomes,

$$\frac{D\mathbf{u}}{Dt} = -g\hat{\mathbf{z}} - \frac{1}{\rho}\nabla p, \tag{2.6}$$

which is also known as Euler's equation.

However, in this equation a number of additional forces which may work on the fluid are not included. These additional forces will be included in the form of two vectors, $\mathbf{S}$ respectively $\mathbf{B}$, representing surface respectively body forces. Surface forces are forces working only on the surface of the fluid, like wind friction. Body forces are forces which work on the entire body of the fluid, for instance the gravity of the moon (in tide studies) or electromagnetic forces (in plasma physics). Thus the equation of motion finally becomes,

$$\frac{D\mathbf{u}}{Dt} = -g\hat{\mathbf{z}} - \frac{1}{\rho}\nabla p + \mathbf{B} + \mathbf{S}. \tag{2.7}$$

Vorticity, stream lines and the velocity potential

Vorticity, denoted as $\boldsymbol{\omega}$, is a measure of the local spin or rotation of the fluid and is defined as the curl of the velocity field,

$$\boldsymbol{\omega} = \nabla \times \mathbf{u}. \tag{2.8}$$

Applying this concept to Euler's equation, equation (2.6), Bernoulli's theorem is obtained. Rewrite Euler's equation as,

$$\frac{D\mathbf{u}}{Dt} = -\nabla\Omega - \frac{1}{\rho}\nabla p, \tag{2.9}$$

where $\Omega = gz$ is a potential function. This can be rewritten as,

$$\frac{\partial \mathbf{u}}{\partial t} + \nabla\left(\frac{1}{2}\mathbf{u}\cdot\mathbf{u} + \frac{P}{\rho} + \Omega\right) = \mathbf{u}\times\boldsymbol{\omega}. \tag{2.10}$$

Now for a steady flow, $\frac{\partial \mathbf{u}}{\partial t} = 0$ this becomes,

$$\nabla\left(\frac{1}{2}\mathbf{u}\cdot\mathbf{u} + \frac{P}{\rho} + \Omega\right) = \mathbf{u}\times\boldsymbol{\omega}. \tag{2.11}$$

Introduce a streamline as a curve with the property that everywhere along the curve the velocity vector is tangent. Along a streamline the quantity $\mathbf{u}\times\boldsymbol{\omega} = 0$, which means that along a streamline,

$$\frac{1}{2}\mathbf{u}\cdot\mathbf{u} + \frac{P}{\rho} + \Omega = \text{constant}. \tag{2.12}$$

This is known as Bernoulli's theorem. The terms on the left hand side in fact represent the total energy (kinetic + work done by the pressure + potential), and thus Bernoulli's theorem describes the conservation of energy for a steady flow.

An irrotational flow is a flow with $\boldsymbol{\omega} \equiv 0$, which means that $\nabla\times\mathbf{u} = 0$. This then allows the introduction of a velocity potential ϕ, so that $\mathbf{u} = \nabla\phi$. If the flow is also incompressible, the velocity potential satisfies Laplace's equation,

$$\nabla\cdot\mathbf{u} = \nabla\cdot\nabla\phi = \Delta\phi = 0. \tag{2.13}$$

2.2 Wave theory

In the last section the equation of motion for fluids, the Navier-Stokes equation, was presented. In this section, this equation will be applied to the problem of water waves. Consider the problem as defined in figure 2.2. A layer of water of depth h and density ρ_0 is bounded at the upper side by a free interface and on the lower side by a rigid bottom. The hydrostatic pressure, the pressure in the undisturbed state, is then simply a function of depth, z,

$$p_h = p_a - \rho_0 g z, \tag{2.14}$$

where p_a is the atmospheric pressure. When a force is applied to the surface, it creates a disturbance of this surface, characterised by the displacement η.

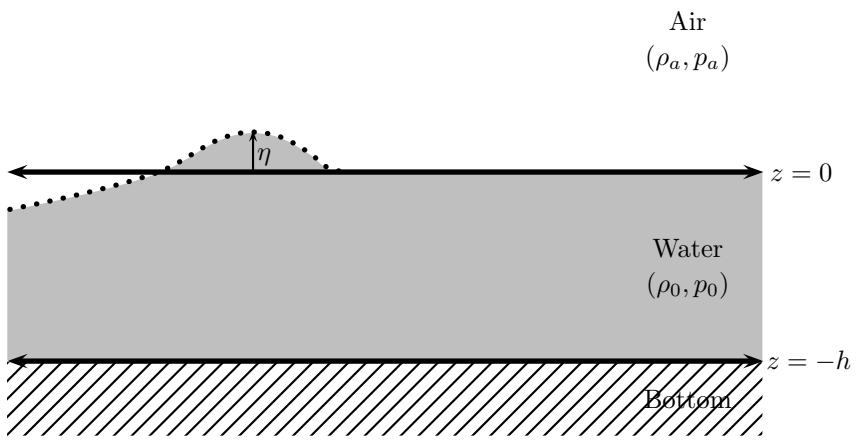

Figure 2.2: Water wave problem

Now assume the fluid to be irrotational and incompressible, which means that $\Delta\phi = 0$, see equation (2.13). One additional approximation may be made, the Boussinesq approximation, which states that the total pressure in the fluid is the sum of the hydrostatic pressure, $p_h = p_a - \rho_0 g z$ and the perturbation pressure, $p' = \rho_0 g \eta$,

$$p = p_a + \rho_0 g(-z + \eta). \tag{2.15}$$

Let us also assume that after the initial disturbance no more forces are applied to the surface. Under all these assumptions the equation of motion reduces to,

$$\rho \frac{\partial \mathbf{u}}{\partial t} = -\nabla p'. \tag{2.16}$$

Taking the divergence on both sides of the equation and remembering that $\nabla \cdot \mathbf{u} = 0$ for an incompressible fluid, gives Laplace's equation for the pressure,

$$-\rho \frac{\partial}{\partial t}(\nabla \cdot \mathbf{u}) = \nabla \cdot \nabla p' = \Delta p' = 0. \tag{2.17}$$

In order to solve these equations the boundary conditions for this system need to be defined. For the full derivation of these conditions the reader is referred to the standard literature mentioned in section 2.1. At the upper boundary $z = \eta$ and at the bottom boundary $z = -h$ the conditions are:

$$\begin{array}{lcll} w(z) & = & \frac{\partial \eta}{\partial t} & \text{at } z = \eta \\ p(z) & = & p_0(z) + p'(z) = p_a & \text{at } z = \eta \\ w(z) & = & 0 & \text{at } z = -h \\ \frac{\partial p'(z)}{\partial z} & = & 0 & \text{at } z = -h. \end{array} \tag{2.18}$$

The derivation ignores the effects of surface tension and is as such only suited for gravity waves. Treatment of capillary waves therefore requires the inclusion of surface tension. Surface tension is the force that supports a pressure across a curved surface,

$$\Delta p = p - p_a = -\tau_s \left(\frac{1}{R_x} + \frac{1}{R_y} \right), \tag{2.19}$$

where $1/R_x$ and $1/R_y$ are the two-dimensional curvatures. However, the curvatures are approximately the second derivatives of the surface elevation so that,

$$\Delta p = p - p_a = -\tau_s \left(\frac{\partial^2 \eta}{\partial x^2} + \frac{\partial^2 \eta}{\partial y^2} \right), \tag{2.20}$$

For clean water $\tau_s = 0.079\text{N m}^{-1}$. The inclusion of surface tension in the boundary conditions can then be made by forcing

$$p = p_a - \tau_s \left(\frac{\partial^2 \eta}{\partial x^2} + \frac{\partial^2 \eta}{\partial y^2} \right) \qquad \text{on } z = \eta, \tag{2.21}$$

instead of the classical $p = p_a$.

By defining the equation of motion, Laplace's equations for the pressure and the velocity potential as well as the boundary conditions at the upper and lower boundaries, we now have the tools to solve the problem of water waves. Many solutions are possible, like Crapper, Gertner, Stokes and sinusoidal waves, but only the latter two will be treated here. The sinusoidal wave has the advantage of simplicity and can be used in Fourier analysis. Unfortunately, most ocean waves are not fully sinusoidal in shape, but have a more trochoidal shape, i.e. sharper crests and shallower troughs. This shape is better modelled by the Stokes' waves.

2.2.1 Sinusoidal waves

The easiest solution to the problem described above is a sinusoidal wave,

$$\eta(\mathbf{r}, t) = \eta_0 \cos(\omega t \pm \mathbf{k} \cdot \mathbf{r}). \tag{2.22}$$

Sinusoidal water waves have a number of properties, which are analogous to those of electromagnetic plane waves. The difference between the two is that the electromagnetic waves are defined in three-dimensional space, while the water waves are restricted to the surface and therefore two-dimensional. This means that the standard quantities, like wavenumber, frequency and velocity as defined for the electromagnetic waves can also be defined for the water waves, but these are only dependent on the two horizontal dimensions, $\hat{\mathbf{x}}$ and $\hat{\mathbf{y}}$.

Define $\mathbf{k} = (k_x, k_y)$ as the propagation vector, with amplitude k, which is called the wavenumber. The wavenumber is then related to the wavelength, λ by,

$$k = 2\pi/\lambda. \tag{2.23}$$

The radian frequency, ω, frequency, f, and the period T are linked through,

$$\omega = 2\pi f = 2\pi/T. \tag{2.24}$$

Applying the boundary conditions, the following dispersion relation between ω and $\mathbf{k}$ is found,

$$\omega(\mathbf{k}) = \pm\sqrt{(gk + k^3\tau_s/\rho)\tanh(kh)}. \tag{2.25}$$

Then the phase velocity of the wave is,

$$v_{ph} = \frac{\omega}{k} = \pm\sqrt{(g/k + k\tau_s/\rho)\tanh(kh)}. \tag{2.26}$$

What is interesting to notice is that the phase velocity has a minimum at $\partial v_{ph}/\partial k = 0$. This occurs for $k = 363$ at a velocity of 0.23 m s^{-1}.

Consider the two limiting regimes for water waves, the capillary and the gravity regime.

Capillary waves

If $k \gg 1$ the factor gk is negligible to $k^3\tau_s/\rho$ and the dispersion relation and phase velocity simply become,

$$\omega = \pm\sqrt{(k^3\tau_s/\rho)\tanh(kh)} \tag{2.27}$$

$$v_{ph} = \pm\sqrt{(k\tau_s/\rho)\tanh(kh)}. \tag{2.28}$$

In effect this means that for these very small waves surface tension is the main restoring force. For these waves usually $kh \gg 1$, so that $\tanh(kh) \approx 1$ and the dispersion relation and the phase velocity become,

$$\omega = \pm\sqrt{k^3\tau_s/\rho}, \qquad v_{ph} = \pm\sqrt{k\tau_s/\rho}. \tag{2.29}$$

Gravity waves

If k is small enough, the factor $k^3\tau_s/\rho$ is negligible to gk. In this case the main restoring force is gravity. For gravity waves the dispersion relation and the phase velocity are,

$$\omega = \pm\sqrt{(gk)\tanh(kh)}, \qquad v_{ph} = \pm\sqrt{(g/k)\tanh(kh)}. \tag{2.30}$$

If the water is deep enough, $kh \gg 1$, then $\tanh(kh) \approx 1$ and the dispersion relation and the phase velocity become,

$$\omega = \pm\sqrt{gk}, \qquad v_{ph} = \pm\sqrt{g/k}. \tag{2.31}$$

In the shallow water limit, $kh \ll 1$, then $\tanh(kh) \approx kh$, and the dispersion relation and the velocity are,

$$\omega = \pm\sqrt{ghk^2}, \qquad v_{ph} = \pm\sqrt{gh}. \tag{2.32}$$

so that the velocity becomes a constant.

The stream function

For the sinusoidal wave it can be shown that the vorticity is indeed zero. This allows the definition of the stream function for these waves. For simplicity consider one single wave and assume it is moving in the x direction. This means that $\mathbf{u} = (u, 0, w)$. The Langrangian stream function $\psi = \psi(x, z, t)$ is then defined as,

$$\psi(x, z, t) = \psi_a + \int (udz - wdx), \tag{2.33}$$

where ψ_a is a function independent of x and z and the integral is taken along a curve starting at a reference point to the point (x, z). As there is no flow across a streamline, ψ is constant along a streamline. For the sinusoidal solution, the stream function is found to be,

$$\psi(x, z, t) = \psi_a + \psi_0 \sinh k(z + h) \cos(kx - \omega t), \tag{2.34}$$

where

$$\psi_0 = \frac{2g\eta_0}{\omega} \cosh kh. \tag{2.35}$$

Various examples of the stream function can be found in [2], figure 5.13.

2.2.2 Stokes waves

Another solution of the wave equation is the Stokes wave. It is an approximate solution, which is trochoid in shape. This means a sharper crest and shallower trough than for a sinus. The derivation of this type of wave will not be shown here, only the results.

To fourth order the Stokes wave is approximated by,

$$\begin{aligned} \frac{1}{a}\eta &= -\cos kx + \frac{1}{2}\pi\delta(1 + \frac{25}{24}\pi^2|delta^2)\cos 2kx \\ &\quad -\frac{3}{8}\pi^2\delta^2(1 - \frac{3}{4}\pi^2\delta^2)\cos 3kx + \frac{1}{3}\pi^3\delta^3 \cos akx, \end{aligned} \tag{2.36}$$

with δ the wave steepness, $\delta = \eta_0/\lambda$. Under this approximation the phase speed is given by,

$$v_{ph}^2 = \frac{g}{k}\left(1 + \pi^2\delta^2 + \frac{1}{2}\pi^4\delta^4\right). \tag{2.37}$$

Thus for stokes waves the phase velocity is dependent on the wave steepness and so for a wave of a certain wavelength on the amplitude. Another important result for Stokes waves is that it can be proven mathematically that such waves have a finite steepness. In fact it can be shown that the minimum opening angle of the crest should be 120°. If the wave has this steepness, the acceleration at the crest is equal to g. So for waves steeper than this limit, the acceleration at the crest would exceed g, which means that these types of waves cannot be restored by gravity, which will lead to destabilisation and breaking. This will be treated more in-depth in section 2.5.

2.3 Spectral analysis

In the last section the wave equation for water waves was derived and a number of different solutions for this equation were given. One of these solutions consisted of standard sinusoidal waves, which will be used in this section. Real ocean waves might actually be closer to either crapper or stokes waves, but the sinus has the advantage that it allows the use of Fourier analysis. The ocean surface consists of a large number of different waves with different wavelengths and amplitudes. The waves do influence each other somewhat, but as a first order approximation it is safe to assume that all the waves move independent from each other. By assuming these waves to be sinusoidal, the ocean surface gets a Fourier basis, which allows description of the surface with a (complex) amplitude spectrum.

A large number of researchers have worked on spectral analysis of ocean surfaces [3, 24, 41, 77, 78, 56, 105]. Essentially this type of research is performed as follows: Either a large stretch of surface or a long time series of a point at the ocean surface is recorded. A Fourier transform is then applied to this recording resulting in a complex wavenumber (for the spatial record) or a frequency (for the time record) spectrum. If, as it is often assumed, the waves essentially experience little or no influence from other waves, the phase of the complex signal should be randomly distributed. The relevant information is thus contained in the amplitude of the spectrum. In the following we will concentrate only on the amplitude of the spectra.

Most research on this subject has concentrated on finding parameterisations of these spectra. Usually, researchers have attempted to find a physical basis for their parameterisations, but as yet the physical basis for some of the parameterisations remains unclear. In this section we will describe some of the most commonly accepted spectral models, i.e. the Donelan-Banner-Jähne [3] and the Romeiser-Alpers-Wisman spectra [77, 78].

The main problem of the spectral approach is that it can only describe linear wave fields. Linear means a linear superposition of sinusoidal waves. In reality, however, the wave field consists of both linear, sinusoidal, and strongly non-linear objects like wedges, bound waves, foam, and breaking waves. Of these non-linear

objects we will mainly concentrate on breaking waves. The reason for this is that these objects are most likely connected with sea spikes, as was mentioned in chapter 1.

2.3.1 Wind profiles

It is now convenient to first define the different wind speeds that will be used throughout the rest of this chapter. The wind speed, u, at a particular point is dependent on a number of things. Firstly, u depends on the general wind speed. One therefore needs to define a reference wind speed, u_z. This u_z is the wind speed measured by an anemometer at a height, z, above the surface. An often used reference height is $z = 10$ m, which will be used throughout this chapter. The second parameter the wind speed depends on is the height above the surface. This dependence is given by,

$$u_z = \frac{u_*}{\kappa} \ln\left(\frac{z}{z_0}\right), \tag{2.38}$$

where κ is von Karman's constant, which has a value of approximately 0.40, u_* is the friction velocity and z_0 is the roughness length. A number of different parameterisations exist for the relation between u_* and z_0. Inoue suggested,

$$z_0 = 0.01\left(\frac{0.0684}{u_*} + 4.28u_*^2 - 0.443\right). \tag{2.39}$$

Another parameterisation was put forward by Garratt,

$$z_0 = \frac{0.0144}{g}u_*^2. \tag{2.40}$$

Smith changed the constant in the formulation by Garratt slightly to 0.0110, but retained the same shape,

$$z_0 = \frac{0.0110}{g}u_*^2. \tag{2.41}$$

Given the wind speed at a certain height and substituting equation (2.39), (2.40), or (2.41) into equation (2.38) it is possible to calculate the wind speed as a function of height.

2.3.2 Equilibrium spectra

An equilibrium wave height spectrum is a spectrum for which the energy that is supplied by wind stress is equal to the energy that is dissipated ate the surface. An ocean surface with an equilibrium spectrum is also called a fully developed sea. In order to obtain such an equilibrium the wind stress should be approximately constant over a long time and long fetch. This means that equilibrium spectra are

mostly found on the open sea. In coastal areas the wavefield usually has had insufficient time or fetch to evolve fully. This thesis, however, will mainly concentrates on equilibrium spectra. In particular two parameterisations will be described here, the Donelan-Banner-Jähne (DBJ), see [3] and the Romeiser-Alpers-Wisman (RAW) spectra, see [77, 78].

Both the DBJ and RAW spectra have the general form of,

$$\Psi = \Psi_a(k, \phi)\Psi_r(k), \tag{2.42}$$

where Ψ_a is the angular wave spectrum, Ψ_r the radial wave spectrum, k the wavenumber of the waves, and ϕ the angle between the waves and the wind.

The model devised in this thesis is two-dimensional, i.e. radial. This means that the influence of directional spread can be ignored. Hence Ψ_a is set to 1.

The radial spectrum is again split up in a number of parts,

$$\Psi_r(k) = A\frac{F_l J_p F_h}{k^4}, \tag{2.43}$$

where A is a constant, which by [3] was determined to be 0.00195, F_l the low-frequency roll-off, F_h the high-frequency roll-off and J_p the peak enhancement factor.

Low-frequency roll-off

The low-frequency roll-off was first modelled by Pierson and Moskowitz in 1964, see [66]. It has the form,

$$F_h = \exp\left(-\frac{k_p^2}{k^2}\right), \tag{2.44}$$

where k_p is the peak wavenumber. The peak in the spectrum occurs at the wavenumber for which the waves have the same velocity as the wind. Larger, faster-moving waves cannot effectively obtain energy from the wind field and will therefore be much shallower. This explains the rapid drop-off for waves larger than the peak wavelength. The factor k_p is then established by,

$$v_{ph,p} = \frac{\omega}{k_p} \approx u \quad \rightarrow \quad k_p = \frac{g}{\sqrt{2}u^2}. \tag{2.45}$$

Peak enhancement factor

The original formula of Pierson and Moskowitz failed to take a number of nonlinear effects into account. These effects cause an overshoot around the peak of the spectrum. This was first described during the JONSWAP project, see citehasselmann1.

Later this expression for the peak enhancement factor was adopted and modified by [21]. The form used both in the DBJ and the RAW spectra is,

$$J_p(k) = \Gamma^{\gamma(k)}, \tag{2.46}$$

$$\gamma(k) = \exp\left[-\frac{\left(\sqrt{k}-\sqrt{k_p}\right)^2}{2\delta^2 k_p}\right], \tag{2.47}$$

where $\Gamma = 1.7$ for fully developed seas, and $\delta = 0.40$.

High-frequency roll-off

The only part of the spectrum where there is significant difference between the RAW and DBJ spectra is the high-frequency roll-off. The F_h of the DBJ spectrum is based on the parameterisation of a number of physical processes thought to contribute to the spectral shape at high wavenumbers. The expression in the RAW spectrum on the other hand is based wholly on an empirical model obtained from radar data.

In the DBJ spectrum the high-frequency roll-off takes the form,

$$F_h = \left(R_{\rm ro} + S(u)R_{\rm res}\right) V_{\rm dis}, \tag{2.48}$$

with

$$R_{\rm ro} = \frac{1}{1+\left(\frac{k}{k_{\rm ro}}\right)^2}, \tag{2.49}$$

$$S(u) = \exp\left\{\left[s_1 + s_2\left(1-e^{-\frac{u}{u_\eta}}\right)\right]\ln 10\right\} \tag{2.50}$$

$$R_{\rm res} = ak\ \mathrm{sech}\left(\frac{k-k_{\rm res}}{k_w}\right) \tag{2.51}$$

$$V_{\rm dis} = e^{-\frac{k^2}{k_{\rm dis}^2}}. \tag{2.52}$$

The various constants in these expressions are,

$$\begin{array}{c} s_1 = -4.95, \quad s_1 = -3.45, \quad k_{\rm ro} = 100 \text{ rad/m}, \quad a = 0.8, \\ k_{\rm res} = 400 \text{ rad/m}, \quad k_w = 450 \text{ rad/m}, \quad k_{\rm dis} = 6283 \text{ rad/m}. \end{array} \tag{2.53}$$

For the RAW spectrum the high-frequency roll-off is,

$$F_h = \left(\frac{u_{10}}{u_n}\right)^\beta \frac{\left[1+\left(\frac{k}{k_6}\right)^{7.2}\right]^{0.5}}{\left[1+\left(\frac{k}{k_7}\right)^{2.2}\right]\left[1+\left(\frac{k}{k_6}\right)^{3.2}\right]^2} \exp\left(-\frac{k^2}{k_9^2}\right), \tag{2.54}$$

where β is given by,

$$\left[1-\exp\left(-\frac{k^2}{k_1^2}\right)\right]\exp\left(-\frac{k}{k_2}\right)\left[1-\exp\left(-\frac{k}{k_3}\right)\right]\exp\left[-\left(\frac{k-k_4}{k_5}\right)\right]. \quad (2.55)$$

Here, the constants are,

$$\begin{array}{lll} k_1 = 183 \text{ rad/m}, & k_2 = 3333 \text{ rad/m}, & k_3 = 33 \text{ rad/m}, \\ k_4 = 140 \text{ rad/m}, & k_5 = 220 \text{ rad/m}, & k_6 = 280 \text{ rad/m}, \\ k_7 = 75 \text{ rad/m}, & k_8 = 1300 \text{ rad/m}, & k_9 = 8885 \text{ rad/m}. \end{array} \quad (2.56)$$

2.4 Currents

In this section the influence of currents on the wavefield is discussed. Moreover, a technique for estimating the current from images of the wavefield is introduced.

2.4.1 The effects of current on the wavefield

Surface waves are in essence only disturbances of the free sea-air interface. On average no mass will be transported by a wave. On the other hand, Currents do not disturb the surface, but the entire body of water is moved by a current. The effects of currents on surface waves are twofold. Firstly the phase velocity of the waves will be affected. The effective phase velocity of a wave experiencing a current with velocity $\mathbf{u}_c$ is,

$$\mathbf{v}'_{ph} = \mathbf{v}_{ph} + \mathbf{u}_c. \quad (2.57)$$

This will in turn affect the dispersion relation,

$$\omega'(\mathbf{k}) = \pm\sqrt{(g\mathbf{k} + \mathbf{k}^3\tau_s/\rho)\tanh(\mathbf{k}h)} + \mathbf{k}\cdot\mathbf{u}_c. \quad (2.58)$$

This means that by measuring the dispersion relation for a wavefield allows a researcher to determine the magnitude and direction of a current. For more information on this subject see for instance [94].

The second effect of a current on a wave is that energy may be transferred between the current and the wave. This process, called wave-current interaction, may lead to either growth or dissipation of waves. This is described by the action-balance equation. The process will not be treated here, but interested readers are referred to [105].

2.4.2 Estimating the current from wave images

It is possible to determine the current underlying a wavefield from a series of images of that same wavefield. The procedure is, for instance, explained in [120]. Here the

procedure is explained for 1-dimensional observations, such as the ones presented in chapter 6. However, it is possible to extend the procedure to two dimensions.

Assume a timeseries of 1D observations: $p(r, t_i)$. Here p is the scattered power, r is the 1D range along which the observations were made and $t_i = t_1 : t_n$ is the series of timestamps at which the observations were made. In chapters 3 and 6 it is explained that the power of a seaclutter observation is directly linked to the slope of he scattering surface. As a result a series of observations of the scattered power from the ocean surface images the wavefield on that surface. By applying a simultaneaous space and time Fourier transform, the power as a function of frequency and wavenumber is obtained. As the power images the wavefield, the regions of highest power in the frequency-wavenumber domain should follows the dispersion relation. Having obtained the measured dispersion relation, the current can be obtained by fitting it to the known dispersion relation, i.e. equation 2.58. For a more thorough illustration of this procedure see section 6.5.1.

2.5 Breaking waves

Having discussed the linear wavefield and currents, the last ocean surface feature of interest in this thesis is the breaking wave. Breaking waves occur in three main forms: micro-, plunging and spilling breakers.

Plunging breakers occur in shallow water and are caused by instabilities due to interactions between the waves and the sea bottom, see [2]. As such they mainly occur in the surf zone and are not treated in this thesis. In 'deep' water breaking mainly occurs in the other two forms. Of these, micro-breakers are not treated in much detail, except in section. Micro-breakers, [], are very small events, i.e. cm size, and cause no visible whitecapping. They might, however, be capable of affecting seaclutter, a phenomenon which is treated in section 7.6.

This thesis is mainly concerned with the spilling breaker. As explained in chapter 1, much research has been devoted to this type of breaker, [7, 17, 53, 54, 55, 109, 122]. In the rest of this section, both the conditions leading up to the event and the evolution of the shape of the event itself are treated.

2.5.1 Breaking conditions

Much research has been devoted to this topic, see for instance [4, 8, 9, 7, 40, 122], but no consensus has been reached beyond the fact that the steepness of the wave cannot exceed a certain value. The first such breaking condition was Stokes' theorem [92] that the opening angle at the crest should not be less than 120°. Steeper waves are unstable and will break. In 1975 it was shown by Longuet-Higgins, [53] that for a uniform wave train the energy density has a maximum at $ak = 0.443$, where a is

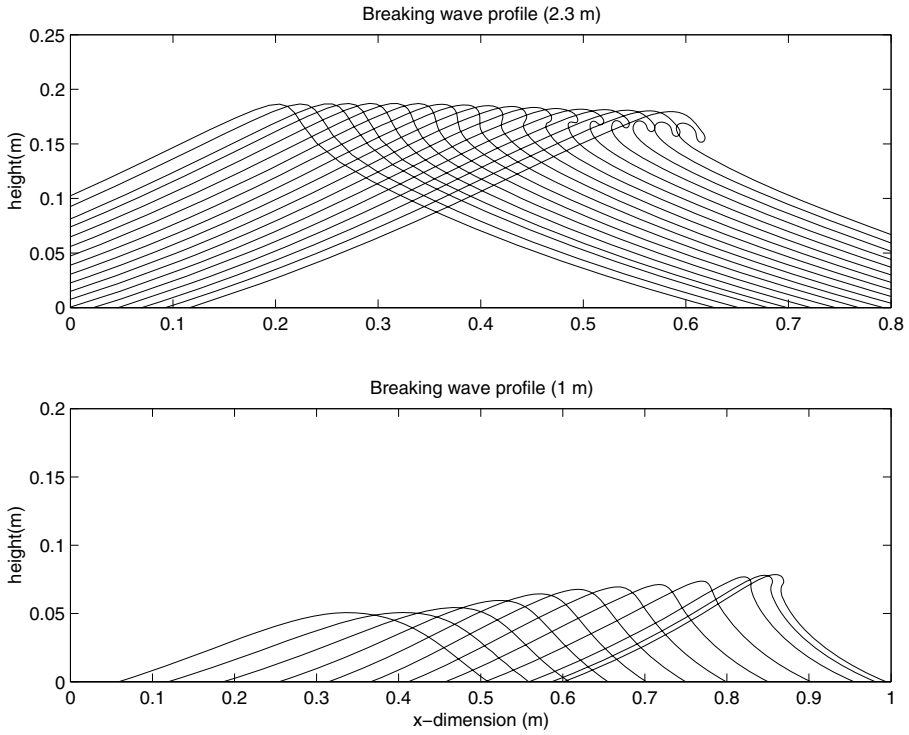

Figure 2.3: Breaking wave profiles from [109]. The upper panel gives the evolution of a breaking wave with a wavelength of 2.3 m, while the lower panel give the evolution of a breaking wave with a wavelength of 1.0 m. The 2.3 m wave has been modelled without surface tension and as such can be scaled upwards at will.

the amplitude of the wave, and at above that steepness breaking will occur. Later, [54, 55], he suggested a value of $ak = 0.38$. Other researchers have obtained similar values of ak, see for instance [8, 40].

On the open ocean uniform wave trains do not occur. However, group processes may lead to rapid wave growth. In the last decade significant work has been done on this topic. A likely process may be the following, see [17]. Whenever a wave group is overtaken by a dominant wave the group may steepen. Especially the smaller components of the groups can easily exceed the breaking limit. This will lead to microbreaking events. If the group is unstable enough these micro breakers may lead to a cascade effect where larger and larger waves break. This will then finally lead to the breaking of larger, gravity waves, which will generate the visible whitecap.

2.5.2 Breaking wave form and evolution

Linear wave theory does not describe the occurrence of breaking waves. The calculations of the shape of such events quickly become too complicated to be performed analytically. Some efforts have been made on Gertner waves, see for instance [46], but these were largely unsuccessful in giving a good description of breaking waves. The main problem occurs when the front face of the wave becomes vertical or even exceeds the vertical. The analytical solutions break down at that point and numerical techniques must be used. A great deal of effort has been made on numerically solving the hydrodynamic calculations, with varying degrees of success, see [17, 53, 54, 55, 109, 122]. The solution of this problem is hydrodynamic in nature and does not lie within the scope of this thesis. The author will mainly use the results of such calculations.

In this thesis breaking wave simulations are used that were generated with the LONGTANK simulator, [109]. LONGTANK numerically simulates the occurrence of breaking waves in a wave tank. The authors started with the approach pioneered by [54]. Following this approach they managed to describe the free surface boundary using BEM (boundary with Neumann condition). Subsequently, the surface was divided in a number of subdomains, each of which was evaluated using the BEM formulation. This allowed the efficient evaluation of the entire surface. As setup for the simulation a restricted problem was chosen. The surface was assumed to be restricted to a wavetank with an artificial beach to dissipate the generated waves. It was found that the above described approach could generate simulations of spilling breakers. An example of two sets of these breaking waves can be found in figure 2.3. This figure shows a time series of 2.3 m (upper panel) and a 1.0 m (lower panel) breaking waves. The former set was modelled without surface tension and, as a result, it can easily be scaled upwards at will. These two examples have been widely used in literature for evaluating the electromagnetic scattering from breaking waves, [38, 39, 58, 118, 115, 116].

Chapter 3

Electromagnetic scattering

In this chapter an overview of electromagnetic scattering theory is given. Starting from Maxwell's equations the general expression and properties of plane waves are derived in section 3.1. Subsequently, the theory of scattering of such waves on a surface is treated in section 3.2. It is shown that for a number of simple surface types the scattering problem can either be solved analytically or approximated with a reasonable accuracy. However, scattering from more complicated types of surfaces cannot be treated with these techniques and for those problems so-called full waves solutions are needed. The basic theory of one of these methods, the method of moments (MoM) is described in section 3.2.3. The latter is studied in more detail in chapter 5. Finally, in the last section a link is made with radar observations.

3.1 Fundamental theory

The fundamental equations governing electromagnetic behaviour are Maxwell's equations. In a medium with permittivity ϵ and permeability μ they take the form,

$$\nabla \cdot \mathbf{E} = \frac{\rho}{\epsilon}, \tag{3.1}$$

$$\nabla \times \mathbf{E} = -\frac{\partial \mathbf{B}}{\partial t}, \tag{3.2}$$

$$\nabla \cdot \mathbf{B} = 0, \tag{3.3}$$

$$\nabla \times \mathbf{B} = \mu \mathbf{J} + \mu\epsilon \frac{\partial \mathbf{E}}{\partial t}. \tag{3.4}$$

Here $\mathbf{E}$ is the electric field strength, $\mathbf{B}$ the magnetic flux density, $\mathbf{J}$ the current density and ρ the electric charge density. Some authors prefer using the magnetic

field strength, $\mathbf{H}$, instead of $\mathbf{B}$. The relation between $\mathbf{H}$ and $\mathbf{B}$ is given by

$$\mathbf{H} = \frac{1}{\mu}\mathbf{B} - \mathbf{M}, \tag{3.5}$$

where $\mathbf{M}$ is the magnetisation vector. However, due to the fact that ferro-magnetic materials will not be taken into account within the scope of this work, $\mathbf{M}$ equals zero and 3.5 simply becomes,

$$\mathbf{H} = \frac{1}{\mu}\mathbf{B}. \tag{3.6}$$

The current and the charge density are linked through the law of conservation of charge, which is also called the equation of continuity,

$$\nabla \cdot \mathbf{J} = -\frac{\partial \rho}{\partial t}. \tag{3.7}$$

Finally the electromagnetic potentials are defined in the following manner,

$$\mathbf{E} = -\nabla\Phi - \frac{\partial \mathbf{A}}{\partial t} \tag{3.8}$$

$$\mathbf{B} = \nabla \times \mathbf{A}, \tag{3.9}$$

where Φ is called the scalar potential and $\mathbf{A}$ the vector potential.

3.1.1 The wave equation

In a source-free region, i.e. $\rho = 0$ and $\mathbf{J} = 0$, Maxwell's equations take the form,

$$\nabla \cdot \mathbf{E} = 0, \tag{3.10}$$

$$\nabla \times \mathbf{E} = -\frac{\partial \mathbf{B}}{\partial t}, \tag{3.11}$$

$$\nabla \cdot \mathbf{B} = 0, \tag{3.12}$$

$$\nabla \times \mathbf{B} = \mu\epsilon\frac{\partial \mathbf{E}}{\partial t}. \tag{3.13}$$

Taking the curl of equation 3.11 gives,

$$\nabla \times \nabla \times \mathbf{E} = -\frac{\partial}{\partial t}(\nabla \times \mathbf{B}). \tag{3.14}$$

Applying the vector identity $\nabla \times (\nabla \times \mathbf{E}) = \nabla(\nabla \cdot \mathbf{E}) - \nabla^2\mathbf{E}$ to the left hand side and substituting equation 3.13 into the right hand side results in,

$$\nabla(\nabla \cdot \mathbf{E}) - \nabla^2\mathbf{E} = -\mu\epsilon\frac{\partial^2 \mathbf{E}}{\partial t^2}. \tag{3.15}$$

But, remembering that $\nabla \cdot \mathbf{E} = 0$, cf. equation 3.10, gives,

$$\nabla^2 \mathbf{E} = \mu\epsilon \frac{\partial^2 \mathbf{E}}{\partial t^2}, \tag{3.16}$$

which is the homogeneous wave equation. Taking the curl of equation 3.13, again applying the vector identity and substituting from equation 3.11, a similar equation for the magnetic flux density is obtained,

$$\nabla^2 \mathbf{B} = \mu\epsilon \frac{\partial^2 \mathbf{B}}{\partial t^2}. \tag{3.17}$$

3.1.2 Solving the wave equation: Plane waves

In the last section the wave equation was derived. The general solution of the wave equation is,

$$f(\mathbf{r} + \mathbf{v}t) + f(\mathbf{r} - \mathbf{v}t), \tag{3.18}$$

which represents two waves, one moving in the negative and one in the positive direction, both with velocity $\mathbf{v}$. Each solution of this form is a type of (electromagnetic) wave. However, in this work the main interest is in plane waves. The theory of electromagnetic waves and in particular plane waves is well known. In this section a short review of the subject will be given. For more details on this topic the reader is referred to standard works on electromagnetic theory, for instance [27], chapters 18, 20, 32 and 33 and [100], chapter 2. In this work the notation of [28] will be followed.

The standard solution to the wave equation (3.16), known as the plane wave, is,

$$\mathbf{E}(\mathbf{r}, t) = \mathbf{E}_0 \Re \left(e^{j(\omega t \pm \mathbf{k}\cdot\mathbf{r})} \right), \tag{3.19}$$

where ω is the radian frequency, $\mathbf{E}_0$ is a constant vector and $\mathbf{k}$ and $\mathbf{r}$ are the propagation vector and the displacement vector defined by,

$$\mathbf{k} = \hat{x}k_x + \hat{y}k_y + \hat{z}k_z \tag{3.20}$$

$$\mathbf{r} = \hat{x}r_x + \hat{y}r_y + \hat{z}r_z. \tag{3.21}$$

Notice that for plane waves the time and space variables may be separated and treated independently. In effect the problems considered within this work may be treated as static problems.

3.1.3 Time behaviour of the electromagnetic fields

An integral part of this thesis will be spectral analysis. From a physical point of view, the Laplace transform (LT) is the best tool for spectral analysis. Start with

a signal $u(t)$. The Laplace transformed, $\tilde{u}(s)$ is then defined as,

$$\tilde{u}(s) = \int_{t_0}^{\infty} e^{-st} dt, \tag{3.22}$$

where $s = a - j\omega$ with $a > 0$ a real number and ω the frequency. For the problems treated in this thesis it can be shown that the LP reduces to the Fourier transform (FT). Due to the fact that the radar is an active system, the signal $u(t)$ is generated at a certain time, t_1. By choosing $t_1 > t_0$, the lower limit of the integral may be set to $-\infty$. For all practival seaclutter operations the interval between the transmission and the receival of the radiation is much smaller than 1 s. Over this interval the influence of the factor a may be neglected. Under these assumptions the LP reduces to the FT,

$$\tilde{u}(\omega) = \int_{-\infty}^{\infty} e^{j\omega t} dt, \tag{3.23}$$

There are two advantages to using the FT instead of the LT. Firstly, the FT has a more simple form, which can easily be discretised for numerical problems. Secondly, in most books on radar technology the FT and ω are used. To keep this work comparable to those books I have chosen to use the FT.

3.1.4 Harmonic time dependence

The time dependence, $e^{j\omega t}$, in equation (3.19) is usually called the harmonic time dependence. In most electromagnetic scattering problems harmonic time dependence may be assumed *a priori*. This has the advantage that the time derivatives of the fields reduce to,

$$\frac{\partial \mathbf{E}}{\partial t} = j\omega \mathbf{E}, \qquad \frac{\partial \mathbf{B}}{\partial t} = j\omega \mathbf{B}, \tag{3.24}$$

and also the derivatives of the potentials,

$$\frac{\partial \mathbf{A}}{\partial t} = j\omega \mathbf{A}, \qquad \frac{\partial \Phi}{\partial t} = j\omega \Phi. \tag{3.25}$$

Maxwell's equations may then be written as:

$$\nabla \cdot \mathbf{E} = \frac{\rho}{\epsilon_0}, \tag{3.26}$$

$$\nabla \times \mathbf{E} = -j\omega \mathbf{B}, \tag{3.27}$$

$$\nabla \cdot \mathbf{B} = 0, \tag{3.28}$$

$$\nabla \times \mathbf{B} = \mu \mathbf{J} + j\mu\epsilon\omega \mathbf{E}, \tag{3.29}$$

and the equation of continuity becomes,

$$\nabla \cdot \mathbf{J} = -j\omega\rho. \tag{3.30}$$

3.1.5 Properties of plane waves

Equation 3.19 is easily recognised as a plane wave. In this section the most important properties of such waves.

Frequency and wavenumber

For convenience the co-ordinate system is defined such that the wave is propagating along the z-axis so that equation 3.19 becomes,

$$\mathbf{E}(z,t) = \mathbf{E}_0 \Re\left(e^{j(\omega t \pm kz)}\right) = \mathbf{E}_0 \cos(\omega t \pm kz). \tag{3.31}$$

This represents two waves moving in the positive z direction ($\cos(\omega t - kz)$) and the negative z-direction ($\cos(\omega t - kz)$).

The amplitude of the **k**-vector, k, is called the wavenumber. It satisfies the dispersion relation,

$$\omega^2 \mu\epsilon = k^2. \tag{3.32}$$

The radian frequency ω is related to the frequency f and the period T by,

$$\omega = 2\pi f = 2\pi/T$$

and the wavenumber, k, is related to the wavelength, λ, by,

$$k = 2\pi/\lambda.$$

The velocity of the wave is given by,

$$v = \frac{dz}{dt} = \frac{\omega}{k} = \frac{1}{\sqrt{\mu\epsilon}}. \tag{3.33}$$

In free space $\epsilon = \epsilon_0 = 8.854 \cdot 10^{-12}$ Fm^{-1}, $\mu = \mu_0 \equiv 4\pi \cdot 10^{-7}$ Hm^{-1} and the corresponding velocity is usually denoted by $c \equiv \frac{1}{\sqrt{\mu_0\epsilon_0}} = 2.9979 \cdot 10^8$ m/s.

Power

The energy stored in the electromagnetic field within a volume V is given by,

$$\frac{1}{2}\int_V \left(\epsilon|\mathbf{E}|^2 + \frac{1}{\mu}|\mathbf{B}|^2\right) dV. \tag{3.34}$$

However, in radar technology the energy flux density of the field, i.e. the flow of energy per unit time per unit area perpendicular to the flow, is more important.

This quantity is given by the Poynting vector, $\mathbf{S}$, which can be calculated from the field by,

$$\mathbf{S} = \frac{1}{\mu}\mathbf{E}(\mathbf{r}) \times \mathbf{B}(\mathbf{r}). \tag{3.35}$$

The measured power is then the integral of the time-averaged Poynting vector over the area, A of the antenna,

$$P = \int_{\text{antenna area}} |\langle \mathbf{S} \rangle| \, dA, \tag{3.36}$$

where $\langle \ldots \rangle$ denotes the time averaging. Interesting to notice is that, due to the fact that for electromagnetic waves the $\mathbf{E}$ and $\mathbf{B}$ fields are perpendicular, the Poynting vector for electromagnetic waves becomes,

$$\mathbf{S} = \frac{1}{\mu}\mathbf{E} \times \mathbf{B} = \frac{1}{\eta}\mathbf{E}^2. \tag{3.37}$$

3.2 The scattering of plane waves

In the last few sections the fundamentals of electromagnetic theory were presented and the wave equation was derived. Moreover, a special solution of this wave equation, the plane wave, and its properties were given. In this section the scattering of such waves on different surfaces is studied. First the scattering on a plane interface is examined, then the scattering on a random surface. Several regimes of random surface scattering are identified and contemplated, high frequency, low frequency and full-wave.

3.2.1 Polarisation

For plane waves travelling in a sourceless region the $\mathbf{E}$ and $\mathbf{B}$ fields always lie in a plane perpendicular to the propagation direction. Polarisation is used to define the direction of the electromagnetic field with respect to some reference plane or axis. Polarisation is usually defined according to either of three conventions.

The first two conventions define the polarisation by the direction of the electric field. Firstly, If the direction of the electric field is horizontal respectively vertical to the transmitter/receiver of the radiation, the polarisation is defined as horizontal (H) respectively vertical (V). This convention is usually used in observational electromagnetics and will also be used throughout chapter 6 of this work. Secondly, if the direction of the electric field is parallel respectively perpendicular to the plane through which the radiation propagates, the polarisation is defined to be parallel respectively perpendicular. This convention will not be used in this work, except for validation purposes in chapter 4.

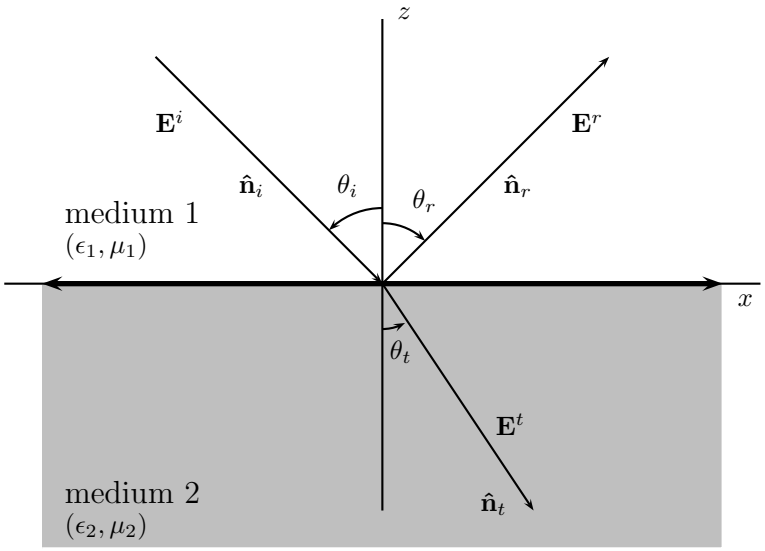

Figure 3.1: Reflection and transmission geometry

The final convention is largely mathematical. Here the polarisation of the EM-field is defined with respect to some fixed axis of the system under consideration, usually the z-axis. This approach is adopted for modelling, i.e. calculation, as well as observational purposes. In this work the convention as used in [6] is followed. If the electric field is transverse, i.e. perpendicular to, the z-axis, the polarisation is defined to be transverse electric, TE^z. This corresponds to vertical or parallel polarisation. If the magnetic field is transverse, i.e. perpendicular to, the z-axis, the polarisation is defined to be transverse magnetic, TM^z. This corresponds to horizontal or perpendicular polarisation.

3.2.2 Scattering at a plane interface

Reflection of plane waves at a plane boundary is a well-defined problem, which can be solved using Maxwell's equations, see for instance [28], chapter 33. In this section I will only present the relevant formulae.

Define the geometry of the problem as in figure (3.1). Further define the incident, reflected, and transmitted waves according to,

$$\begin{aligned} \mathbf{E}^i &= \mathbf{E}_0^i \Re\left(e^{j(\omega_i t - \mathbf{k_i}\cdot\mathbf{r})}\right), \\ \mathbf{E}^r &= \mathbf{E}_0^r \Re\left(e^{j(\omega_r t - \mathbf{k_r}\cdot\mathbf{r})}\right), \end{aligned}$$

$$\mathbf{E}^t = \mathbf{E}_0^t \Re\left(e^{j(\omega_t t - \mathbf{k_t}\cdot\mathbf{r})}\right).$$

The wavenumber, direction, and frequency of the reflected and the transmitted waves are yet unknown. However, Maxwell's equations give the following boundary conditions:

$$E_x^i + E_x^r = E_x^t, \tag{3.38}$$
$$E_y^i + E_y^r = E_y^t, \tag{3.39}$$
$$\epsilon_0\left(E_z^i + E_z^r\right) = \epsilon E_z^t, \tag{3.40}$$
$$\mathbf{B}^i + \mathbf{B}^r = \mathbf{B}^t. \tag{3.41}$$

Applying the boundary condition (3.38) to the fields gives,

$$\omega_i = \omega_r = \omega_t. \tag{3.42}$$

Substituting these results into the dispersion relation (3.32) gives

$$k_i = \sqrt{\frac{\epsilon}{\epsilon_0}} k_t, \tag{3.43}$$
$$k_i = k_r, \tag{3.44}$$

which implies that,

$$\theta_i = -\theta_r, \tag{3.45}$$
$$k_i \sin\theta_i = k_t \sin\theta_t. \tag{3.46}$$

Equation (3.46) is also known as Snell's law. The amplitudes of the fields can then be determined from the boundary condition (3.41),

$$E_0^r = R_p E_0^i, \tag{3.47}$$
$$E_0^t = T_p E_0^i, \tag{3.48}$$

where R_p and T_p are the Fresnel reflection and transmission coefficients. The p stands for either $\perp$ or $\parallel$ polarisation. The coefficients satisfy the relation, $R_p + T_p = 1$ and,

$$R_\perp = \frac{\eta_t \cos\theta_i - \eta_i \cos\theta_t}{\eta_t \cos\theta_i + \eta_i \cos\theta_t} \tag{3.49}$$
$$R_\parallel = \frac{\eta_i \cos\theta_i - \eta_t \cos\theta_t}{\eta_i \cos\theta_i + \eta_t \cos\theta_t}. \tag{3.50}$$

3.2.3 Scattering at a random surface

In section 3.1.5, the general properties of electromagnetic waves were defined. Section 3.2.2 described the scattering of such a wave on an infinite flat plane. The

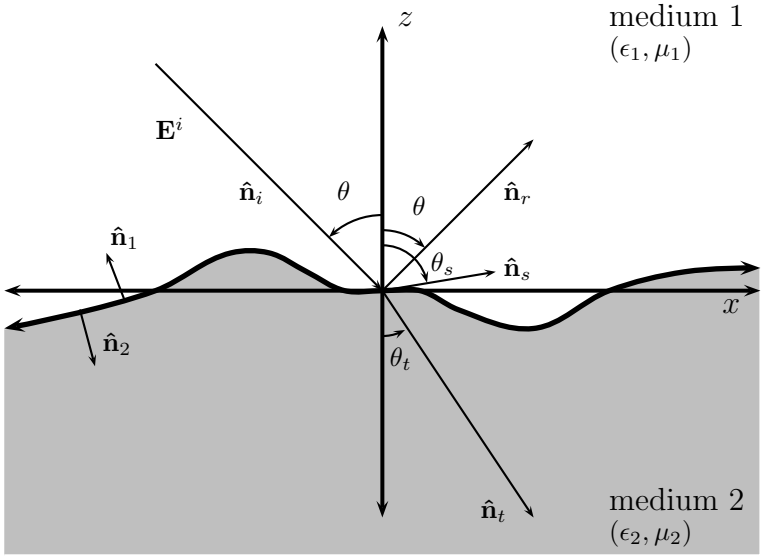

Figure 3.2: Scattering geometry

main interest of his thesis, however, is in the scattering of electromagnetic waves on the ocean surface. In general this surface is not an infinite flat plane, but a random surface, with a number of different roughness scales. For a more complete treatment of ocean surfaces the reader is referred to chapter 2. In this section the scattering from random surfaces is treated. In figure 3.2 the scattering geometry is defined.

The scattering from a random surface can be described by the Stratton-Chu equation,

$$\mathbf{E}^s = K\hat{\mathbf{n}}_s \times \int_S [\hat{\mathbf{n}} \times \mathbf{E} - \frac{\eta_s}{\mu}\hat{\mathbf{n}}_s \times (\hat{\mathbf{n}} \times \mathbf{B})]\, e^{jk_s \mathbf{r}\cdot\hat{\mathbf{n}}_s} dS, \tag{3.51}$$

where

K	=	$-jk_s e^{-jk_s R_0}/(4\pi R_0)$,
$\hat{\mathbf{n}}_S$	=	unit vector in the scattered direction
$\hat{\mathbf{n}}$	=	unit vector normal to the scattering surface
η_s	=	intrinsic impedance of the medium in which $\mathbf{E}^s$ is evaluated
k_s	=	wave number of the medium in which $\mathbf{E}^s$ is evaluated
R_0	=	range from the center of the illuminated area to the observation point.

For arbitrarily shaped surfaces this equation cannot be solved analytically. A number of techniques exist for solving the general problem and these are treated

in section 3.2.3 (full-waves techniques). However, for some simple surfaces (semi-) analytical solutions can be found, which are treated next.

High frequency approximations

Many high frequency methods exist, scattering methods such as Geometrical Optics and Physical Optics, diffraction methods, such as the Physical Theory of Diffraction and the Method of Equivalent Currents. All these methods have the following property in common: the assumption of high frequency or in other words, the frequency of the radiation is considered to be high compared to that of the variation of the surface. Another way of saying this might be that the wavelength of the radiation is much smaller that the surface structures. In the derivations this means that the ratio of wavelength and the surface size goes to zero. This considerately simplifies the scattering equations, which allows analytical solutions.

The high frequency method that is used in this thesis is ray tracing, which is based on Snells law. This method describes the incident radiation in the form of rays and the scattering object as a collection of flat patches. Subsequently, Snells law is used to evaluate the reflection of these rays by the patches. This method allows the evaluation of the illumination of an object and the determination of the direction of the scattered radiation.

Bragg (resonant) scattering

Bragg scattering is a resonant scattering mechanism related to diffraction of X-rays in solid materials. The latter process itself is related to diffraction on a grate and was first described by Bragg in 1913. The theory of scattering of electromagnetic (radar) waves on slightly rough surfaces was first described by Rice in 1951, [72]. Rice showed that the backscattered power from a rough surface was proportional to value of the surface height spectrum at a wavenumber, which is dependent on the radar parameters. His work was based on work done by Rayleigh in 1929 on acoustic scattering on rough surfaces. Crombie, [19], was one of the first to show evidence for Bragg scattering in ocean surface radar returns. The work by Rice was further improved and extended to composite surface models by a number of researchers, [65], [119], [103, 104]. For a good review on the subject see also [68].

In this section only Bragg scattering for a monostatic configuration is treated. For the derivation of the bistatic formulae the reader is referred to [104]. The scattering geometry is shown in figure 3.3. For simplicity the surface is assumed to be sinoid, with a wavelength k_B. However, the same arguments apply to random rough surfaces. A plane wave is incident on the surface, with an incidence angle θ and wavenumber $\mathbf{k}$. The scattered field is evaluated in the incident direction ($\theta_s = \theta_i = \theta$). Consider the fields along rays 1 and 2. Both rays intersect the surface

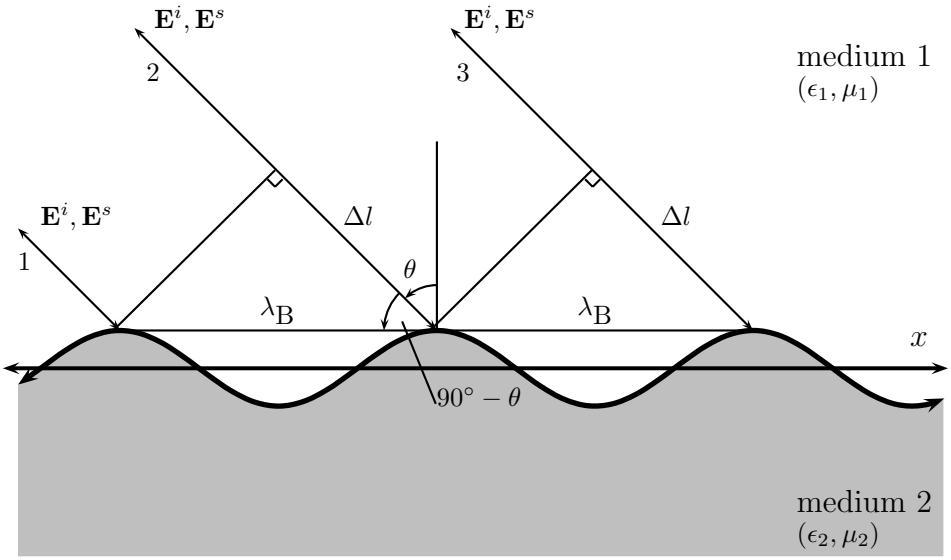

Figure 3.3: Bragg scattering

at points of equal phase of the periodicity. The path length difference between the fields along the two rays can then be expressed in terms of the wavelength, λ_B and the incidence/ scattering angle θ:

$$\Delta l = \lambda_B \cos(90° - \theta) = \lambda_B \sin\theta. \tag{3.52}$$

The total path length difference between the scattered fields will then be $2\Delta l$. Resonance will occur when the path length difference is equal to n times the wavelength, λ_r, of the incident radiation:

$$n\lambda_r = 2\Delta l = 2\lambda_B \sin\theta, \quad n = 1, 2, \ldots, \tag{3.53}$$

or

$$nk_B = 2k \sin\theta, \quad n = 1, 2, \ldots\ , \tag{3.54}$$

with k_B the wavenumber of the sinusoidal surface. The same resonance criterion also applies for rays 1 and 3 and for rays 2 and 3. Thus, the returns along the rays will be in phase, which will cause resonance. This means that a wave train with a wavenumber of nk_B will cause Bragg resonant scattering.

It can be proven mathematically, see [68], that for a random surface the spectral component of that surface which corresponds to the Bragg criterion in equation 3.54 will cause Bragg resonant scattering. First order Bragg scattering, $n = 1$, gives much higher backscattered power than higher orders, $n > 1$. For random rough surfaces, with first order Bragg spectral components, higher order Bragg scattering can be neglected.

The scattered power can be calculated from Maxwell's equations and from the Stratton-Chu equation. This derivation does not lie within the scope of this work and thus only the results will be given here. The full derivation can be found in a number of standard works on the subject, like [68]. The backscattered power will be given in terms of the normalised cross section,

$$\sigma_0 = 16\pi k^4 \left|g_{pp}\left(\theta\right)\right|^2 \Psi\left(0, k_B\right), \tag{3.55}$$

where pp indicates the receive and transmit polarisation and

$$g_{HH}\left(\theta\right) = \frac{\left(\epsilon_r - 1\right)\cos^2\theta}{\left(\cos\theta + \sqrt{\epsilon_r - \sin^2\theta}\right)^2}, \tag{3.56}$$

$$g_{VV}\left(\theta\right) = \frac{\left(\epsilon_r - 1\right)\left[\epsilon_r\left(1 + \sin^2\theta\right) - \sin^2\theta\right]\cos^2\theta}{\left(\cos\theta + \sqrt{\epsilon_r - \sin^2\theta}\right)^2}, \tag{3.57}$$

$$g_{HV} = g_{VH} = 0. \tag{3.58}$$

The quantity $\Psi\left(\phi, k\right)$ is the two dimensional surface displacement spectrum. This quantity will be treated more in-depth in chapter 2.

Full wave methods

There are many so-called full-wave methods. They all have one thing in common: they directly solve Maxwell's equations for a given problem or set of problems to obtain a full-wave solution. The problem is usually written in the form of an integral equation, which is then solved numerically. In this section one of the most common such methods, the Method of Moments (MoM) is presented. For more information on this method the reader is referred to [34] and [123]. The method of moments is a standard recipe for solving linear equations. Consider the following equation,

$$Z(f) = h, \tag{3.59}$$

where Z is a linear operator, h is the known forcing vector and f is the unknown quantity. The first step is to expand f into a series of basisfunctions,

$$f = \sum_n a_n f_n, \tag{3.60}$$

with a_n as yet unknown constants and f_n known basisfunctions. Substituting this expansion into 3.59 gives,

$$\sum_n a_n Z(f_n) = h. \tag{3.61}$$

The next step is to define a set of testing functions g_m and taking the inner product with each g_m, resulting in,

$$\sum_n a_n \langle g_m, Z f_n \rangle = \langle g_m, h \rangle. \tag{3.62}$$

But this is a series of equations leading to the following matrix equation

$$[Z_m n][a_n] = [V_m], \tag{3.63}$$

with

$$[Z_m n] = \begin{bmatrix} \langle g_1, Zf_1\rangle & \langle g_1, Zf_2\rangle & \cdots \\ \langle g_2, Zf_1\rangle & \langle g_2, Zf_2\rangle & \cdots \\ \cdots\cdots\cdots\cdots\cdots\cdots & & \end{bmatrix} \tag{3.64}$$

$$[a_n] = \begin{bmatrix} a_1 \\ a_2 \\ \vdots \end{bmatrix} \qquad [V_m] = \begin{bmatrix} \langle g_1, h_1\rangle \\ \langle g_2, h_2\rangle \\ \vdots \end{bmatrix}. \tag{3.65}$$

The matrix equation given above can then be solved with standard linear algebra techniques.

In chapter 5 this method is used to solve the scattering from breaking waves. In that chapter an integral equation is derived of the form,

$$\mathbf{E}^i = \int_S \mathbf{J}\mathbf{G}dS, \tag{3.66}$$

where $\mathbf{E}^i = \mathbf{E}^i(\mathbf{r})$ is the incident field, S represents the scattering surface, $\mathbf{J} = \mathbf{J}(\mathbf{r}')$ is the current induced by the incident field and $\mathbf{G} = \mathbf{G}(\mathbf{r}, \mathbf{r}')$ is Green's function. The coordinates $\mathbf{r}$ and $\mathbf{r}'$ are unimportant for the following derivation and will thus be omitted. Studying 3.66 the different elements for the MoM recipe can be identified:

$$\int_S \mathbf{J}\mathbf{G}dS \leftrightarrow Z(f), \qquad \mathbf{J} \leftrightarrow f, \qquad \mathbf{E}^i \leftrightarrow h. \tag{3.67}$$

Thus $\mathbf{J}$ is expanded using basis functions $\mathbf{f}_n$,

$$\mathbf{J} = \sum_n I_n \mathbf{f}_n, \tag{3.68}$$

resulting in,

$$\mathbf{E}^i = \sum_n I_n \int_S \mathbf{f}_n \mathbf{G} dS. \tag{3.69}$$

The next step is the introduction of testing functions $\mathbf{g}_m$ and taking the inner product,

$$\langle \mathbf{g}_m, \mathbf{E}^i\rangle = \sum_n I_n \langle \mathbf{g}_m, \int_S \mathbf{f}_n \mathbf{G} dS\rangle. \tag{3.70}$$

This recipe then gives us the following matrix equation,

$$[Z_{mn}][I_n] = [V_m], \tag{3.71}$$

with

$$[Z_{mn}] = \begin{bmatrix} \langle g_1, \int_S \mathbf{f}_1 \mathbf{G} dS \rangle & \langle g_1, \int_S \mathbf{f}_2 \mathbf{G} dS \rangle & \cdots \\ \langle g_2, \int_S \mathbf{f}_1 \mathbf{G} dS \rangle & \langle g_2, \int_S \mathbf{f}_2 \mathbf{G} dS \rangle & \cdots \\ \cdots & \cdots & \end{bmatrix} \tag{3.72}$$

$$[I_n] = \begin{bmatrix} I_1 \\ I_2 \\ \vdots \end{bmatrix}, \qquad [V_m] = \begin{bmatrix} \langle g_1, \mathbf{E}_1^i \rangle \\ \langle g_2, \mathbf{E}_2^i \rangle \\ \vdots \end{bmatrix}. \tag{3.73}$$

3.3 Radar observations

3.3.1 Power and radar cross section

In this chapter the scattering of electromagnetic waves on different types of surfaces was treated. In radar technology the power, P_r, received by a radar after being scattered on a surface is calculated from the power, transmitted by the radar through the radar equation:

$$P_r = \frac{P_t G_t G_r \lambda^2 \sigma}{(4\pi)^3 r_t^2 r_r^2}, \tag{3.74}$$

where P_t is the transmitted power, G_r and G_t are the gains of the receiving and transmitting antennas, the r_r and r_t are the ranges between the receiving respectively transmitting systems and the scattering surface and λ is the radar wavelength. For monostatic systems often $G_r = G_t = G$ and $r_r = r_t = r$, so that the radar equation becomes,

$$P_r = \frac{P_t G^2 \lambda^2 \sigma}{(4\pi)^3 r^4}. \tag{3.75}$$

The parameter σ in the equation is the so-called radar cross section. This is a parameter describing the scattering properties of the surface. It is not dependent on the properties of the radar system or on the range to and from the system. This makes the cross section a convenient parameter for expressing the scattering from the surface.

The three-dimensional radar cross section, σ, of is defined as,

$$\sigma = 4\pi \lim_{r \to \infty} r^2 \frac{|\mathbf{E}^s|^2}{|\mathbf{E}^i|^2}, \tag{3.76}$$

where r is the range between the surface and the receiver. In chapters 4 and 5, the scattering from two-dimensional surfaces is considered. For such surfaces the definition of the cross section is slightly different:

$$\sigma = 2\pi \lim_{r\to\infty} r\frac{|\mathbf{E}^s|^2}{|\mathbf{E}^i|^2}, \tag{3.77}$$

Often the normalised cross section, σ_0, is used. This quantity is defined as the cross section per unit area of the scattering surface.

Chapter 4

The Method of Moments applied to radar scattering

In chapter 2 a mathematical description of the shape of the ocean surface was given. It was shown that especially breaking waves can form complex shapes. To calculate the RCS of such shapes, approximate methods such as physical optics or ray tracing are not suitable. Such methods produce erroneous results because of the small size of the breaking waves with respect to the radar wavelength. Hence, for such objects full wave methods are needed. In this chapter the evaluation of radar scattering from such arbitrary surfaces using the Method of Moments is described.

The general formulation of the Method of Moments (MoM) was presented in section 3.2.3. In this chapter that recipe is applied to the problem of scattering on a randomly shaped 2D object, composed of perfectly conducting material. The problem is defined in detail in section 4.1. The integral equation for this problem is derived in section 4.2. The Method of Moments is applied to this equation to obtain a matrix equation, as is shown in section 4.3. The solution of this matrix equation gives the induced current, which in turn generates the scattered field, as is shown in section 4.4. The implementation of this MoM algorithm is treated in section 4.5. Finally, in section 4.6, a number of standard objects are evaluated as a validation of the method.

4.1 Problem definition

This section presents the problem to be solved in this chapter. Throughout this chapter we assume that the scattering configuration is located in a standard three-dimensional Cartesian space, with coordinates $(\mathbf{x}, \mathbf{y}, \mathbf{z})$. The time is measured on

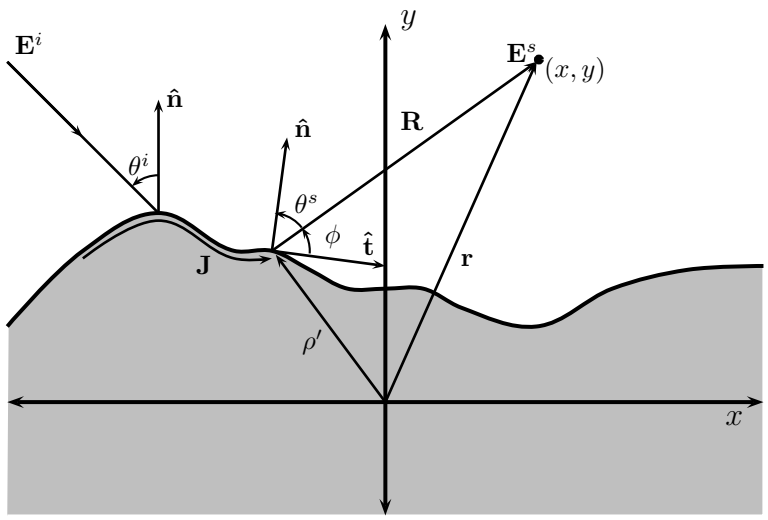

Figure 4.1: Geometry of the scattering problem.

a standard clock, which is in rest compared to the origin of our coordinate system. The MoM algorithm presented in this chapter is two-dimensional in nature. This means that all objects in this chapter may vary in two dimensions, $(\mathbf{x}, \mathbf{y})$, only. Objects have an infinite extend in the third dimension, $\mathbf{z}$, in which none of the properties vary.

The main interest lies in the evaluation of breaking wave profiles. A sequence of these profiles goes through a variety of shapes, from a slightly curved contour to a strongly curved, nearly cylindrical, jet shape. In the third dimension, along the crest, the profiles vary slowly, which explains why a two-dimensional evaluation is sufficient. In those two dimensions, the method needs to be able to evaluate an arbitrary shape that is as general as possible. Such a geometry is shown in figure 4.1. An electromagnetic field, denoted by $\mathbf{E}^i = \left(E_x^i, E_y^i, E_z^i\right)$ is incident on the surface. It induces a surface current $\mathbf{J} = (J_x, J_y, J_z)$, which in turn induces a scattered field $\mathbf{E}^s = \left(E_x^s, E_y^s, E_z^s\right)$. Throughout this chapter the 2D coordinate $\mathbf{r} = (\mathbf{x}, \mathbf{y})$ is used to denote a position in this 2D space. For coordinates on the scattering surface the symbol ρ is used. Also, primed quantities are used to denote source points and unprimed quantities to denote observation points.

For this 2D problem, the polarisation conventions as defined in section 3.2.1 are used. If the magnetic field is transverse to the $\mathbf{z}$-axis, the polarisation is said to be TM^z. If the electric field is transverse to the $\mathbf{z}$-axis, the polarisation is said to be TE^z. Due to the fact that physical properties are considered to be invariant along

the **z**-axis, these two polarisations are mutually independent.

In this work only perfectly conducting materials (PEC) are considered. For a surface of PEC material the boundary condition follows from the interface boundary condition that the total tangential electric field is zero upon crossing an interface discontinuity. This is expressed in the following form:

$$\hat{\mathbf{n}} \times \mathbf{E}^i + \hat{\mathbf{n}} \times \mathbf{E}^s = \mathbf{E}^{\text{tot}} = 0, \tag{4.1}$$

which implies that:

$$\hat{\mathbf{n}} \times \mathbf{E}^i = -\hat{\mathbf{n}} \times \mathbf{E}^s. \tag{4.2}$$

This boundary condition is used in the next section for the derivation of the integral equation.

4.2 Integral equation derivation

In this section, the electric field integral equation (EFIE) will be derived from Maxwell's equations. Starting out from Maxwell's equations the electric field integral equation is derived, which couples the known incident field with the current that induces the scattered field. Much of the material in this section has been taken from [6, 34] and [123].

It is convenient to write this derivation in terms of the electromagnetic potentials. Assume harmonic time dependence and define the vector, $\mathbf{A}(\mathbf{r})$, and scalar, $\Phi(\mathbf{r})$, potentials according to equations (3.8) and (3.9):

$$\mathbf{E}(\mathbf{r}) = -\nabla\Phi(\mathbf{r}) - j\omega\mathbf{A}(\mathbf{r}) \tag{4.3}$$

$$\mathbf{B}(\mathbf{r}) = \nabla \times \mathbf{A}(\mathbf{r}). \tag{4.4}$$

Taking the curl on both sides of equation 4.4 and using vector identity $\nabla\times(\nabla\times\mathbf{A}) = \nabla(\nabla\cdot\mathbf{A}) - \nabla^2\mathbf{A}$ gives:

$$\nabla \times \mathbf{B}(\mathbf{r}) = \nabla\left(\nabla \cdot \mathbf{A}(\mathbf{r})\right) - \nabla^2\mathbf{A}(\mathbf{r}). \tag{4.5}$$

Comparing this with Maxwell's equation (3.29),

$$\nabla \times \mathbf{B}(\mathbf{r}) = \mu\mathbf{J}(\mathbf{r}) + j\omega\mu\epsilon\mathbf{E}(\mathbf{r}), \tag{4.6}$$

and substituting equation 4.3 gives:

$$\begin{aligned} \nabla^2\mathbf{A}(\mathbf{r}) + k^2 A(\mathbf{r}) &= -\mu\mathbf{J}(\mathbf{r}) + \nabla\left(\nabla \cdot \mathbf{A}(\mathbf{r})\right) + \nabla\left(j\omega\epsilon\mu\Phi(\mathbf{r})\right) \\ &= -\mu\mathbf{J}(\mathbf{r}) + \nabla\left(\nabla \cdot \mathbf{A}(\mathbf{r}) + j\omega\mu\epsilon\Phi(\mathbf{r})\right). \end{aligned} \tag{4.7}$$

To resolve the ambiguity of the electromagnetic field, the divergence of $\mathbf{A}$ is set according to the Lorentz gauge,

$$\nabla \cdot \mathbf{A}(\mathbf{r}) = -j\omega\mu\epsilon\Phi(\mathbf{r}), \tag{4.8}$$

which upon substitution into 4.7 gives

$$\nabla^2 \mathbf{A}(\mathbf{r}) + k^2 \mathbf{A}(\mathbf{r}) = -\mu \mathbf{J}(\mathbf{r}). \tag{4.9}$$

Following the derivation in section A.1, the general solution of this equation is:

$$\mathbf{A}(\mathbf{r}) = \frac{\mu}{4j} \int_S \mathbf{J}(\mathbf{r}') G(\mathbf{r}, \rho') dS', \tag{4.10}$$

where $G(\mathbf{r}, \rho')$ is Green's function. For the 2D problem considered in this chapter, it takes the form of A.21. The primed quantities denote the source points, while the unprimed ones denote the observation points. Thus equation 4.10 leads to the scattered (electromagnetic) vector potential at the observation point $\mathbf{r}$ due to the current $\mathbf{J}$ on the surface S.

This, in turn, allows the calculation of the electric field induced by the current $\mathbf{J}$. Applying the Lorentz gauge to equation 4.3 gives,

$$\mathbf{E}^s(\mathbf{r}) = -j\omega \mathbf{A}(\mathbf{r}) - \frac{j}{\omega \mu \epsilon} \nabla \left(\nabla \cdot \mathbf{A}(\mathbf{r}) \right), \tag{4.11}$$

and substituting equation 4.10 gives:

$$\mathbf{E}^s(\mathbf{r}) = -\frac{j\eta}{k} \left[k^2 \int_S \mathbf{J}(\rho') G(\mathbf{r}, \rho') dS' + \nabla \int_S \nabla' \cdot \mathbf{J}(\rho') G(\mathbf{r}, \rho') dS' \right]. \tag{4.12}$$

This equation then allows the calculation of the field, scattered by the surface S. Setting both source and observation points on the scatterer and applying the boundary condition, equation 4.2, gives the EFIE:

$$\mathbf{E}^i(\rho) = \frac{j\eta}{k} \left[k^2 \int_S \mathbf{J}(\rho') G(\rho, \rho') dS' + \nabla \int_S \nabla' \cdot \mathbf{J}(\rho') G(\rho, \rho') dS' \right]. \tag{4.13}$$

This is called an integral equation as it allows the calculation of the current from the known quantity $\mathbf{E}^i$. In the next subsection this equation will be adapted to both TM and TE polarisation.

4.2.1 The electric field integral equation for TM and TE polarisations

In the previous subsection the general form of the 2D electric field integral equation (EFIE) was derived. In this subsection this general form is adapted to the 2D scattering problem described in section 4.1. The problem is treated separately for the two polarisations, TM^z and TE^z. In the rest of this chapter the superscripts ^{z} will be implied.

TM polarisation

In the case of TM polarisation the only non-zero component of the $\mathbf{E}$ field is $E_z(\rho)$ and, correspondingly, the only non-zero component of $\mathbf{J}$ is $J_z(\rho')$. This means that for our geometry, the $\nabla' \cdot \mathbf{J}(\rho')$ term is zero, so that equation 4.13 reduces to:

$$\mathbf{E}^i(\rho) = j\eta k \int_S \mathbf{J}(\rho')G(\rho,\rho')dS' = \frac{\eta k}{4}\int_S J_z(\rho')H_0^{(2)}(|\rho-\rho'|)d\rho'. \tag{4.14}$$

TE polarisation

In the case of TE polarisation we have the boundary condition: $\hat{\mathbf{n}} \times \left(\mathbf{E}^i + \mathbf{E}^s\right) = 0$. In other words, the nonzero elements of the $\mathbf{E}$ fields are the E_x and the E_y, while now the E_z is zero. This means that the $\nabla' \cdot \mathbf{J}$ term does not reduce to zero and as a consequence the TE-EFIE becomes:

$$\begin{aligned}
\mathbf{E}^i(r) &= \frac{j\eta}{k}\left[k^2\int_S \mathbf{J}(\rho')G(\rho,\rho')dS' + \nabla\int_S \nabla'\cdot\mathbf{J}(\rho')G(\rho,\rho')dS'\right] \qquad (4.15)\\
&= \frac{\eta}{4k}\left[k^2\int_S \mathbf{J}(\rho')H_0^{(2)}(|\rho-\rho'|)dS' + \nabla\int_S \nabla'\cdot\mathbf{J}(\rho')H_0^{(2)}(|\rho-\rho'|)dS'\right]
\end{aligned}$$

Separating the x and y components and expanding the derivatives gives:

$$\begin{aligned}
E_x^i(\rho) &= \frac{\eta}{4k}\left[\left(k^2+\frac{\partial^2}{\partial x^2}\right)\int_S \mathbf{J}(\rho')H_0^{(2)}(|\rho-\rho'|)d\rho'\right],\\
E_y^i(\rho) &= \frac{\eta}{4k}\frac{\partial^2}{\partial x\partial y}\int_S \mathbf{J}(\rho')H_0^{(2)}(|\rho-\rho'|)d\rho'. \qquad (4.16)
\end{aligned}$$

Interchanging the differentiation and integration, and performing the former it can be shown, see B.1, that for our geometry these equations reduce to:

$$\begin{aligned}
E_x^i(\rho) &= \frac{k\eta}{8}\int_S \mathbf{J}(\rho')\left[H_0^{(2)}(|\rho-\rho'|) + H_2^{(2)}(|\rho-\rho'|)\cos(2\phi)\right]d\rho',\\
E_y^i(\rho) &= \frac{k\eta}{8}\int_S \mathbf{J}(\rho')H_2^{(2)}(|\rho-\rho'|)\sin(2\phi)d\rho'. \qquad (4.17)
\end{aligned}$$

4.3 Matrix equation derivation

The integral equations, 4.14 and 4.17, derived in the previous section are continuous equations. These equations cannot be solved using analytical methods. To obtain a solution of these equations, numerical techniques have to be used. One such numerical techniques is the Method of Moments, which was described in section 3.2.3. This method allows us to convert the integral equations into a matrix equation of the form,

$$ZI = V. \tag{4.18}$$

Two steps need to be taken for this: firstly, the discretisation of the induced surface current by means of expansion functions and, secondly, the testing procedure, which discretises the integration.

4.3.1 Expansion of the current

As explained in section 3.2.3 the first step in the MoM is the expansion of the induced surface current. This is done in two steps. Firstly, the basisfunctions, which are used for the expansion, need to be chosen. Secondly, the surface is divided into some grid and the basisfunctions are applied to this grid to expand the surface current.

The choice of the basisfunctions

For expansion of the physical quantities, many possible types of basisfunctions may be used, such as pulse functions, rooftop (triangular), piecewise sinusoid and many others. I have opted to use subdomain pulse functions. The advantage of pulse functions is twofold. Firstly, pulse functions have a simple form, which do not add extra terms to the integrand of the integral equation. Secondly, pulse function will cause only a single singularity, one on the diagonal term of the matrix. The main disadvantage of pulse functions is the fact that they do not follow the surface in high detail. This forces the use of a higher number of sampling points to get a sufficiently detailed surface description for the analysis. After careful consideration the simplicity of the pulse functions was preferred over the higher accuracy of higher order basisfunctions.

Expansion procedure

Now that the basisfunctions have been chosen, the surface needs to be discretised. Assume the surface is built out of N points $\rho_n = (\rho_1, \rho_2, \rho_3, \ldots, \rho_N)$, where $\rho_n = (x_n, y_n)$. The surface is assumed to be linear between the grid points. This

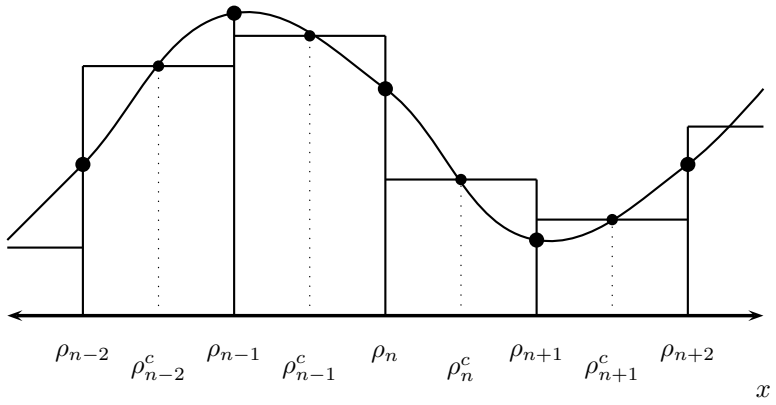

Figure 4.2: Definition of the pulse basis functions.

will introduce some slight numerical errors, but it will be shown that if the sampling is fine enough, the errors are negligible. In effect the continuous surface is approximated by a piecewise linear surface. On the grid ρ_n the pulse basis function are defined as:

$$P_n(\rho) = \begin{cases} 1 & \rho_n \leq \rho < \rho_{n+1} \\ 0 & \text{elsewhere} \end{cases}, \tag{4.19}$$

An example of pulse functions is given in figure 4.2. The matchpoints for the pulse functions are the midpoints of the grid (dotted lines). This is important for the point-matching in the next section.

Using these basis functions, the current may now be approximated by,

$$\mathbf{J} = \sum_{n=1}^{N} I_n P_n \tag{4.20}$$

Applying this expansion to the TM integral equation (4.14) gives

$$\mathbf{E}^i(r) = \frac{\eta k}{4} \sum_{n=1}^{N} \int_{\rho_n}^{\rho_{n+1}} I_n H_0^{(2)}(|\rho - \rho'_n|) d\rho'_n. \tag{4.21}$$

And applying it to the TE integral equation (4.17) gives

$$\begin{aligned} E^i_x(\rho) &= \frac{k\eta}{8} \sum_{n=1}^{N} \int_{\rho_n}^{\rho_{n+1}} I_n \left[H_0^{(2)}(|\rho - \rho'_n|) + H_2^{(2)}(|\rho - \rho'|) \cos(2\phi) \right] d\rho'_n, \\ E^i_y(\rho) &= \frac{k\eta}{8} \sum_{n=1}^{N} \int_{\rho_n}^{\rho_{n+1}} I_n H_2^{(2)}(|\rho - \rho'_n|) \sin(2\phi) d\rho'_n. \end{aligned} \tag{4.22}$$

4.3.2 Point-matching

The next step is the testing procedure. Following [6], we use point matching. This means that the Dirac delta function is used as testing function. Setting the match point to the midpoints of the pulse functions of equation 4.19, we may write equation 4.21 as:

$$\mathbf{E}^i(\rho_m^c) = \frac{\eta k}{4} \sum_{n=1}^{N} \int_{\rho_n}^{\rho_{n+1}} I_n H_0^{(2)}(|\rho_m^c - \rho_n'|) d\rho_n'. \tag{4.23}$$

and equation 4.22 as

$$\begin{aligned} E_x^i(\rho_m^c) &= \frac{k\eta}{8} \sum_{n=1}^{N} \int_{\rho_n}^{\rho_{n+1}} I_n \left[H_0^{(2)}(|\rho_m^c - \rho_n'|) + H_2^{(2)}(|\rho_m^c - \rho'|) \cos(2\phi) \right] d\rho_n', \\ E_y^i(\rho_m^c) &= \frac{k\eta}{8} \sum_{n=1}^{N} \int_{\rho_n}^{\rho_{n+1}} I_n H_2^{(2)}(|\rho_m^c - \rho_n'|) \sin(2\phi) d\rho_n'. \end{aligned} \tag{4.24}$$

With this we have completed a procedure to obtain a set of N equations (in m) with N unknowns, I_n. These can be written in the form of a square matrix equation as follows,

$$[Z][I] = [V], \tag{4.25}$$

in which $[Z] = Z_{mn}$ denotes the interaction matrix obtained from the testing procedure, $[I] = I_n$ denotes the unknown current components obtained from the expansion and $[V] = V_m = (\mathbf{E}^i(\rho_m))$ denotes the forcing vector obtained from the testing of the incident field. Thus for TM fields Z_{mn} becomes:

$$Z_{mn} = \frac{\eta k}{4} \int_{\rho_n}^{\rho_{n+1}} H_0^{(2)}(|\rho_m^c - \rho_n'|) d\rho_n'. \tag{4.26}$$

And for TE fields:

$$\begin{aligned} Z_{mn}^x &= \frac{k\eta}{8} \int_{\rho_n}^{\rho_{n+1}} \left[H_0^{(2)}(|\rho_m^c - \rho_n'|) + H_2^{(2)}(|\rho_m^c - \rho_n'|) \cos(2\phi) \right] d\rho_n', \\ Z_{mn}^y &= \frac{k\eta}{8} \int_{\rho_n}^{\rho_{n+1}} H_2^{(2)}(|\rho_m^c - \rho_n'|) \sin(2\phi) d\rho_n'. \end{aligned} \tag{4.27}$$

These matrix equations can now be implemented into a computer code. This is mostly a straightforward process. Special care should be taken, however, for the selfpatch, i.e. the diagonal of the matrix. In this case, the argument of the Hankel functions will become zero. This leads to a singularity in the integral, which needs to be handled with care. This issue is treated, amongst others, in section 4.5.

4.4 Calculating the scattered field

Once the surface current has been calculated, the scattered field can be determined by using the integral formulation of the scattered field from which the integral equation was derived. Start with equation 4.12, the integral relation for the scattered field. Deriving separate relations for the two polarisations as shown in section 4.2.1 and discretising the relations as shown in section 4.3 gives the following relations for the scattered field at some observation point $\mathbf{r}$:

$$\mathbf{E}_z^s(\mathbf{r}) = -\frac{\eta k}{4} \sum_{n=1}^{N} \int_{\rho_n}^{\rho_{n+1}} I_n H_0^{(2)}(|\mathbf{r} - \rho_n'|) d\rho_n'. \tag{4.28}$$

for TM, and

$$\begin{aligned} \mathbf{E}_x^s(\mathbf{r}) &= -\frac{k\eta}{8} \sum_{n=1}^{N} \int_{\rho_n}^{\rho_{n+1}} I_n \left[H_0^{(2)}(|\mathbf{r} - \rho_n'|) + H_2^{(2)}(|\mathbf{r} - \rho'|) \cos(2\phi) \right] d\rho_n', \\ \mathbf{E}_y^s(\mathbf{r}) &= -\frac{k\eta}{8} \sum_{n=1}^{N} \int_{\rho_n}^{\rho_{n+1}} I_n H_2^{(2)}(|\mathbf{r} - \rho_n'|) \sin(2\phi) d\rho_n'. \end{aligned} \tag{4.29}$$

for TE polarisation. These equations allow us to calculate the scattered field induced by the calculated surface current $J = \sum_{n=1}^{N} I_n P_n$. In the next section some implementation issues are treated. In section 4.6 a number of examples are shown of calculations performed with this MoM code for validation purposes.

4.5 Implementation

In the two previous sections the MoM algorithm was derived which allows the evaluation of arbitrary 2D objects. In this section a number of implementation issues are treated. The implementation of the Method of Moments, described in the previous sections is a straightforward process. It consists of four parts:

1. The numerical description of the scattering object and the incident ratio.
2. The implementation of the matrix equation, 4.25, for both polarisations.
3. Solving the matrix equation to obtain the surface current.
4. Calculating the field induced by the surface current.

As mentioned, performing these four steps is mostly a straightforward process and has been done both in MATLAB and FORTRAN. The former programming

language was found to be convenient for the first implementation and testing of the MoM algorithm. For its greater speed and wider spread, the algorithm was also coded in FORTRAN. The details of these codes will not be treated here. However, a few issues deserve more attention, in particular: resolving the singularities, solving the matrix equation and optimisation of the MoM code. These issues are treated in the following three subsections.

4.5.1 Singularities of the self-patch

Two types of singularities may occur on the diagonal of the matrix equation, namely a quadratic and a logarithmic singularity. In this section we will describe the way that these singularities are resolved in this thesis. Both of the singularities occur at TE and only the logarithmic one at TM. In section 4.5.3 it is shown that the latter is of the same type as one of the singularities at TE. Let us thus start with the TE matrix equation:

$$\begin{aligned}
\mathbf{E}_x^i(\rho^c) &= \frac{k\eta}{8}\sum_{n=1}^{N}\int_{\rho_n}^{\rho_{n+1}}\left[H_0^{(2)}(k|\rho^c-\rho'_n|)+H_2^{(2)}(k|\rho^c-\rho'|)\cos(2\phi)\right]d\rho'_n,\\
\mathbf{E}_y^i(\rho^c) &= \frac{k\eta}{8}\sum_{n=1}^{N}\int_{\rho_n}^{\rho_{n+1}}H_2^{(2)}(k|\rho^c-\rho'_n|)\sin(2\phi)d\rho'_n. \qquad (4.30)
\end{aligned}$$

To reduce the problem to its essentials it is convenient to apply this equation to the scattering on a flat plate lying along the x-axis, so that $\rho = x$. Hence the equations become:

$$\begin{aligned}
\mathbf{E}_x^i(x_m^c) &= \frac{k\eta}{8}\sum_{n=1}^{N}\int_{x_n}^{x_{n+1}}\left[H_0^{(2)}(k|x_m^c-x'_n|)+H_2^{(2)}(k|x_m^c-x'_n|)\cos(2\phi)\right]dx'_n,\\
\mathbf{E}_y^i(x_m^c) &= \frac{k\eta}{8}\sum_{n=1}^{N}\int_{x_n}^{x_{n+1}}H_2^{(2)}(k|x_m^c-x'_n|)\sin(2\phi)dx'_n. \qquad (4.31)
\end{aligned}$$

Studying the geometry of figure 4.1, it is easily seen that $2\phi = 0$, which means that $\sin(2\phi) = 0$ and $\cos(2\phi) = 1$, so that the only non zero component of the electric field is $\mathbf{E}_x^i$:

$$\begin{aligned}
\mathbf{E}_x^i(x_m^c) &= \frac{k\eta}{8}\sum_{n=1}^{N}\int_{x_n}^{x_{n+1}}\left[H_0^{(2)}(k|x_m^c-x'_n|)+H_2^{(2)}(k|x_m^c-x'_n|)\right]dx'_n,\\
&= \frac{k\eta}{8}\sum_{n=1}^{N}\left[\int_{x_n}^{x_{n+1}}H_0^{(2)}(k|x_m^c-x'_n|)dx'_n+\int_{x_n}^{x_{n+1}}H_2^{(2)}(k|x_m^c-x'_n|)dx'_n\right]
\end{aligned}$$

$$\mathbf{E}_y^i(x_m^c) \quad = \quad 0.$$

For the self-patch m is equal to n. Applying this to the equation above and dropping the index, we are left with two types of integral:

$$I1 \quad = \quad \int_{x_n}^{x_{n+1}} H_0^{(2)}(k|x^c - x'|)dx' \tag{4.32}$$

$$I2 \quad = \quad \int_{x_n}^{x_{n+1}} H_2^{(2)}(k|x^c - x'|)dx' \tag{4.33}$$

Both these integrals contain Hankel functions of the second kind, both of which have a singularity when $x' = x^c$. They are treated here separately. In this section certain relations from [1] are used. They will be denoted as (A&Sx), where the x denotes the equation number from [1].

The H_0^2 singularity

Referring to equation A.27, H_0^2 can be written in the form of an infinite series. Explicitly writing out the terms we get:

$$\begin{array}{lcll} k=0 & \rightarrow & \frac{2i}{\pi}\left\{\frac{\pi}{2i} - \gamma - \ln\left(\frac{z}{2}\right)\right\} & \sim \quad \frac{2}{\pi i}\ln\left(\frac{z}{2}\right) \\ k=1 & \rightarrow & \frac{2i}{\pi}\left\{\frac{\pi}{2i} + \psi(2) - \ln\left(\frac{z}{2}\right)\right\} - \frac{1}{4}z^2 & \sim \quad \frac{2}{\pi i}z^2\ln\left(\frac{z}{2}\right) \\ \vdots & & \vdots & \quad \vdots \\ k=n & \rightarrow & \frac{2i}{\pi}\left\{\frac{\pi}{2i} + \psi(n+1) - \ln\left(\frac{z}{2}\right)\right\}\frac{\left(-\frac{1}{4}z^2\right)^n}{(n!)^2} & \sim \quad \frac{2}{\pi i}z^{2n}\ln\left(\frac{z}{2}\right) \end{array} \tag{4.34}$$

This reveals that the singularity occurs in the first term ($k = 0$). This is due to the factor $\ln(z/2)$. The logarithm can be integrated around zero according to (A&S4.1.49):

$$\int_0^a \ln\left(\frac{z}{2}\right) = \left[z\ln\left(\frac{z}{2}\right) - z\right]_0^a = a\ln\left(\frac{a}{2}\right) - a. \tag{4.35}$$

Here the fact is used that the limit for $z \rightarrow 0$ of $z^n\ln(z)$ is zero for $n > 0$, (A&S4.1.31).

The higher terms are all of the order of $z^{2n}\ln(z/2)$, with $(n \geq 0)$. Again using the limit (A&S4.1.31) it is easily seen that this term goes to zero for $z \rightarrow 0$, which means that the higher terms do not contain singularities. Moreover, due to the increasing order of the factor z^{2n}, the series converges rapidly for small values of z.

This then allows us to resolve the H_0^2 singularity. By extracting the singularity-causing logarithmic term from the Hankel function, only finite terms are retained,

which may be treated numerically. The singular term can then be treated separately as was shown above:

$$\begin{aligned} I1 &= \int_{x_n}^{x_{n+1}} H_0^{(2)}(k|x^c - x'|)dx', \\ &= -\int_{-\Delta x/2}^{\Delta x/2} H_0^{(2)}(k|x^c - x'|)d(x^c - x'), \\ &\quad \text{Substitute: } q = (x^c - x'), \\ &= -2\int_0^{\Delta x/2} H_0^{(2)}(kq)dq \\ &= -2\int_0^{\Delta x/2} H_0^{(2)}(kq) - \frac{2}{\pi i}\ln\left(\frac{kq}{2}\right)dq - 2\int_0^{\Delta x/2}\frac{2}{\pi i}\ln\left(\frac{kq}{2}\right)dq, \\ &= -2\int_0^{\Delta x/2} H_0^{(2)}(kq) - \frac{2}{\pi i}\ln\left(\frac{kq}{2}\right)dq - \frac{2\Delta x}{\pi i}\left\{\ln\left(\frac{k\Delta x}{2}\right) - 1\right\}, \end{aligned}$$

where $\Delta x = |x_{n+1} - x_n|$. As explained above, the remaining integral can be evaluated numerically, because the integrant, i.e. the Hankel function with the singular logarithmic term subtracted, only contains finite elements. This is best done by using the series expansion where the logarithmic term is internally subtracted.

The H_2^2 singularity

This singularity is more complicated to deal with. From A&S9.1.9 it follows that the H_2^2 function behaves as z^{-2} around zero. The integral over z^{-2} is not simply evaluated. Fortunately, an approximation of this singularity can be found in [6]. Around zero, the integral may be approximated by:

$$\begin{aligned} I2 &= \int_{x_n}^{x_{n+1}} H_2^{(2)}(k|x^c - x'|)dx' \\ &= \int_{x^c-\epsilon/2}^{x_{n+1}} H_2^{(2)}(k|x^c - x'|)dx' + \int_{x_n}^{x^c+\epsilon/2} H_2^{(2)}(k|x^c - x'|)dx' \\ &+ \int_{x^c-\epsilon/2}^{x^c+\epsilon/2} H_2^{(2)}(k|x^c - x'|)dx' \end{aligned}$$

$$= \int_{x^c-\epsilon/2}^{x_{n+1}} H_2^{(2)}(k|x^c - x'|)dx' + \int_{x_n}^{x^c+\epsilon/2} H_2^{(2)}(k|x^c - x'|)dx'$$
$$+ \frac{\epsilon i}{\pi}\left\{1 - \frac{16}{(k\epsilon)^2}\right\}, \tag{4.36}$$

where $\epsilon < \Delta x$ is a small number. In effect the part on which the singularity occurs is cut out of the integral and replaced by the approximation from [6]. We have thoroughly tested this approximation and found that it works well for values of $\epsilon \sim \lambda/100$, which is well within the preferred patch size of $\lambda/20$

4.5.2 Solving the matrix equation

Special care should be taken when solving the matrix equation as derived in the previous section. Due to the strong singularities on the diagonal of the matrix, it is not very well conditioned. This makes the use of many of the more efficient matrix solving techniques risky. Thus, in this thesis a Gauss-Jordan method was chosen, combined with backward substitution. For the details on this method we refer to standard textbooks on solving matrix equations. The main advantage of this approach is that it works well for even badly conditioned matrices, although it is a fairly slow solving technique.

4.5.3 Optimisation of the MoM code

Studying the matrix equations for both TE and TM, equations 4.26 and 4.27, it can be seen that equation 4.26 is equal to the first term of equation 4.27, except for a factor 2. This also applies to the equations for the scattered field, equations 4.28 and 4.29. This means that the singularity for the TM case is equal to the logarithmic singularity for TE, except for the factor 2. It may thus be treated similarly.

Therefore, the evaluation of the scattering at TM polarisation may be performed with little extra cost during the evaluation of the scattering at TE polarisation. If only the evaluation at one of the polarisations is desired, it is more efficient to perform it solely, but when both polarisations are required, this approach reduces the CPU time by almost 50%.

4.6 Validation

In this chapter a Method of Moments solution of the electric field integral equation was presented. This solution has been especially designed for the problem of the

two dimensional scattering on perfectly conducting surfaces. In this section a number of calculations of the scattering on standard 2D objects are presented. These calculations are compared with examples from literature to validate the MoM code. In the rest of the chapter, the MoM code presented in this chapter is referred to as MoM1.

The results for the scattered fields will be presented in the form of the 2D radar cross section defined as:

$$\sigma^c = 2\pi \lim_{r\to\infty} r\frac{E^s \cdot E^{s*}}{E^i \cdot E^{i*}}. \tag{4.37}$$

4.6.1 Flat plates

Here the results for a calculation on flat plates are presented. Flat plates are complicated, due to their edges. Edge effects prevent a theoretical solution. Therefore, we have opted to compare our method to two other approximate methods, [82, 124].

In figure 4.3 the current obtained with MoM1 for a flat plate with a width of 1λ is compared with results of a similar analysis from [124]. The latter analysis was a 3D calculation, performed with another MoM code of the scattering on a flat strip, with a size of $40\lambda \times 1\lambda$. The presented currents are taken directly from the middle of the long edge of the plate, i.e. at 20λ. The upper two panels give the results of MoM1 for TE (left) and TM (right), while the lower two panels give their counterparts from [124]. Comparing the results from both methods reveals that they match very well. Some slight deviations can be explained by the fact that the results from [123] were obtained by a 3D analysis, while the results from MoM1 are truly 2D.

In figure 4.3 a comparison is made between the cross section results obtained by MoM1 and those by [82]. The results in [82] were obtained with a novel method. They first derived the results for an infinitely long ellipsoid cylinder. Then they let the short axis of the ellipse go to zero. This results in an infinitely long strip with a width of two times the long axis (a) of the ellipse. The upper two panels give the results of MoM1 for two values of a: $a = 5.29/k$ and $a = 8.94/k$. The lower two panels give their counterparts from [82]. Here the solid line represents TE or $\parallel$ polarisation and the dotted line TM or $\perp$ polarisation. Comparing the results from both methods show a good agreement. The only real deviation can be found in the second sidelobe of the TE or $\parallel$ polarisation for $a = 5.29/k$.

4.6.2 Cylinders

Here the results of calculations on cylinders are shown. The scattering problem is defined as follows: The main axis of the cylinder lies along the z-axis. The radius of the cylinder is denoted by a. Four cylinders are evaluated. Their radii are defined by

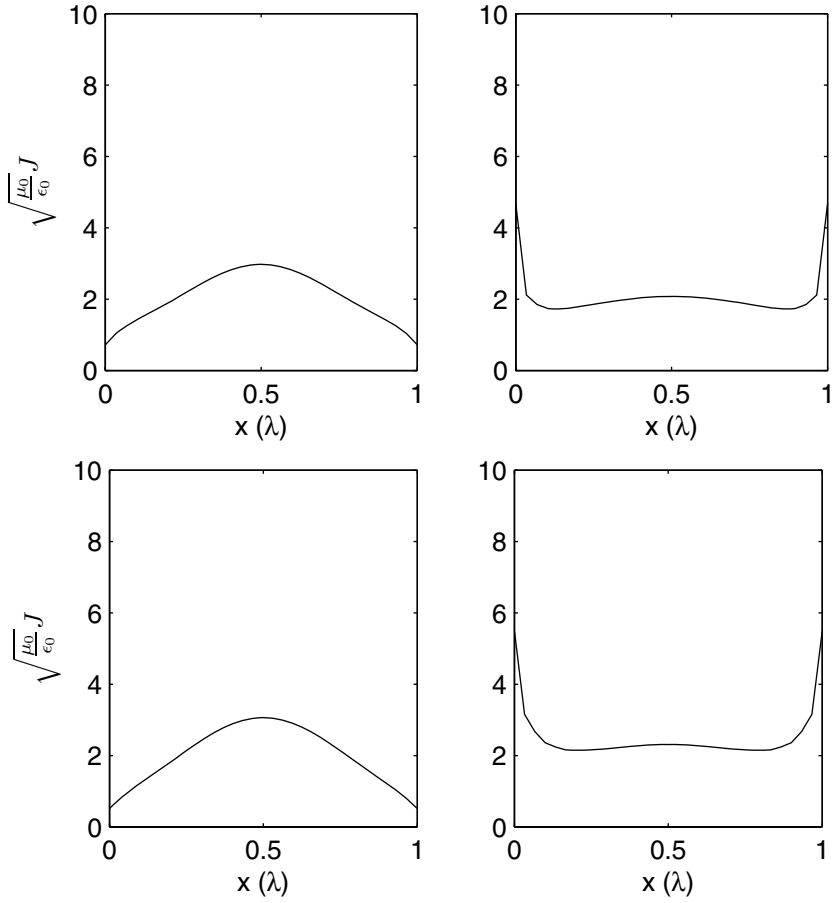

Figure 4.3: Validation calculation for flat plates: The surface current. The upper two panels give the results of MoM1, while the lower two panels give the results from [124]. The currents are normalised by a factor $\sqrt{\mu_0/\epsilon_0}$.

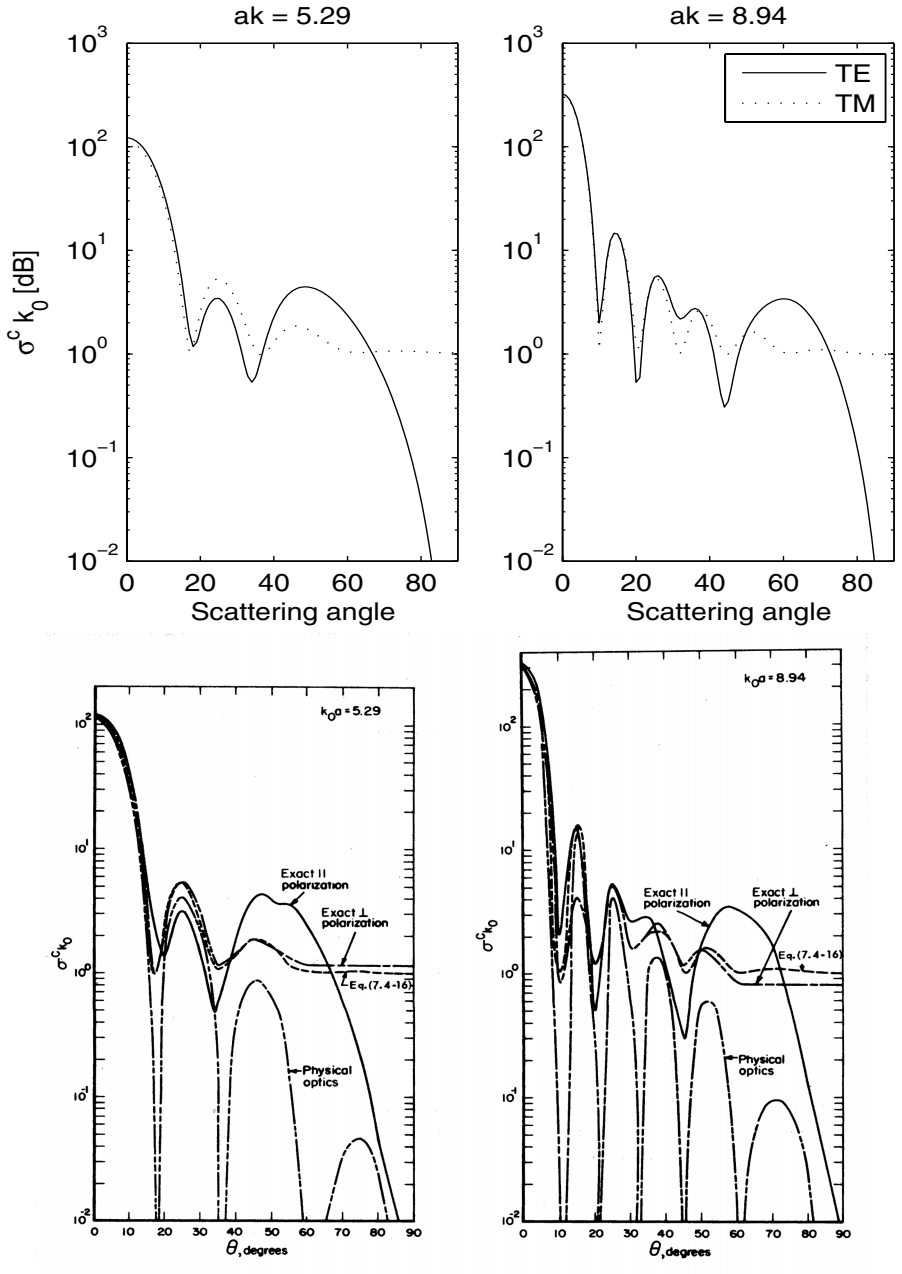

Figure 4.4: Validation calculation for flat plates: Cross section. The upper two panels show the results of MoM1, while the lower two present those of [82]. The cross section are normalised by a factor k_0.

$ak = 0.5, 1, 5$ and 10, with $k = \frac{2\pi}{\lambda}$ the wavenumber of the scattered radiation. The results of the calculations are shown in figures 4.5, for TE polarisation and 4.6 for TM polarisation. The upper four panels show the normalised 2D RCS, $\sigma^c/(\pi a)$ of the cylinders. Results are shown of both the MoM code (solid line) and theoretical (dotted line) 2D cross section. The cross sections are all given in dB. The theoretical results were obtained from [81], chapter 3. It is easily observed that the results of the MoM code match the theoretical results very well. To better illustrate this fact, the difference between the two results for the cylinders with $ak = 0.5$ and 10 are presented in the lower two panels of each figure. These results are also in db scale. Studying these results it can be stated that the MoM results match the theoretical results within 0.3 dB.

4.7 Summary and conclusions

In this chapter a Method of Moments code was presented that was designed for the evaluation of breaking wave profiles. Therefore, the method was adapted for randomly shaped 2D objects, made out of a perfectly conducting material. Firstly, the electric field integral equation (EFIE) for this problem was derived. The Method of Moments was then used to rewrite this problem in the form of a matrix equation. Here pulse functions were used for the expansion of the current and point matching was used in the testing procedure. Subsequently, some implementation issues were treated. Particular attention was given to resolving the singularities that occur on the diagonal of the matrix. Finally, the method was validated against literature results, for two types of standard objects. This validation showed good agreement of the MoM code's results with the literature. From this it can be concluded that the method presented in this chapter, is very suitable for evaluating the complicated objects it was designed for.

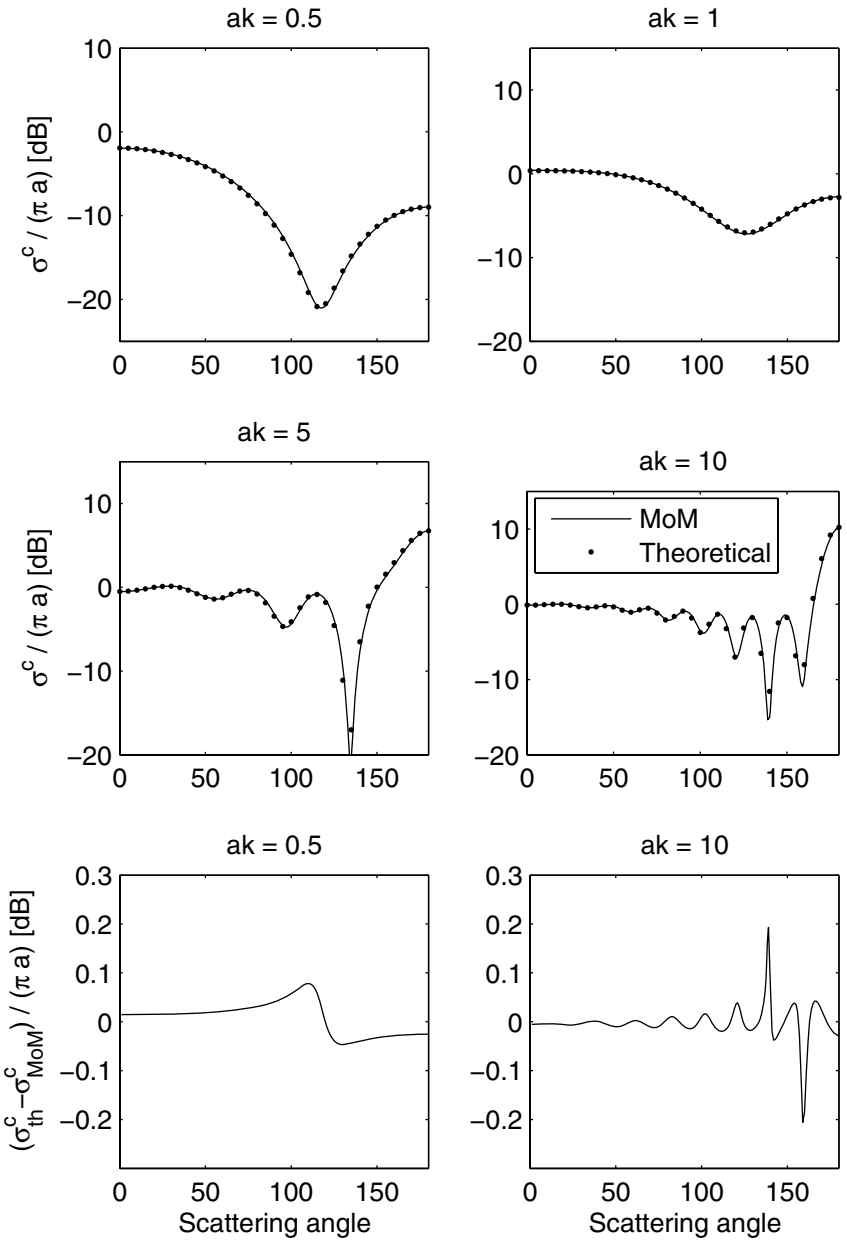

Figure 4.5: Validation calculation for cylinders, TE polarisation. The upper four panels show results for four cylinders of different radii and the lower two panels show the difference between the MoM1 results and those of the exact results of [81]. The cross sections are normalised by a factor $1/(\pi a)$.

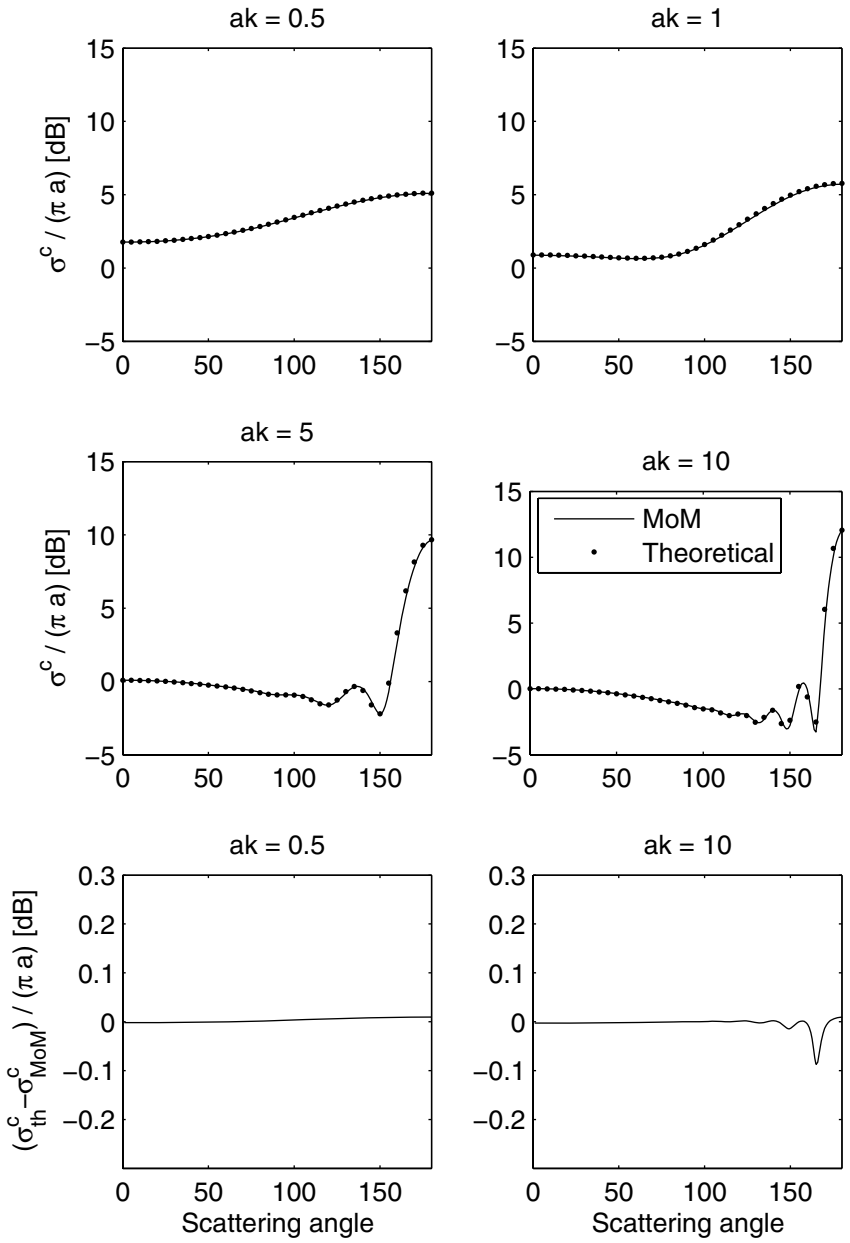

Figure 4.6: Validation calculation for cylinders, TM polarisation. The upper four panels show results for four cylinders of different radii and the lower two panels show the difference between the MoM1 results and those of the exact results of [81]. The cross sections are normalised by a factor $1/(\pi a)$.

Chapter 5

The combined radar seaclutter model

5.1 Introduction

The main goal of this thesis, as stated in chapter 1, is to build a comprehensive model of ocean surface radar scattering. Such a model must have two characteristics. Firstly, and most importantly, it should incorporate models of most of the physical processes making up sea clutter. Secondly, the model has to improve on current models. In this chapter a radar seaclutter model is presented that satisfies both these requirements. To the authors knowledge, there are very few, if any, models that incorporate most of the physical processes, that generate sea clutter. This means that satisfying the first requirement, automatically satisfies the second. The basic assumption of our model is that sea clutter is made up out of two main components, tilt-modulated Bragg scattering (composite surface) and sea spikes (scattering on steepened or breaking waves). By combining current knowledge on oceanography and electromagnetism, see chapters 2 to 4, both components are modelled. Moreover, a wave breaking criterion is presented, which allows the fusion of the two components:

The model is schematically shown in figure 5.1. The model is roughly divided into two main parts, an oceanographic component (surface generation) and an electromagnetic one (RCS calculation). The former generates a realisation of the ocean surface, while the latter is used to evaluate this surface and calculate its radar cross section. The surface generation consists of two components,

1. Spectral surface generation, where an equilibrium ocean surface is generated through spectral analysis.

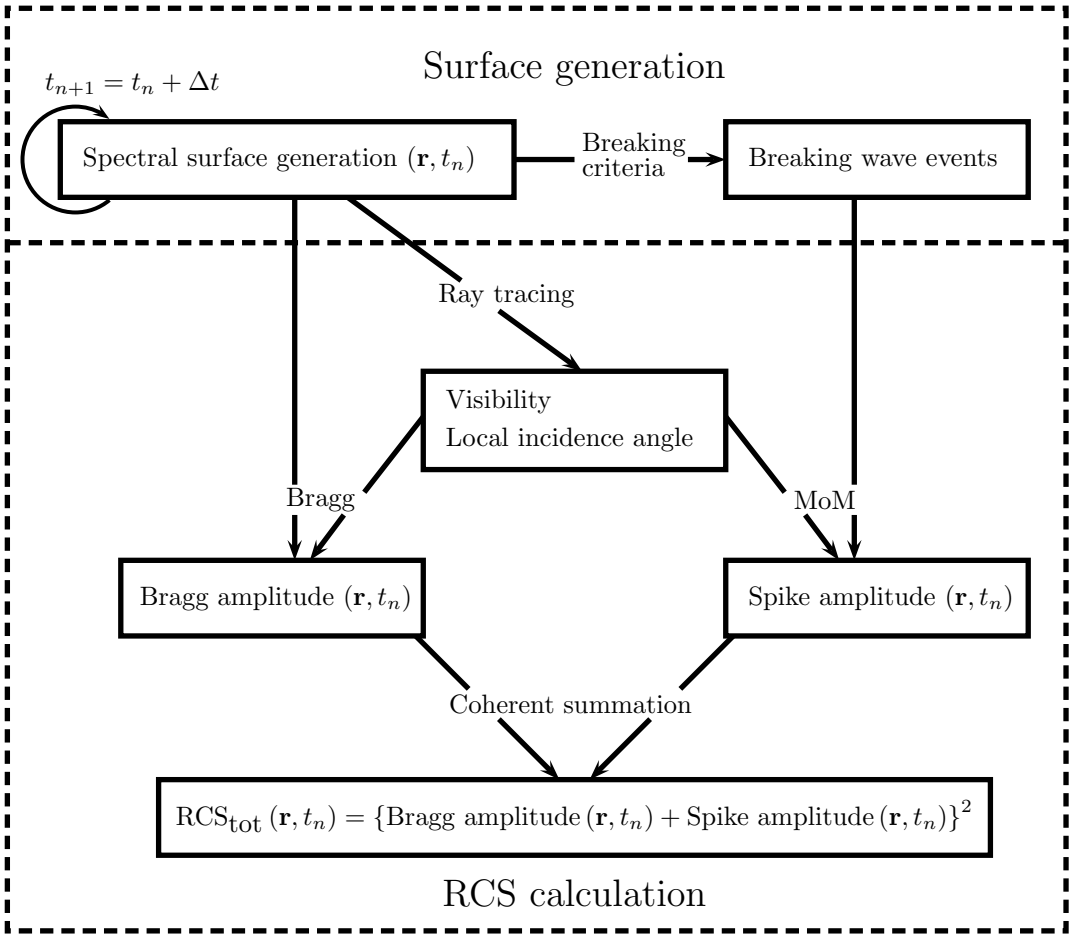

Figure 5.1: Schematic of the sea clutter modelling approach. It consist of six main components, indicated by the arrows, which are models of physical processes. Each of these processes generates one or more physical quantities, which have been put in the boxes.

2. Breaking wave generation, where a breaking criterion is used to predict the occurrence of breaking waves on different parts of the generated surface.

These two components together generate ocean surface realisations. These realisations are then evaluated in the second part of the model to calculate the corresponding RCS. This part of the model is made up of an additional four components,

3. Ray-tracing, where the illumination of and local incidence angle on the surface are determined.
4. Bragg RCS calculation, where the results of the ray tracing routine are used in combination with Bragg theory to calculate the composite surface RCS for the surface. Here the velocity of the Bragg component is calculated by adding the intrinsic velocity of the Bragg waves to the orbital velocity of the swell.
5. Spike RCS calculation, where the MoM code from chapter 4 is used to evaluate the breaking wave profiles, which are generated in the breaking wave component. The velocity of the breakers is determined by calculating their phase velocity.
6. Combined RCS calculation. As is shown later in this chapter, during items 4 and 5 the phase information of both the Bragg and the spike components are also determined. From this complex amplitudes of both components can be calculated. These amplitudes are then used to determine the combined RCS and velocity.

The model presented in this chapter is one-dimensional, i.e. all properties vary along one dimension. There are a number of reasons for this. Firstly, because the physics of breaking waves is extremely complicated, the hydrodynamic simulation of these objects, the LONGTANK profiles presented in chapter 2, was performed on a 1D grid. Secondly, the complicated nature of these profiles requires a full-wave electromagnetic method such as the method of moments, to evaluate. Extending both the profiles and the MoM code to two dimensions was deemed to be too complicated and therefore outside the scope of this thesis. Moreover, evaluating 2D breaking wave profiles with a MoM code would require a prohibitive amount of computer calculations. Finally, navigational radar operate according to a 1D principle. Such systems transmit radiation in one dimension and measure the scattered power along that direction. A 2D image of the surroundings is built up by rotating the radar, while continuously receiving echoes from the surroundings after each transmission. Therefore, the 1D model presented in this chapter is capable of simulating these types of measurement.

This chapter is organized in the following manner. The six components of the model are treated in the consecutive sections 5.2 to 5.7. Section 5.8 discusses the results and draws preliminary conclusions about the model. In the next chapter the

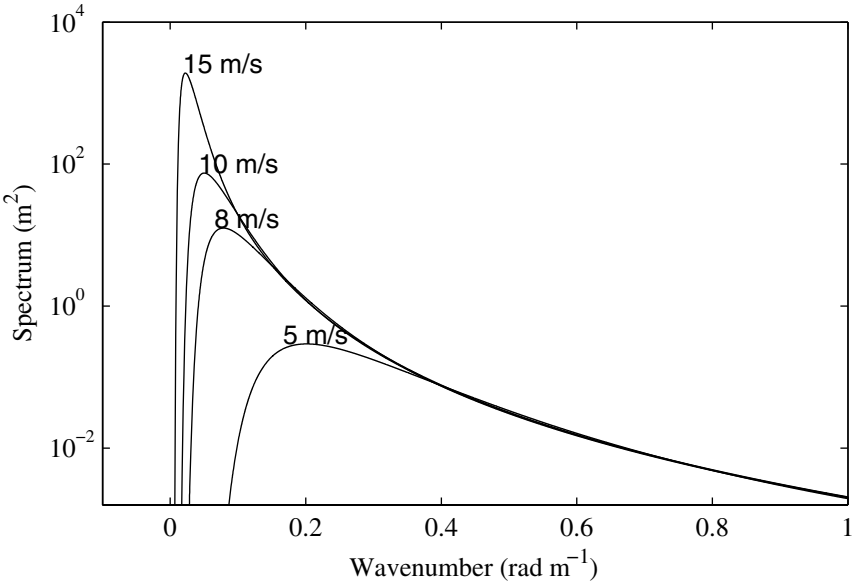

Figure 5.2: Examples of the spectrum used in this chapter for four different values of the wind speed W_{10}, $5, 8, 10$ and 15 ms^{-1}. This spectrum is built up out of a PM low-frequency roll-off in combination with a RAW high-frequency roll-off.

results of the analysis of three sets of radar sea clutter are presented. In chapter 7 the model results are compared to those of the data, which allows conclusions to be drawn about the validity of the model .

5.2 Spectral surface generation

The spectral surface generation uses standard spectral theory to generate ocean surface realisations. It consists of two parts, a spatial Fourier transform to generate the surface and a phase evolution to evolve this surface.

Start with a 1D spectrum, Ψ, as defined in section 2.3,

$$\Psi(k) = A\frac{F_l J_p F_h}{k^4}, \tag{5.1}$$

where k is the wavenumber of the water waves, A is a constant, which by [3] was determined to be 0.00195, F_l the low-frequency roll-off, F_h the high-frequency roll-off and J_p the peak enhancement factor. For both the high and the low frequency

roll-off a number of formulations exist. In this thesis we have adopted the Pierson-Moskowitz (PM) form for the low-frequency roll-off (eq. 2.44) in combination with a Romeiser-Alpers-Wisman (RAW) for the high-frequency roll-off (eq 2.54). The features of these roll-offs are discussed in section 2.3.2. The spectrum will be referred to as PMRAW in the rest of this chapter. An example of such a spectrum is shown in figure 5.2.

To generate an ocean surface realisation from such a spectrum three steps need to be taken:

- The above defined spectrum is a power spectrum. It needs to be transformed into an amplitude spectrum, which is accomplished by taking the square root.
- As explained in section 2.3, the phase information of the ocean surface is lost by representing it by a parameterised spectrum. To obtain a true surface realisation, phase information needs to be put into the spectrum. On a typical ocean surface most waves move independent from each other. This means that due to their different phase velocities their phases are typically random. Consequently, the model is initialised with random phase factors. The phase information will later be used to evolve the surface.

Combining these two steps gives the following form of the amplitude spectrum at the initial time t_0:

$$\Psi_a(k, \phi, t_0) = \sqrt{\Psi(k)} e^{2\pi j \phi(k) t_0}, \phi(k) = \text{random}. \tag{5.2}$$

- The spatial analysis is concluded by applying an inverse Fourier transform to the spectrum to obtain an ocean surface realisation $z(x, t_0)$:

$$z(x, t_0) = \text{IFT}\left(\Psi_a(k, \phi, t_0)\right) = \text{IFT}\left(\sqrt{\Psi(k)} e^{2\pi j \phi(k) t_0}\right), \tag{5.3}$$

where x is the range coordinate.

This same approach can be used for generating 2D surfaces, but as mentioned in the introduction the model is restricted to 1D spectra and surfaces. An example of an ocean surface realisation generated using the methodology described in this section is shown in figure 5.3. Such a surface forms the basis for the rest of the model, which is presented in the following sections.

Now that a single surface realisation has been generated at some time $t = t_0$, a time-series of the surface is generated by evolving the surface. Incidentally, this is marked by the curved arrow at the surface generation box in figure 5.1. The procedure is as follows. Firstly, the phase speed $v_{\text{ph}}(k) = \frac{\omega(k)}{k}$ is determined for each of the component waves of the spectrum. Then the phase of each component wave is evolved using this phase speed. Finally, a new realisation is determined

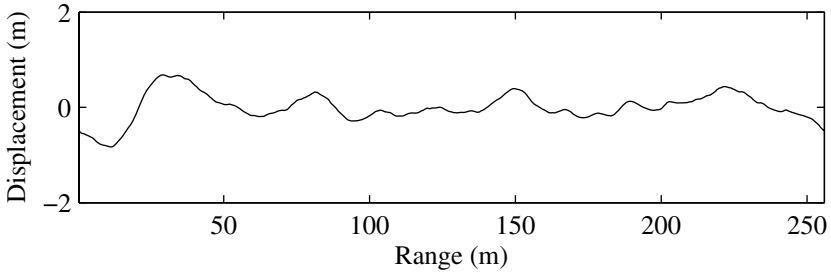

Figure 5.3: Example of an ocean surface realisation. This realisation was generated using the procedure of section 5.2. The propagation direction of the waves is towards infinity, i.e. the right of the figure.

by applying an inverse Fourier transform to the surface. This procedure may be repeated indefinitely to generate a time series of the surface of any desired length. The procedure is summarised in equation 5.4.

$$z(x, t_0 + \mathrm{d}t) = \mathrm{IFT}\left(\Psi_a(k, \phi, t_0 + \mathrm{d}t)\right) = \mathrm{IFT}\left(\sqrt{\Psi(k)}e^{2\pi j(\phi(k)t_0 + v_{\mathrm{ph}}\mathrm{d}t)}\right) \quad (5.4)$$

Note that the propagation direction of the waves is towards infinity, i.e. the right side of figure 5.3. The spectral surface generation is the engine that drives the entire seaclutter model. Each realisation, i.e. timestep, is analysed and finally leads to a radar seaclutter simulation. This results in a series of radar rangelines similar to the data results from the next chapter.

5.3 Breaking wave generation

The breaking wave generation component again consists of two parts, (i) determining where and when a breaking wave may occur and (ii) grafting the breaking wave into the realisations generated by spectral analysis. These two parts are discussed in subsections 5.3.1 and 5.3.2.

5.3.1 Breaking wave localisation

The aim of this subsection is to determine when and where a breaking wave event may occur and what its wavelength will be. The first step towards obtaining this goal is to find which physical parameters govern wave breaking.

Table 5.1: Values of the steepness parameter

$\{ak\}_{\text{crit}}$ value	reference
1.07	[92]
0.84	[53]
0.79	[12]
0.36	[8]

The main problem is that it is not yet fully understood how deep water wave breaking occurs. What is known is that a wave will break if it is sufficiently steep, which was first shown by [92]. This means that the steepness of a wave is a good indicator of wave breaking. Therefore, the steepness parameter, ak, the amplitude of a wave multiplied by its wavenumber, is the central parameter in our wave breaking criterion. To obtain a good criterion, two questions must be answered:

1. At what steepness does wave breaking occur? In particular, is there a critical value $\{ak\}_{\text{crit}}$ for the steepness parameter beyond which breaking is triggered?

2. What processes lead to sufficiently high steepness values and when and where do these high values occur?

These are the central questions that we attempt to answer in this section. This will lead to a wave breaking criterion, which indicates where breaking waves are located on the surface, what their wavelengths are and at what time these events occur.

The answer to the first question can be found in literature. Many values of $\{ak\}_{\text{crit}}$ have been proposed, based on a number of different physical considerations. These values are summarised in table 5.1. The first column gives the critical value of the parameter ak beyond which the authors suggest that wave breaking occurs and the second column gives the reference to the papers from which these values were obtained. In this thesis the value proposed by [8], 0.36, is used. This value is one of the most recently suggested and as such uses the most current insights in this topic. Moreover, it has been compared to some of the other suggestions in [7] and was found to best predict wave breaking.

The second question is more difficult to answer. It is not completely understood what triggers the high values of ak in deep water. In coastal regions decrease of the depth of the water results in the steepening and, ultimately, breaking of waves. In recent years it has been frequently suggested that in deep water group processes cause the high values of ak that are needed for wave breaking, see for instance [17, 112]. When a wave moves through a wavegroup, interactions with the other waves in the group may cause it to steepen. As is shown later in this section, wave-wave interactions are used in our breaking criterion.

There are two ways of calculating ak, either directly by multiplying the ampli-

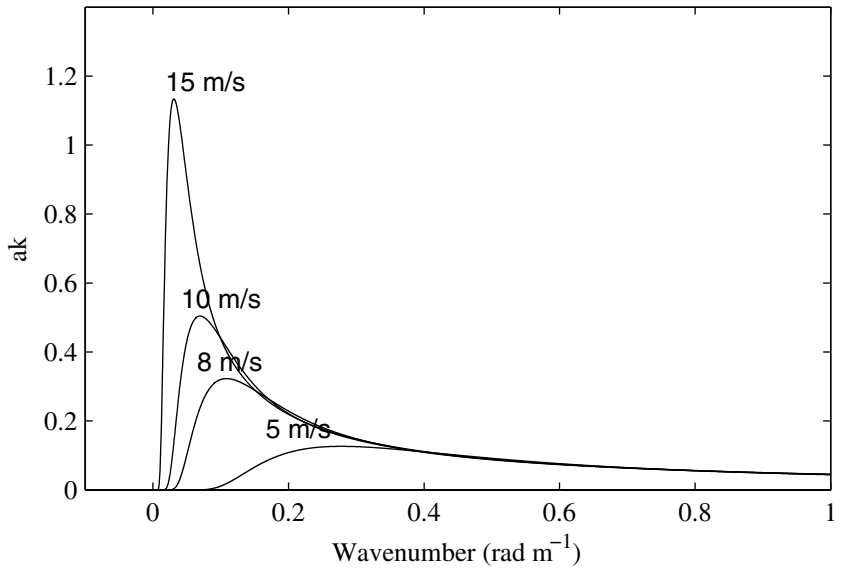

Figure 5.4: The dependence of ak with respect to k for different values of the input wind speed, W_{10}. The different curves were calculated using a PMRAW spectrum, with input wind speeds of 5, 8, 10, 12.5 and 15 ms^{-1}. Here the curve with the lowest maximum is the one for $W_{10} = 5$ ms^{-1}, while the highest curve is for $W_{10} = 15$ ms^{-1}.

tude of a wave a with its wavenumber k or indirectly by dividing its orbital velocity by the phase velocity. The direct method has the advantage of simplicity and for higher wind speeds produces breaking wave candidates as illustrated in figure 5.4. In this figure the value of ak is plotted versus k for different values of the input wind speed, W_{10}. These values were obtained by taking the amplitude spectrum, i.e. de square root of the power spectrum, and multiplying it by k. However, it does not indicate where and when a given critical wave, i.e. a wave with a critical ak value, might actually break. Nor does it tell what the wavelength of the breaker would be. Furthermore, as can be seen from figure 5.4, it only produces viable values of ak for higher values of W_{10}, i.e. $W_{10} \geq 10$ ms^{-1}. Breaking waves do, however, also occur at lower wind speeds. For these reasons this approach has been discarded in favour of the second criterion.

This second criterion is based on the ratio of the orbital velocity to the phase velocity. Let us consider a single wave with wavenumber k_0. For this wave the orbital velocity, v_o, and the phase velocity, v_{ph}, are defined as:

$$v_o(x, t, k_0) \quad = \quad \omega y = \omega a(k_0) \cos(k_0 x - \omega t), \tag{5.5}$$

$$v_{ph}(k_0) = \frac{\omega}{k_0}. \tag{5.6}$$

From these definitions it can easily be derived that dividing v_o by v_{ph} gives a measure for ak:

$$\begin{aligned} \frac{v_o}{v_{ph}} &= \frac{\omega a(k_0)\cos(k_0 x - \omega t)}{\frac{\omega}{k_0}} \\ &= a(k_0)k_0\cos(k_0 x - \omega t) \qquad (5.7) \\ \frac{v_{o,\max}}{v_{ph}} &= \frac{\omega a(k)}{\frac{\omega}{k}} = a(k_0)k_0 \qquad (5.8) \end{aligned}$$

Therefore, equation 5.8 shows that the maximum value of the orbital velocity divided by the phase velocity is equal to the factor ak. More interestingly, equation 5.8 shows that the ratio of v_o and v_{ph} is dependent on both range and time. In particular, ak exhibits extreme values at the crest and trough of the wave. This in turn allows for the identification of specific regions of possible breaking activity.

For a collection of waves the orbital velocities for the different waves should be combined so that:

$$v_{o,\text{tot}} = \sum_k v_o = \sum_k \omega a(k)\cos(kx - \omega t + \phi(k)), \tag{5.9}$$

where $\phi(k)$ is the instantaneous phase of each wave component at some reference time. Equation 5.9 gives the total orbital velocity at any part of the surface. To test whether a particular wave, with wavenumber k_0 will break through interaction with this combined orbital velocity, we divide by the phase velocity of that wave:

$$\{ak\}(k_0) = \frac{v_{o,\text{tot}}}{v_{ph}(k_0)} = \frac{\sum_k \omega a(k)\cos(kx - \omega t + \phi(k))}{\frac{\omega(k_0)}{k_0}}. \tag{5.10}$$

Moreover, by combining the orbital velocities of the different wave components, this approach also incorporates wave-wave interaction and group processes.

By summing the orbital velocities from all wave components, it is assumed that all those components influence the wave, k_0. Physically this is correct, but the interaction between waves of widely different wavenumbers is negligible. In fact, a small wave will experience the orbital velocity field of a much larger wave as a type of current. In the same manner the negligable energy of a small wave compared to a large wave insures that the influence of that small wave on the larger one is irrelevant. A wave of a given wavenumber will, therefore, mainly interact with waves of comparable wavenumbers. To compensate for this effect a filter, $w(k, k_0)$, is introduced into equation 5.9:

$$v_{o,\text{eff}}(x, t, k_0) = \sum_k w(k, k_0)v_o(k, x) = \sum_k \omega a(k)w(k, k_0)\cos(kx - \omega t + \phi(k)). \tag{5.11}$$

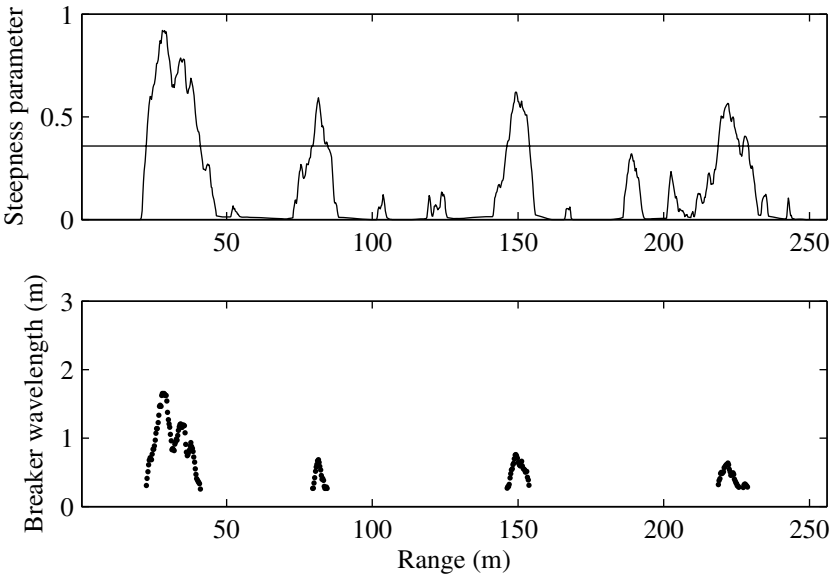

Figure 5.5: Results of the breaking wave localisation. The upper panel shows the maximum values of the steepness parameter ak as a function of range x. The horizontal line marks the critical value of ak above which breaking may occur. The lower panel shows the wavelengths of the breaking wave candidates, i.e. the wavelengths of the waves that exceed the threshold.

To obtain the desired results the weighing function is chosen to be a finite bandwidth filter. In this thesis the following form was chosen:

$$w(k, k_0) = min\left(1, 2\exp\left(-\frac{(k-k_0)^2}{\sigma_k * N}\right)\right), \tag{5.12}$$

with σ_k the filter width and N the number of k-values.

The width of the filter will be discussed in chapter 7. In that chapter the results of the model presented in the current chapter are compared to the data results of chapter 6. This is used in finding the optimum values for some of the input variables of the model. Whatever the precise shape of $w(k, k_0)$, this procedure gives the effective orbital velocity caused by a set of waves in a spectral band around the central wavenumber. By repeating the process for all values of k_0, the effective orbital velocity as a function of k_0 is obtained. This orbital velocity is then in turn divided by the phase velocity of the corresponding central wavenumber, k_0, resulting in a measure of the quantity $\{ak\}(k_0)$.

As an example, this procedure is applied to the surface from figure 5.3. The

value of σ_k in the filter, $w(k, k_0)$, was set to $N/4$. The result is shown in the upper panel of figure 5.5. In this panel the maximum positive values of ak for each position x on the surface are plotted. Only positive values are considered because a negative value of ak means that the cumulative orbital velocity is negative to the phase velocity of the central wave. Wave-current interaction theory, see [105], predicts that in those conditions a wave would lose energy to the underlying current field, which has a decaying effect on the wave. Setting a certain threshold value for ak then gives the smallest k, i.e. the largest wave for which a breaking event might occur. For this simulation the threshold value of $ak = 0.36$ was chosen. It is denoted by a horizontal line in the figure. The result of the selection procedure for the example realisation is shown in the lower panel of figure 5.5. In this figure the wavelengths of the largest waves that exceed the threshold value are plotted.

5.3.2 Tracking the breaking waves on the surface

Having determined where a breaking wave of a given wavenumber may occur, the generation of breaking wave events is straightforward. As explained in the previous section, one of the outputs of the surface generation procedure is the breaker candidates as a function of range and time. At the first time stamp a number of the candidates at that time is chosen at random and from these events are generated. The wavelength of the candidate gives the lifetime of the event as is explained in section 5.6.3. The event is then generated on the underlying surface by marking the region in range and time where the breaking occurs. The movement in range of the breaker over time is calculated from its phase velocity. In this thesis the size of a breaker is assumed to be its wavelength, with as minimum size one rangebin.

It is assumed that in the direct neighbourhood of the event no additional events occur. Thus, a radius is defined dependent on the size, i.e. wavelength, of the breaking wave. Within this radius no other breaking wave events can occur, effectively blocking the other candidates within this region. The total area that is blocked in set to 1.5 wavelengths. After the breaker has ‘died the area is extended for an additional time of 20 ms. After that time new events can be generated again.

All the next timesteps follow the same procedure. Starting from the largest event on the rangeline, events are generated until all candidates are either blocked by another event or have given rise to an event. The procedure of generating the breakers is the same as followed for the first time step. The final result of this procedure is a list of breaking wave events, each with a specific wavelength, location and lifetime. In section 5.6 it is shown how the RCS is determined for each of these events, which results in true spiking events superimposed on the Bragg background.

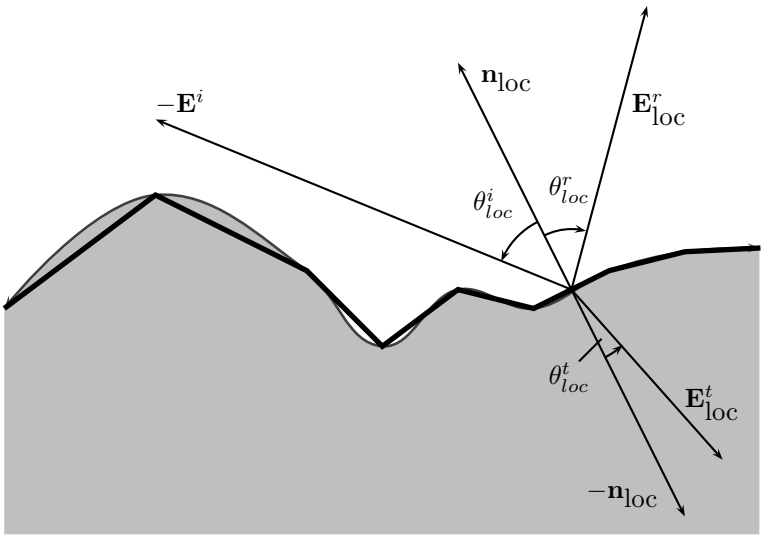

Figure 5.6: Backward ray tracing: The surface is divided into patches. From the center of each patch a ray is 'shot' in the direction of the incident radiation. This gives the local incidence angle, θ^i_{loc}, i.e. the angle between the ray and the local normal. Using Snell's law the local reflection angle, θ^r_{loc}, and local transmission angle, θ^t_{loc}, can be determined.

5.4 Backward ray tracing

An important part of the model consist of the global evaluation of the surface. This has the goal of determining (1) which part of the surface is illuminated, and (2) what the local incidence angle on each part of the surface is. Full-wave methods incorporate these two properties, but Bragg scattering does not. Full-wave methods are not suited for evaluating the whole surface and, therefore, another method is needed. In this thesis the evaluation is performed by a ray-tracing scheme. The advantage of this method is that it requires much less computing power and as such is much faster than full-wave methods. As explained in chapter 3, however, this method has certain limitations. In particular, the surface under consideration needs to be relatively smooth, which is the case for the ocean surface realisation.

To perform the ray tracing part of this model a backward ray tracing scheme was chosen. Ray tracing is a technique whereby the scattering object is described as a collection of flat patches. For each patch Snell's laws are used to determine whether the patch is illuminated and if so, what the local incidence angle of the scattering radiation is on the patch. In this section we restrict ourselves to the monostatic, single reflection case. Monostatic means that the observation direction or point

is equal to the illumination direction or point. As described in the introduction of this chapter, this is one of the basic restrictions that has been imposed on this model. Single reflection means that no multiple, internal, reflections are taken into account. For the purpose of this thesis this is a safe restriction to make. The only objects that do cause multiple reflections are the breaking waves. These objects, however, are evaluated separately, using a MoM code. That code incorporates multiple scatterings. The main purpose of the ray tracing routine is thus satisfied by single and monostatic scattering.

The basic approach is sketched in figure 5.6. The surface is first divided into a number of patches, line segments in the two-dimensional case treated here. For these patches the midpoints, $(x_{\text{mid}}, y_{\text{mid}})$, and normals, $\mathbf{n}$, are determined. The ray is 'shot' from the midpoint either to the observation point or in the observation direction. The angle between this ray and the local normal gives the local incidence angle of the radiation. Applying Snell's law gives us the reflection and, if desired, transmission angles of the radiation. These two angles are important for multiple reflection and bistatic scattering.

The next step is the determination of shadowing for both the incident and reflected radiation. The following scheme for doing this was chosen here:

1. Determine the line equation of the ray.
2. Calculate the y-values of the ray corresponding to the x-values of the midpoints of the other surface patches.
3. If the y-values of the ray lie below one of the corresponding y-values of the midpoints, the ray is blocked by that patch.
4. If no blocking occurs, the ray is accepted and the patch is considered to be illuminated. Otherwise, the patch is considered to be shadowed.

The main advantage of the backward ray tracing scheme is that it is a fairly efficient way of evaluating large surfaces. Only one ray per surface patch is needed to determine the illumination of and local incidence angle on the patch. Some errors do occur, mainly in the algorithm to detect shadowing. Firstly, the blocking of a patch by another patch is only checked at the midpoint of the blocking patch. Any blocking by the edges of that patch are ignored. Secondly, partial shadowing of a patch is also ignored. A patch is considered to be illuminated or shadowed if its midpoint is. Both these effects may lead to slight errors on the edge of a shadowed region. The influence of these effects might be mitigated by a number of schemes, for instance by sampling on a finer grid. Moreover, the partly shadowed patches that are assumed to be unshadowed, should be as numerous as the partly shadowed patches that are assumed to be shadowed. Therefore, for a sufficient number of patches the above described errors should cancel out.

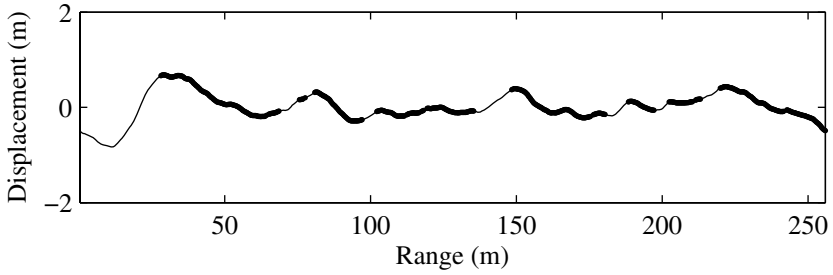

Figure 5.7: Results of the backward ray tracing algorithm. The heavier black patches denote the illuminated parts of the surface. The surface evaluated is the same as presented in figure 5.3.

The results of the ray tracing algorithm for the surface under consideration is shown in figure 5.7. In this figure the ocean surface realisation from figure 5.3 is shown. The global incidence angle of the radiation was set to be 98°. This means that radiation is assumed to be transmitted from a source that is looking upwave, i.e. in the opposite direction from the propagation direction of the surface waves. On the surface those parts that are illuminated are denoted by the heavier black patches and the thinner sections are non-illuminated. In the rest of the model, no scattering from those parts of the surface is allowed. Only a slight 'dark current' level is assumed for the shadowed regions. This is explained in more detail in the next section.

5.5 Tilt-modulated Bragg RCS

Bragg scattering was treated in section 3.2.3. The RCS (σ_0) of a Bragg patch is given by:

$$\sigma_0 = 16\pi k^4 \left|g_{pp}\left(\theta\right)\right|^2 \Psi\left(0, k_B\right), \tag{5.13}$$

where pp indicates either HH, HV, VH or VV, k_B is the Bragg wavenumber, which follows from the Bragg criterion,

$$k_B = 2k\sin\theta, \tag{5.14}$$

and

$$g_{\mathrm{HH}}\left(\theta\right) = \frac{\left(\epsilon_r - 1\right)\cos^2\theta}{\left(\cos\theta + \sqrt{\epsilon_r - \sin^2\theta}\right)^2}, \tag{5.15}$$

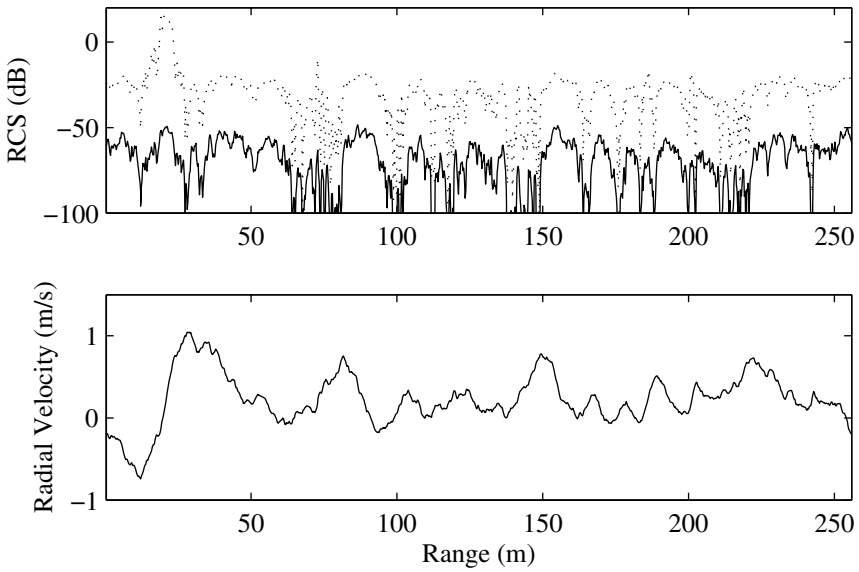

Figure 5.8: Bragg RCS calculation results for the surface from figure 5.3. The upper panel shows the Bragg RCS for HH (solid line) and VV (dotted line) polarisations. The lower panel shows the corresponding radial Doppler velocity of the Bragg scattered radiation.

$$g_{\mathrm{VV}}(\theta) = \frac{(\epsilon_r - 1)\left[\epsilon_r\left(1+\sin^2\theta\right) - \sin^2\theta\right]\cos^2\theta}{\left(\cos\theta + \sqrt{\epsilon_r - \sin^2\theta}\right)^2}, \tag{5.16}$$

$$g_{\mathrm{HV}} = g_{\mathrm{VH}} = 0. \tag{5.17}$$

$$\tag{5.18}$$

Given these formulae and the results of the last sections, the tilt-modulated Bragg RCS calculation is straightforward. In section 5.2 the surface was generated and divided into patches. For each patch these equations can be used to determine the RCS of that patch. The input parameters can be obtained from the results of the previous sections. The spectrum Ψ is the same spectrum as used to generate the surface and the local incidence angle θ from the backward ray tracing. Substituting these parameters in the equation presented above then gives the normalised radar cross section, σ_0, of the patch.

To obtain the true radar cross section of the patch, the normalised cross section is multiplied by the area of the resolution cell. This area can either be set to some standard value, i.e. 1×1 m or, for comparison to real data, to the size of a resolution

cell of the radar. The results of the Bragg RCS calculation for the example surface is shown in the upper panel of figure 5.8. In this panel two lines are shown. The solid line gives the HH polarization and the dotted line the VV polarization. Clearly the VV RCS exceeds the HH RCS by 20 to 30 dB.

To calculate the velocity of the Bragg component the following approach is taken. First, the total orbital velocity, i.e. the sum of the orbital velocities of all waves on the surface, is determined for each point on the surface. To this the intrinsic, i.e. phase, velocity of the Bragg scatterers is added. This results in a local Bragg velocity for each point of the surface. The results of this analysis are shown in the lower panel of figure 5.8.

5.6 Spike RCS

As discussed in chapter 1 and also in section 5.1, one of the central hypotheses of this thesis is that sea spikes are caused by the scattering on steepened and breaking waves. In section 5.3 criteria were defined that govern the formation of these types of events in our models. This resulted in a list of breaking waves with their wavelengths and locations as well as the time they come into being. This information will now be used to determine the RCS and velocity of the corresponding spiking events. This will be performed by electromagnetically evaluating breaking wave models. The first step in the evaluation is defining the precise shape and size of the breaking wave profiles that are to be evaluated. This is discussed in section 5.6.1. The next step is the actual evaluation of these profiles, which is treated in section 5.6.2. Finally, the later stages of the spikes are discussed in section 5.6.3.

5.6.1 Breaking wave profiles

Results of the LONGTANK, see [109], breaking wave simulator are presented in section 2.5. Two sets of results of this simulator are shown, one with an initial breaker wavelength of 2.3 m and another with a wavelength of 1.0 m. The main difference between these sets, except for their respective size, is the fact that the 1.0 m set was generated taking surface tension into account. Studying these different sets in detail it can be observed that their shapes do not differ very much. Only the shape of the jet deviates. In particular, the jet remains smaller for the shorter waves.

As explained in section 5.3, we wish to evaluate a continuum of waves from a wavelength of a few decimetres to a few metres. A first step in the process is to scale the profiles to the desired wavelength, say λ. Let the standard profile have a wavelength of λ_0. The scaling is then simply performed by multiplying both the x and y coordinates by a factor λ/λ_0. Now only the smaller jet for shorter waves

needs to be taken into account. In this thesis this will be done in the following manner. Starting at a wavelength of 2.0 m one profile less is taken into account for each 0.2 m shorter wavelength. Thus, at $\lambda = 2.0$ m only 17 profiles are evaluated, at $\lambda = 1.8$ m only 16, etc. In this manner the jet becomes smaller for the shorter waves. Incidentally, at $\lambda = 1.0$ m 12 profiles are evaluated, the precise number of the 1.0 m profiles and at $\lambda = 0.6$ m 10 profiles are evaluated. The jet develops from about the 11th profile and thus for the shortest waves no jetting occurs.

The next step is determining which part of the profiles should be taken into account. An analysis was performed by extending the profiles with a flat plate of different lengths. These extended profiles were then evaluated with the MoM code and it was found that the length of the extension does influence the scattered power. In fact, it can be shown from the geometry of the profiles that to take all possible multiple reflections into account the profiles would need to be extended to at least three or four wavelengths. The difference in scattered power between a partially and fully extended profile is of the order of a few dB. However, taking the ocean surface into account it is safe to assume that the profiles will be embedded in a large set of waves. These waves will block much of the possible multiple reflections. Therefore, in this thesis we have chosen to evaluate the profiles between the troughs on either side of the breaker.

As an example a set of these profiles for a 2.3 m breaking wave is shown in figure 5.9. The upper panel presents a series of consecutive phases of a breaking wave with a wavelength of 2.3 m. The lower panel shows the corresponding radial (displacement) and phase velocities of the profiles. The displacement velocity was obtained by measuring the horizontal displacement of the profiles at the crest, i.e. at the jet. The effect of the jet on the velocity is an initial increase in velocity at the beginning of the jet formation. This is caused by the mass of water that is thrown forward from the front face of the wave. In the later stages of the jet formation the velocity decreases when the jet is forced downwards. This finally causes the visible breaking and the whitecap.

5.6.2 Evaluating the breaking wave profiles with the MoM code

The MoM code used in this thesis was presented in chapter 4. The code was thoroughly tested on standard objects and showed to be in good agreement with literature. The code is used to evaluate the scattering on the breaking wave profiles that were discussed in the previous subsection. The results for six different breaker wavelengths (1.0, 1.5, 2.0, 2.5, 3.0 and 3.5 m) are shown in figure 5.10. The solid line gives the TM (HH) polarized RCS and the dotted line the TE (VV) RCS. Studying these results it can be observed that the scattering on breaking wave profiles indeed follows the results as predicted in literature. Especially for the larger breakers the RCS strongly increases, on average by 20 dB. Moreover, the HH RCS often exceeds

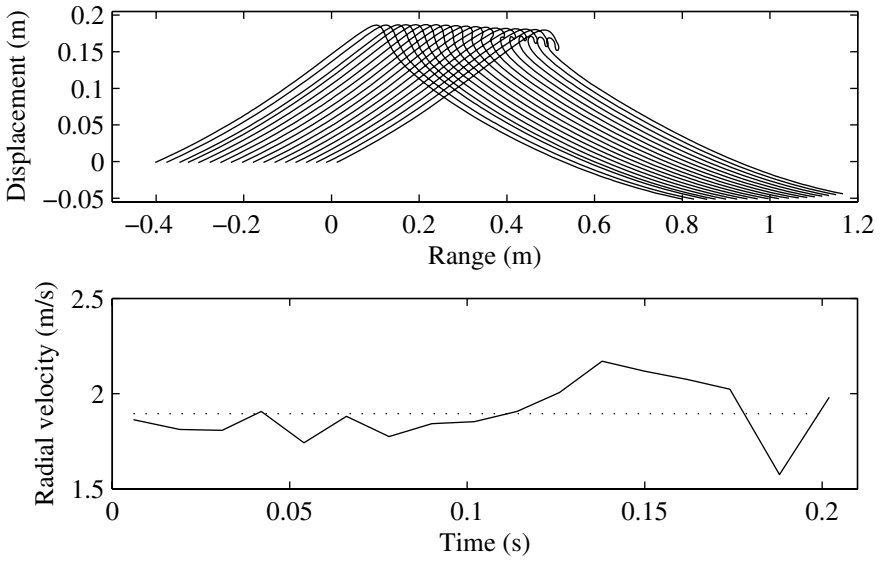

Figure 5.9: Example of the breaking wave profiles that are used for the spike RCS calculation. The upper panel shows a series of consecutive timesteps of a single breaking wave of 2.3 m wavelength. These profiles were obtained from results of the LONGTANK simulator. The lower panel shows the radial velocity (solid line) and the phase velocity (dotted line) of the profiles as a function of time.

the VV RCS. This leads to the expected high polarisation ratio. In the next section these results are combined with the results of the previous section. There it is shown that the spikes also lead to high measured velocities.

5.6.3 Spike RCS for a full event

In the previous two subsections the RCS of breaking wave profiles was determined. However, these profiles are only valid until the moment of breaking. The later stages of the spikes, i.e. the whitecap and the fading scar, cannot be modelled in this manner. In literature, little or no information is available on the scattering on these two stages. This has two reasons: firstly, no hydrodynamical models exist of whitecaps and few of the fading scar; and secondly, to the author's best knowledge, no models of scattering by foam exist. For these reasons it has been impossible to make comprehensive models of the later time stages of the spiking events. Therefore, the following approach is taken. It is assumed that during these two stages the RCS and the velocity of the events slowly decay. Due to the limited information available

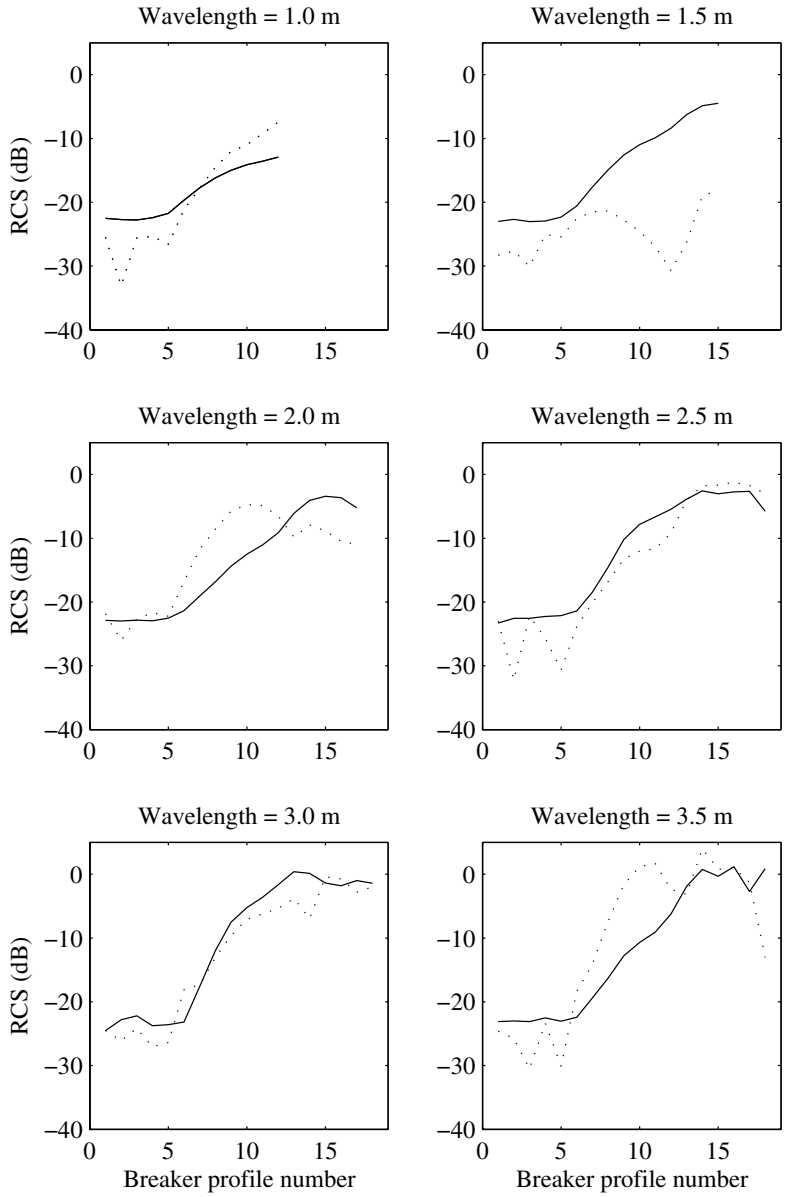

Figure 5.10: Results of the MoM evaluation of six sets of breaking wave profiles. The sets represent 1.0, 1.5, 2.0, 2.5, 3.0 and 3.5 m breaker wavelengths. The solid line gives the TM (HH) RCS and the dotted line the TE (VV) RCS.

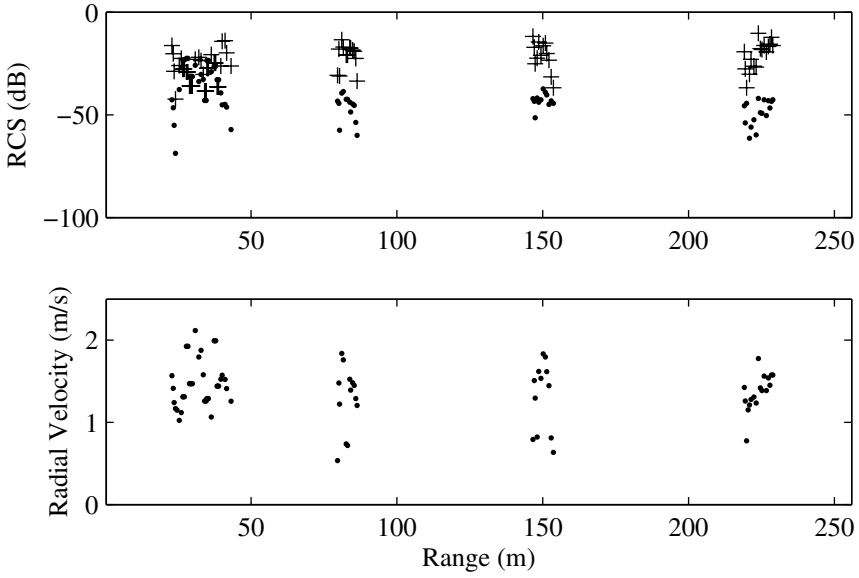

Figure 5.11: Results of the spike RCS calculation performed on the model surface. The upper panel shows the RCS of the spikes that are obtained by evaluating the breakers from figure 5.5. The dots are the TM (HH) and the crosses the TE (VV) results. The lower panel shows the velocities of the spikes.

a linear decay is used. The decay time is chosen to be approximately 4 times as long as the initial breaker onset, i.e. the timeframe spanned by the profiles. For the 2.3 m wave this translates into a total spike lifetime of approximately 1 s.

The results for the profile evaluation and the successive decay are joined to obtain the full spiking event. The total lifetime of such an event is therefore 5 times the timeframe spanned by the profiles. As a result the lifetime of a spike is directly linked to its size. This procedure was applied to the breaking waves that were determined in section 5.3. The results for the example surface are shown in figure 5.11. In the upper panel the RCS of the breakers are shown. The lower panel presents the corresponding velocities of the spikes. A more thorough analysis of the dynamics of the spikes is made in chapter 7, in particular in section 7.5

5.7 RCS combination

In the previous two sections the RCS of both the Bragg background and the spiking events was calculated. Also the measurable velocities of both of these components

were determined. In this section these two components are combined to give the final RCS and velocity of our radar seaclutter model.

The RCS combination is performed in the following manner.

- The results of the backward ray tracing routine are used to determine which parts of the surface are illuminated. For the shadowed portions of the surface the RCS is replaced by a 'dark current' with an average RCS of -100 dB.

- The complex amplitudes of both the spikes (a_s) and the Bragg (a_B) are determined by taking the square root of the corresponding RCS and multiplying it by their phase information, ϕ. As the phase of the Bragg and spikes is unknown, a random phase is added. If a full Doppler analysis would be required, this phase has to be evolved over time, given the intrinsic velocities of the different components. However, in the current model the timestep is too large (10 ms) to make this approach practical. Therefore a random phase for both the spikes and the Bragg is assumed prior to the summation.

$$a_s = \sqrt{\mathrm{RCS}_s} e^{2\pi j \phi_s} \tag{5.19}$$

$$a_B = \sqrt{\mathrm{RCS}_B} e^{2\pi j \phi_B} \tag{5.20}$$

- The amplitudes are summed and the total RCS is calculated by taking the square of the resultant amplitude.

$$\mathrm{RCS}_{\mathrm{tot}} = (|a_s + a_B|)^2 \tag{5.21}$$

- The velocity is determined by taking the weighted average of the spike (v_s) and Bragg (v_B) velocities and, if desired, a current velocity, v_c:

$$v_{\mathrm{tot}} = \frac{|a_s| \times v_s + |a_B| \times v_B}{|a_s| + |a_B|} + v_c. \tag{5.22}$$

The results of this procedure are presented in figure 5.12. The upper two panels present the RCS for HH and VV polarisations, while the lower two panels show the corresponding velocities for both polarisations. Comparing the polarisations it can be seen that the spikes are especially dominant at HH polarisation, while at VV they are not much stronger than the Bragg background. The regions with very low powers for both polarisations are the regions that are (mostly) shadowed and therefore have a RCS around -100 dB. In the velocity diagrams they stand out more clearly, even at VV. The current velocity was set to 0 m/s for this simulation. Chapter 7 will show that these results compare well with the data results from chapter 6.

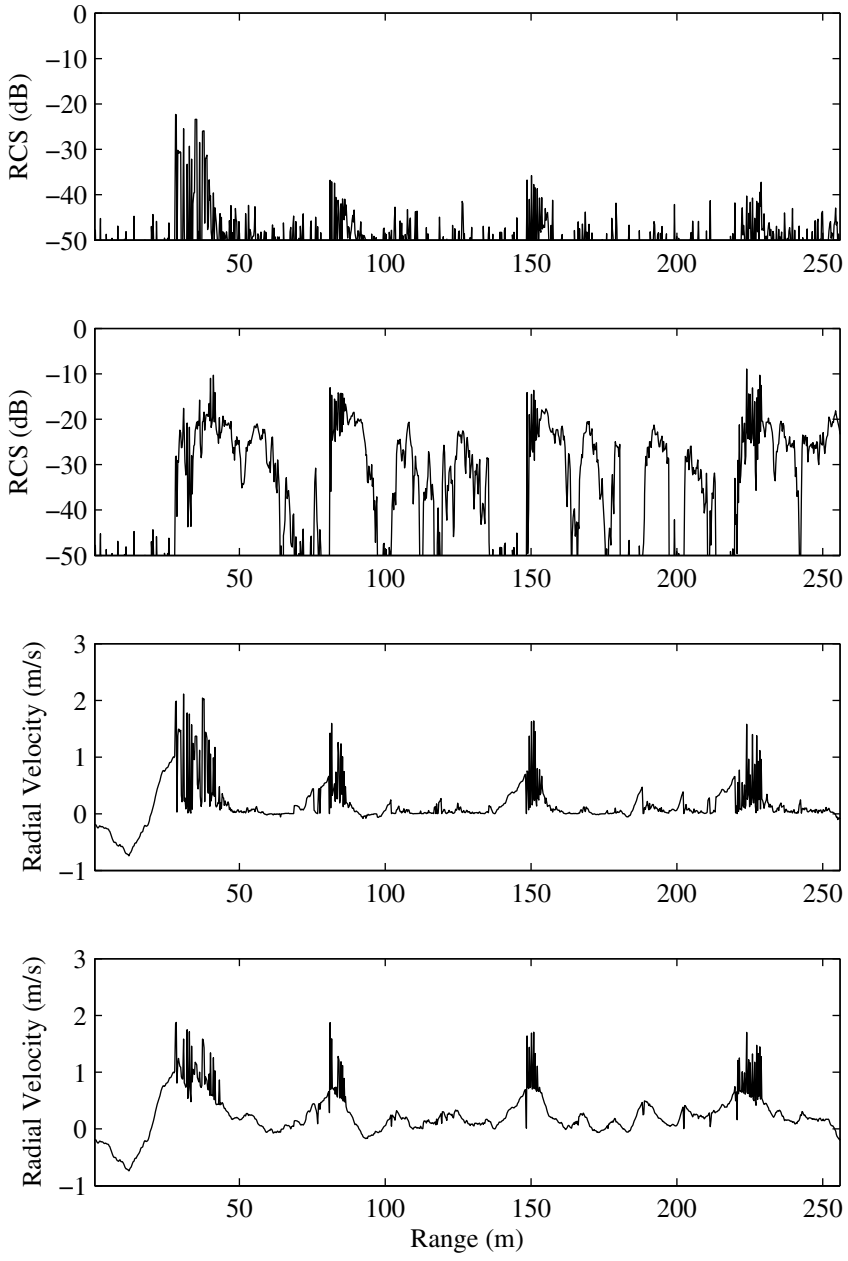

Figure 5.12: Results of the RCS combination. The upper two panels show the resultant RCS for TM (HH) and TE (VV) polarisations respectively. The lower two panels show the resultant velocities for both polarisations.

5.8 Conclusion

In this chapter a comprehensive model of low grazing angle radar seaclutter was presented. The model combines tilt-modulated Bragg scattering and sea spikes, and is also dynamic, which means that it satisfies the goals stated in chapter 1. The model will be validated in chapter 7 through a comparison with the data, analysed in the next chapter.

Chapter 6

Dynamic Behaviour of Sea Clutter*

6.1 Introduction

Over the past few decades major advances have been made on analyzing low grazing angle radar sea clutter in the GHz range, see for instance [47, 57, 112]. It was found that, in general, sea clutter consists of two parts: tilt-modulated Bragg scattering and so-called sea spikes. The Bragg scattering is associated with scattering on small cm-scale waves, which is modulated by the underlying swell. The sea spikes are distinct events characterised by a high polarisation ratio combined with a large Doppler velocity, [44, 52, 97]. In this chapter the dynamic behaviour of sea clutter is studied, and in particular that of the spikes.

Spikes have been researched in great detail, both with measurements and with models. On the measurement side, many researchers have tried to associate spiking events with events on the ocean surface and the best match was obtained with breaking waves, [25, 43, 52, 89]. It was found that spikes and breakers (whitecaps) exhibit a match of approximately 80%. Other researchers, for example [30], have studied scattering on breaking waves generated within wavetanks and found that these objects generate strong spiking events. Both approaches have made a strong case for the assumption that spikes are caused by the scattering on steepened and/or breaking waves.

This chapter is organised in the following manner. In section 6.2 the data sets are introduced. Section 6.3 illustrates the general properties of the data and shows that it contains two components, the spikes and teh Bragg background. A method

*Chapters 6 and 7 were published in an abridged version as [61].

for separating these two components is presented in section 6.4. In sections 6.5 and 6.6 the properties of these two components are expanded upon and interpreted in terms of physical processes. Finally, in section 6.7 the chapter is summarised and concluded.

6.2 The data sets

The data sets were obtained by DERA, presently QinetiQ, Malvern, with the Maritime Clifftop Radar (MCR). The MCR is a coherent and polarimetric radar operated by DERA with a frequency of 9.75 GHz (X-band). It has a range resolution of approximately 50 cm and a beam width of 1.4°, which corresponds to a cell width of 35 m at a range of 1000 m. Full polarimetry was obtained by switching the transmitter polarisation from pulse to pulse and receiving both polarisations. The PRF of the system was 2 kHz, which effectively resulted in a 1 kHz PRF for each polarisation. The different polarisations were calibrated with respect to each other, which allows the comparison of the two polarisations and the calculation of the polarisation ratio. No absolute calibration was performed.

The data were obtained over a two-day period during an experiment on the southern coast of England, near Portland at the end of February 1999. The radar was set up on a cliff, approximately 50 m above sea level, and looked upwind at a range of 1-2 km. The radar was pointed in a fixed direction, which was approximately into the swell. Limited information is available on the atmospheric and oceanographic conditions. The wind speed, measured at the position of the radar, was 10-15 knots. This corresponds to a wind speed over sea at 10 m anemometer height, W10, of around 6 m/s. The wind and wave directions were approximately from the west. The sea state was estimated to be 2-3. No direct measurements were made of the wave field or currents. The bathymetry around Portland is complicated, but for the data sets the depth should lie between 10 and 30 m.

In total three data sets were obtained, that will be denoted by 1, 2 and 3 in this chapter. The three sets were all obtained under similar conditions and as such exhibit similar behaviour. Sets 1 and 2 were obtained on the same day and are thus very similar. Set 3 was obtained on a separate day and therefore differs somewhat from the other two. Set 1 was chosen to present the general data properties discussed in the next section, but the most important statistical properties of the other two sets are also presented.

6.3 General data properties

In this section the general properties of the seaclutter data are studied. In subsequent subsections the general properties of the seaclutter are described and a

number of spikes are studied in more detail. The physical interpretation of these results will be performed in the next section.

6.3.1 General properties of the seaclutter

In this subsection the general properties of power and Doppler velocity of the full data set are treated. The treatment of the polarisation ratio is an integral part of the analysis of the power. In the next subsection special attention is paid to the spikes.

General properties of the power

Figure 6.1 shows the backscattered power at HH polarisation as a function of range and time of data set 1. The horizontal axis gives the time in [s], the vertical axes the range in [m] and the grey-scale shading gives the power in [dB]. This type of diagram will be referred to as a power-range-time diagram. In total a piece of data 250 m by 20 s is shown. In figures 6.2 and 6.3 similar range-time diagrams of the power at VV and the HH/VV polarisation ratio are presented. The HH diagram shows the same stretch of surface as the VV and HH/VV diagrams. It is displayed larger to better illustrate the different scales of the spikes.

The VV diagram shows a rather smooth cross-section characterised by well-defined bands of higher and lower power. The HH results are much more spiky than the VV results. There is still evidence of the banding pattern, but it is more intermittent than its counterpart at VV. Interestingly, in the polarisation ratio diagram the banding pattern is even weaker than at HH. Superimposed on this banded background the spikes may be observed. They are strongly evident in the HH and in the polarisation ratio diagrams, but at VV they are very hard to distinguish. A thorough comparison of all three diagrams reveals that the strongest events at HH have a VV counterpart. The smaller events at HH disappear in the background at VV. All events at HH do have a counterpart in the polarisation ratio diagram. This is caused by the fact that they strongly exceed the background at HH and almost disappear at VV, whereas the background behaves the other way around.

The spikes are studied more thoroughly in section 6.3.2, but generally two observations can be made. The spikes posses a higher polarisation ratio and they mainly occur on the bands of higher power.

The results of the general background are interpreted in section 6.5, where it is shown that this behaviour matches well with general sea clutter theory. The banding pattern in VV and the background in HH can be associated with Bragg scattering and the events in both diagrams are the so-called sea spikes, mentioned in the introduction.

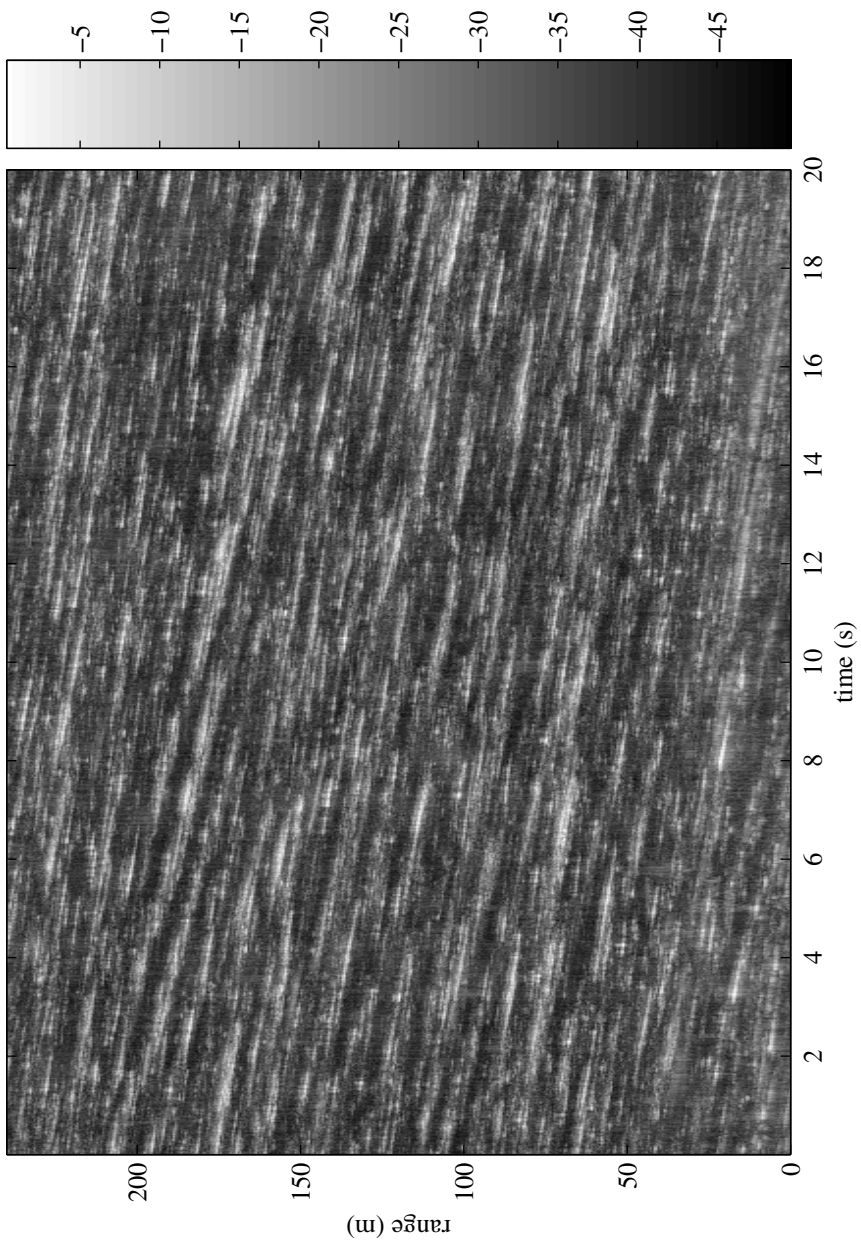

Figure 6.1: Power range-time diagram of data set 1 for HH polarisation. The colour coding gives the power in dB scale.

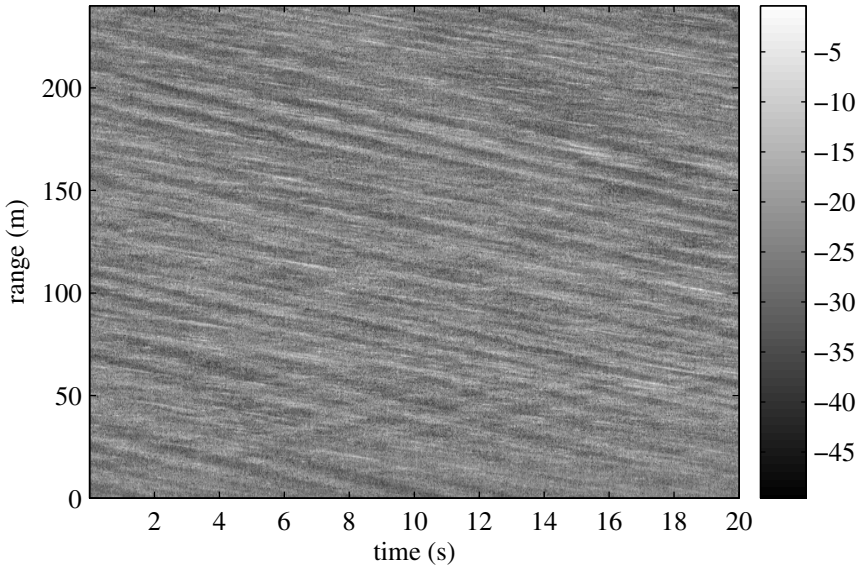

Figure 6.2: Range-time diagram of data set 1 for power at VV polarisation. The grey-scale gives the power in dB scale. The scaling is equal to that of figure 6.1.

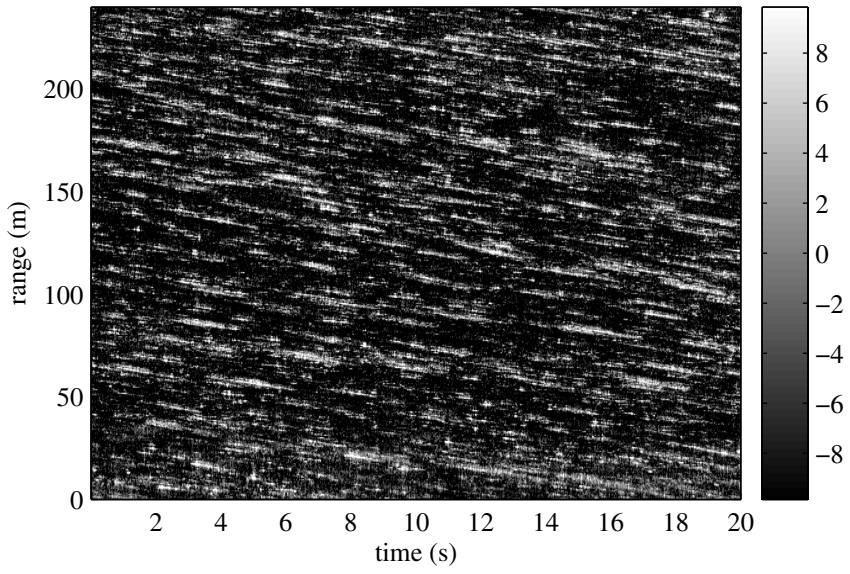

Figure 6.3: Range-time diagram of data set 1 for HH/VV polarisation ratio. The grey-scale gives the polarisation ratio in dB scale.

Inspection of similar diagrams of the other two data sets revealed a comparable behaviour to that of data set 1. Especially data set 2 is very similar to data set 1. Data set 3 exhibits a slightly different behaviour, which might be explained by the fact that it was recorded on a separate day.

As mentioned in section 6.2, the data is coherent. Using Fourier analysis, the phase information can be used to obtain a Doppler velocity, which is based on the Doppler effect and which will be denoted as Doppler velocity throughout this thesis. By measuring the displacement of a certain event over time another velocity may be obtained, which will be called the displacement velocity.

Figures 6.4 and 6.5 present range-time diagrams of the Doppler velocity at VV and HH polarisation respectively. Both diagrams again show evidence of the banding pattern and again the HH velocity diagram is spikier than the VV diagram. Moreover, the HH diagram exhibits a higher velocity than that for VV. Also, spikes can be observed, superimposed on the bands of higher velocity. These are again most evident at HH polarisation, but the larger spikes can be seen in the VV diagram as well. Comparing these diagrams with the power diagrams it is observed that the banding pattern in velocity roughly coincides with the banding pattern in power and that the spikes in velocity match the spikes in power.

General statistical properties

To better study the statistical properties of the different components, histograms have been made of the power and Doppler velocity range-time diagrams for both polarisations, as shown in figure 6.6. These histograms were obtained from the full range and time as shown in figures 6.1 to 6.4. All histograms were normalised using the total number of data points. A similar analysis was performed for all three data sets.

Studying the histograms the following observations can be made. Firstly, the power at HH peaks at a lower level than the power at VV, on average some 10 dB lower. This is supported by a statistical analysis of the polarisation ratio diagram, the mean of which also lies at around -10 dB. Secondly, the distribution width at HH is on average broader than at VV and it also has a much stronger high tail-end. The Doppler velocity diagrams and their properties show the following. The VV results peak at a lower value than those of HH. Moreover, the width is again smaller than the width at HH. As will be shown in section 6.5 the statistical behaviour is indicative of the two different scattering processes, i.e. Bragg scattering and spikes. These types of histograms are analysed in more detail in section 7.3.

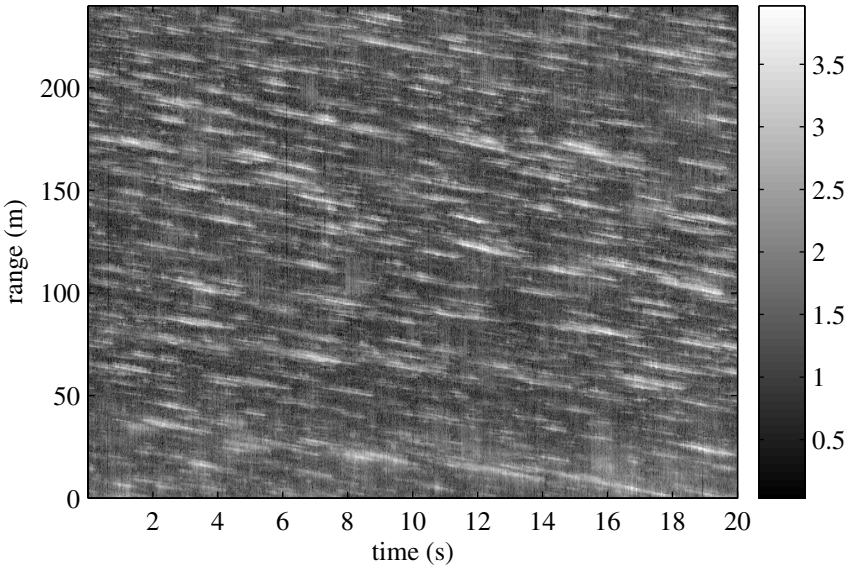

Figure 6.4: Velocity range-time diagram of data set 1 at HH polarisation. The grey level coding gives the Doppler velocity in m/s.

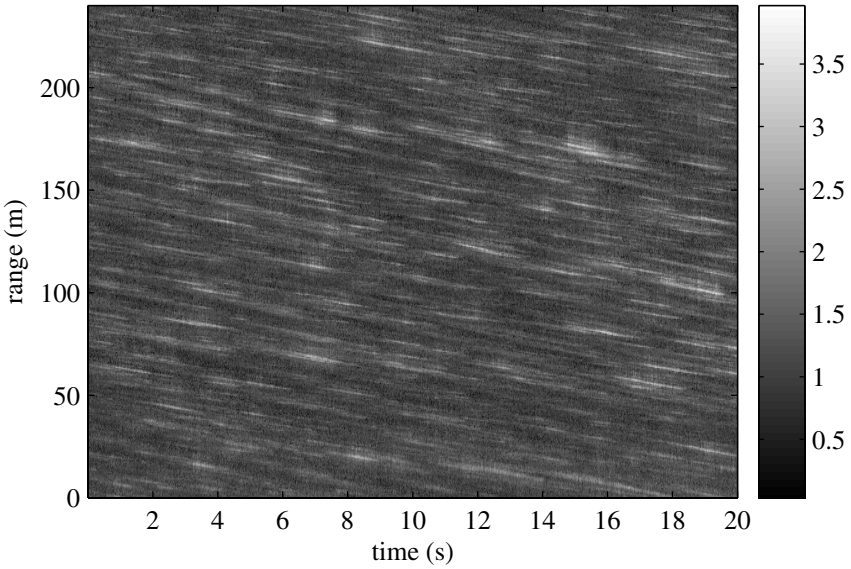

Figure 6.5: Velocity range-time diagram of data set 1 at VV polarisation. The grey level coding gives the Doppler velocity in m/s. The scaling is equal to that of figure 6.4.

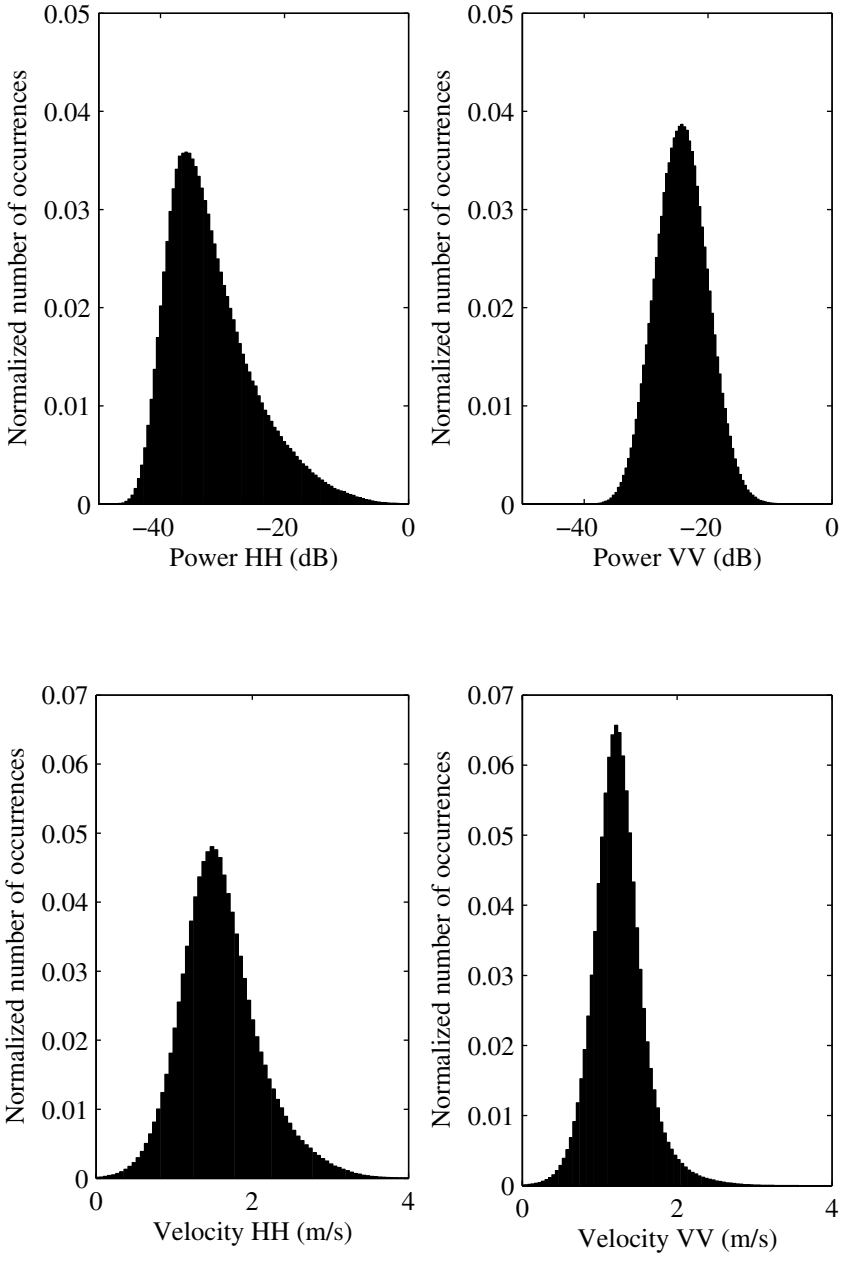

Figure 6.6: Histograms presenting the statistical distribution of Power at HH (upper left) and VV (upper right) and Doppler velocity at HH (lower left) and VV (lower right). All four diagrams have been normalised using the total number of data points.

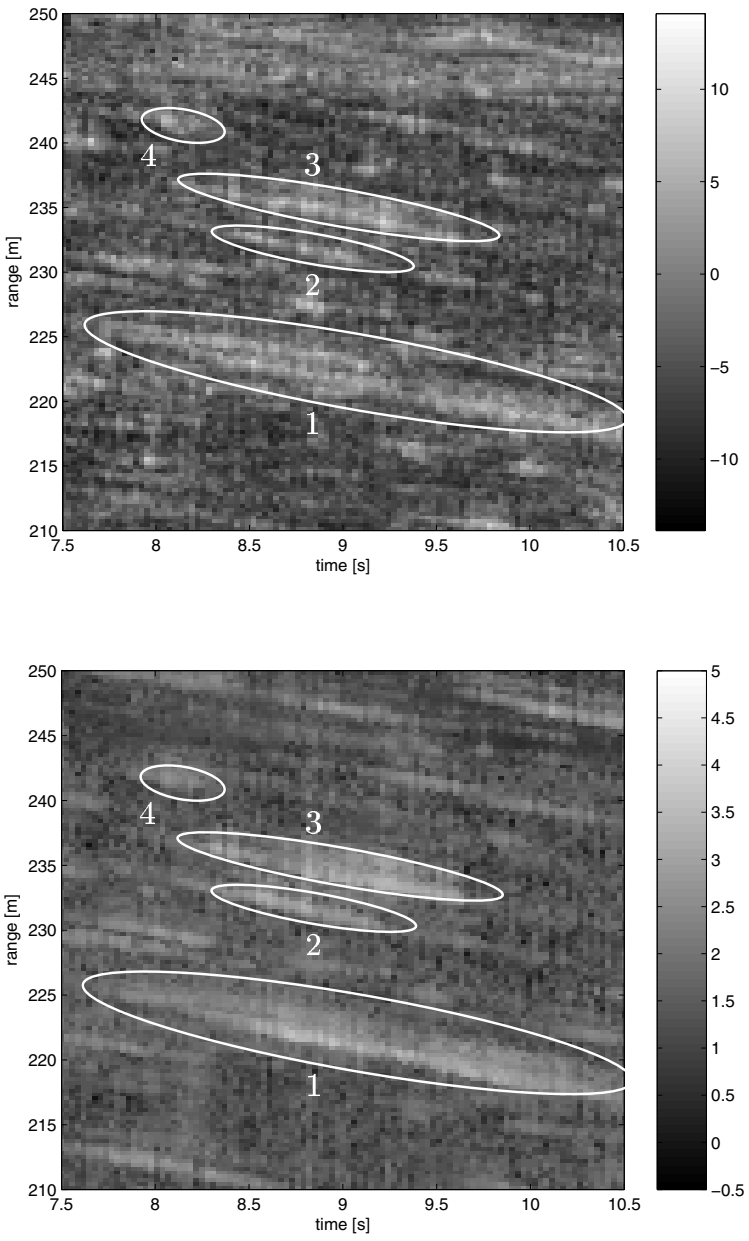

Figure 6.7: Power and polarisation ratio range-time diagrams of data set 1. The upper panel presents the HH/VV polarisation ratio and the lower panel the Doppler velocity at HH polarisation. The colour coding gives the polarisation ratio in dB scale, respectively the Doppler velocity in m/s.

Table 6.1: Scales of the spiking events from figure 6.7

	HH/VV (dB)	v_{HH} (m/s)	ΔR (m)	Δt (s)
1	9.4	3.7	3.5	2.5
2	7.0	3.3	1.2	0.8
3	10.1	3.3	2.1	1.3
4	6.5	2.6	1.2	0.4

6.3.2 General behaviour of the sea spikes

To better study the different properties of spiking events, range-time diagrams of polarisation ratio and Doppler velocity are presented in figure 6.7. Both panels show a close-up of the data, 40 m in range and 3 s in duration. The polarisation ratio, see figure 6.7, again shows the two components, Bragg and spikes. The Bragg background has an average polarisation ratio of -10 dB, while for the spikes it is much higher, > 0 dB.

Figure 6.7 shows that the average Doppler velocity of the banding pattern lies around 1 m/s, while the difference between the bands is approximately 0.5 m/s. The spikes again stand out as their velocity is higher, typically 2 m/s or higher, than that of the Bragg background.

As mentioned in section 6.3.1, a detailed comparison of range-time diagrams of power, polarisation ratio and Doppler velocity revealed that the spikes coincide in all three diagrams. This showed that the spikes are characterised by a high power, polarisation ratio and velocity. To better study the properties of the spikes, four of them have been marked in figure 6.7. Their properties are summarised in table 6.1. The maximum value of the polarisation ratio and Doppler velocity was determined for each event as well as its physical size (in range) and duration. The table shows that larger events (in range) also last longer and possess larger radial velocities. There is a trend showing larger polarisation ratios for the larger spikes, but this relation is not conclusive. Note that even the smallest event has a maximum polarisation ratio well above 0 dB.

6.3.3 Recapitulation

Summarising, the seaclutter consists of two components, a (Bragg) background, which exhibits a banding pattern in power and Doppler velocity, and, superimposed on these bands, a number of spiking events. The background is characterised by

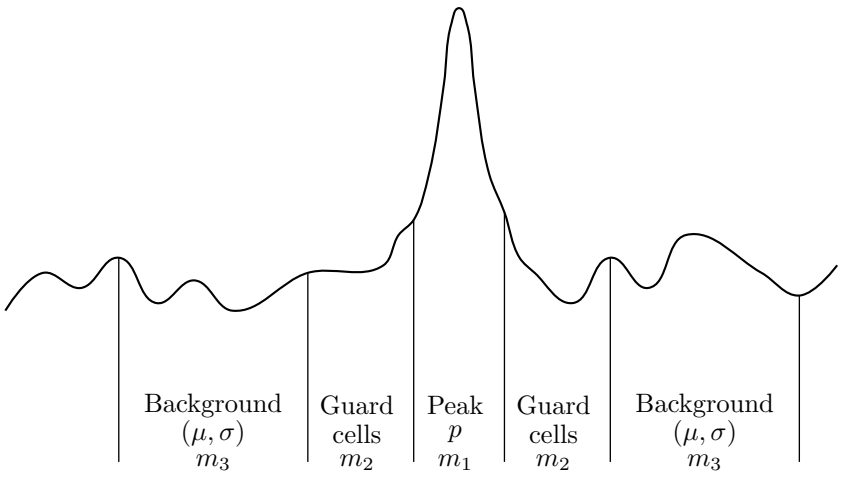

Figure 6.8: One dimensional CFAR principle: Three regions are identified, the background, the guard cells and the peak. Here the background is assumed to be the fusion of both background regions.

a negative polarisation ratio around -10 dB and low Doppler velocity, whereas the spikes have much higher polarisation ratios and radial velocities. A more detailed analysis of the spikes revealed that the largest spikes also have the largest velocity and generally a larger polarisation ratio than the smaller spikes.

6.4 Separation of the Bragg and spike components

The spikes stand out against the background in the power, Doppler velocity and polarisation ratio diagrams, as was shown in the previous section. For the first two properties the effect was strongest at HH polarisation. To properly distinguish the spikes from the background an algorithm based on the constant false alarm rate method (CFAR) was used.

Figure 6.8 illustrates the CFAR-like algorithm as it was used in this thesis. The figure shows a fragment of a signal from which events need to be detected. Three regions are identified: the central peak, the guard cells and the background. The central peak, consisting of m_1 pixels, is the region that is assumed to exceed the background. The average power of this region is denoted as p. The guard cells are the regions, i.e. m_2 cells, directly around the peak. They are assumed to be influenced both by the peak and the background and as such not to be representative of either. Therefore, they are excluded from the analysis. The background consists of the regions outside the guard cells. It has a size of m_3 cells and is assumed

to have an average power μ and a standard deviation σ. Given these definitions, the CFAR-like algorithm assumes that the peak exceeds the background when the following criterion is met:

$$p > \mu + n\sigma, \tag{6.1}$$

where n is the threshold value. A large value of n will lead to fewer false alarms, but also to exclusion of the weaker events. Low values of n have the opposite effect, a higher number of false alarms, but fewer misses.

A total of four parameters governs the CFAR-like analysis, m_1, m_2, m_3 and n. The sizes m_1, m_2 and m_3 need to be chosen in such a manner that the regions fulfil their task. Visual inspection of a number of the larger spikes showed that the events have a large extent in time, but a restricted extent in space, i.e. two to three range bins. Thus the CFAR was performed in the range direction. A peak size of $m_1 = 1$ bin was chosen in combination with $m_2 = 3$ bins. Finally, the background was estimated using a value of $m_3 = 8$ bins. The value of m_3 was kept low because the spikes may lie close together and contamination from other spikes is undesirable.

One parameter, n, remains to be determined. The easiest way of determining a value of this parameter is first deriving the CFAR statistics for the entire set and then estimating a threshold value from these statistics. The CFAR statistics are defined as,

$$\frac{p - \mu}{\sigma}. \tag{6.2}$$

By applying this formula to each bin, the CFAR statistics for the entire set can be determined. The results of this analysis for power, polarisation ratio and Doppler velocity are shown in figure 6.9. In this figure histograms of the distributions of the CFAR parameter for all three quantities are presented. Studying these results it can be observed that the three distribution are mostly Gaussian in nature. They are slightly skewed, with a high tail-end. This high tail probably contains the larger spikes. Given the Gaussian shape of the distributions it is possible to define a value for the parameter n. In this work a value of $n = 2$ was chosen, which results in a 5% chance of false alarms, but allows the detection of smaller spikes.

The CFAR-like analysis was performed on the three diagrams. The pixels that exceeded the background in all three diagrams were identified as belonging to a spike. The results of this analysis are shown in figure 6.10. A visual comparison of these results to figures 6.1 and 6.7 shows that this method is indeed capable of positively identifying the spiking events. A clustering algorithm was applied to the CFAR results to obtain the separate spiking events. In total 4668 spikes were found for set 1, 5035 spikes for set 2 and 8808 spikes for set 3. Dividing by the total range and time of the interpreted data gives densities of 0.93 $m^{-1}s^{-1}$, 1.01 $m^{-1}s^{-1}$ and 1.76 $m^{-1}s^{-1}$. In section 6.6.2 these results are interpreted.

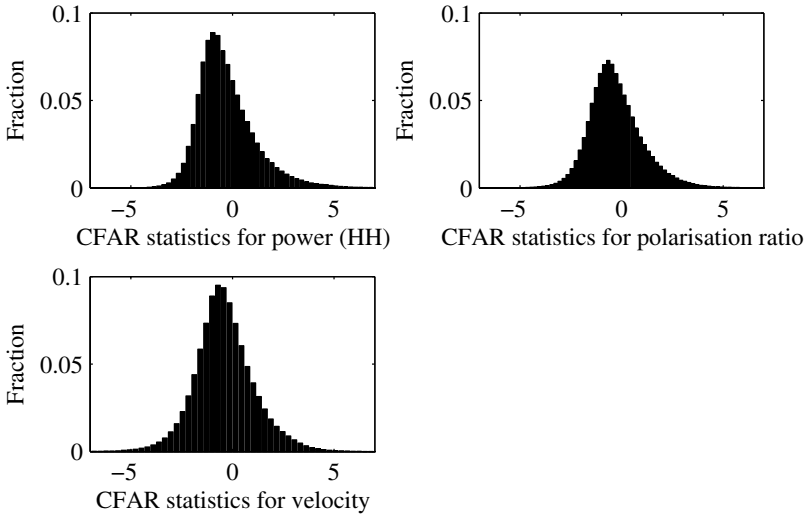

Figure 6.9: CFAR statistics for the power, Doppler velocity and polarisation ratio diagrams. The horizontal axis gives the bins of the statistical parameter from equation 6.2. The vertical axis denotes the fraction for each bin.

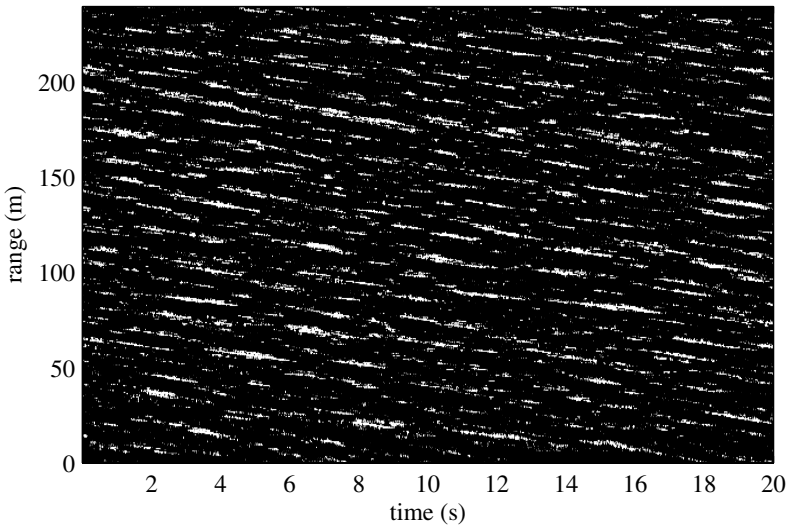

Figure 6.10: Results of the CFAR-like analysis of data set 1. The vertical axis denotes the range and the horizontal axis the time. The pixels identified as belonging to a spike were given a value of 1 (white) and the background is set to 0 (black).

6.5 Physical interpretation 1: The tilt-modulated Bragg background

Standard sea clutter theory predicts a background of tilt-modulated Bragg scattering, which is especially strong at VV polarisation, [47, 68, 103]. This was treated more thoroughly in chapters 3 and 5. The properties of the global background as shown in section 6.3 indeed show the type of behaviour expected of tilt-modulated Bragg scattering. The bands of higher power correspond to the regions in front of and on the crest of the larger waves, where a positive tilt (towards the radar) enhances the Bragg scattering. The bands of lower power are the regions behind the crest and in the trough where the negative tilt reduces the Bragg scattering and/or causes shadowing. Thus, the banding patterns reflect the larger waves, that cause the tilt-modulation. Due to the fact that the radar looked upwave, no projection effects have to be taken into account. Thus, properties of the wavefield can be derived directly from the range-time diagrams. The physical interpretation is carried out for the power, the velocity and the polarisation ratio range-time diagrams. The histograms are treated in the next section as a good understanding of those diagrams requires understanding of the spiking events.

6.5.1 Interpretation of the Power diagrams

The banding pattern in the power diagrams reflects the wave field. Therefore, Fourier analysis can be applied to the range-time diagrams to give both the spectrum (1D FFT) and the dispersion relation (2D FFT) of the wavefield. This technique has been used earlier by for instance [77, 78, 120]. Examples of the results from the Fourier analysis for data set 1 are shown in figure 6.11.

The spectra for all three sets contain a number of peaks, corresponding to waves of different wavelengths. The wavelengths of the dominant waves are summarised in column 2 of table 6.2. In the third column the corresponding theoretical phase velocity is presented. The actual phase velocity could be estimated from the displacement of the actual waves in the range-time diagrams. These values are presented in column 4.

The dispersion relation can be used to estimate the radial component of the current, as described in [120] and section 2.4. The procedure is as follows. Start with the dispersion relation such as the one in figure 6.11. The theoretical dispersion relation for water waves is known. The formulation for deep water with current is:

$$\omega(k) = \sqrt{(gk + \gamma k^3)} + \mathbf{v} \cdot \mathbf{k}, \tag{6.3}$$

where $\gamma = \tau_s/\rho$ is a constant describing the surface tension and $\mathbf{v}$ is the current velocity vector. For these data sets we only have the radial component of the velocity, so that the second term in the equation simply becomes $\mathbf{v} \cdot \mathbf{k} = vk$. Thus,

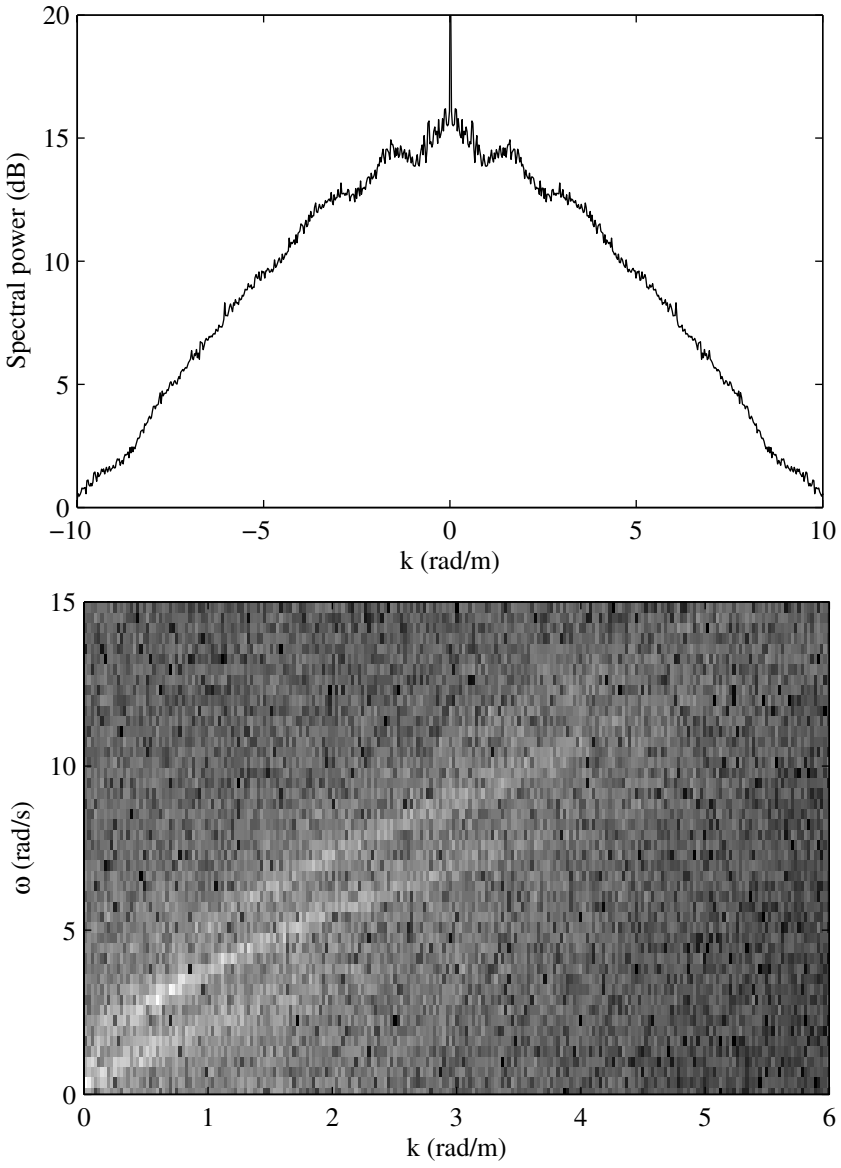

Figure 6.11: Results of the Fourier analysis of data set 1. The upper panel shows the spectrum, resulting from a 1D FFT. The lower panel presents the dispersion relation, resulting from a 2D FFT.

Table 6.2: Wavelengths and velocities

	λ_{dom} (m)	$v_{\mathrm{ph,cal}}$ (m/s)	$v_{\mathrm{ph,m}}$ (m/s)	$v_{c,k\leq 3}$ (m/s)	$v_{c,k>3}$ (m/s)
set 1	10	4.0	4.5	0.5	0.8
set 2	12	4.3	4.8	0.5	0.75
set 3	70	10.5	10.8	0.3	-

by fitting the theoretical dispersion relation to the relation from the data the only unknown, the current, can be determined. One practical problem may occur. As can be seen in figure 6.11 the diagram exhibits some contamination at either side of the main dispersion relation. This contamination may occur due to non-linear processes such as scattering from spikes, shadowing and system noise. It was possible to filter out these contaminations, which resulted in a usable dispersion relation.

This procedure was applied to the three data sets, the results of which are shown in table 6.2. The high range resolution of the radar system does allow the determination of currents for both the large and the shorter waves. The currents for the long waves, $k \leq 3$, and the currents for the smaller waves, $k > 3$, are given in columns five and six of the table. For data set 3 the shorter waves were not well enough defined to determine the current they were subject to. Estimating from the other two sets it should be between 0.5 and 0.6 m/s.

6.5.2 Interpretation of the velocity diagrams

The Doppler velocity diagrams also exhibit banding patterns, obviously of higher and lower velocity, that roughly coincide with the bands of higher and lower power. The direction of the orbital velocity at the crest of a wave is opposite to that in the trough. This causes the banding pattern in Doppler velocity, which consequently coincides roughly with the banding pattern in power. For all three sets the difference between the bands was around 0.5 m/s. The orbital velocity is therefore equal to half of this difference, i.e. 0.25 m/s.

Additionally, it was observed from the statistical analysis that the average Doppler velocity of the Bragg component was approximately 1.2 m/s. This average Doppler velocity consists of three components. The first component is the intrinsic, i.e. phase, velocity of the scatterers, which for low grazing angle X-band Bragg scattering is approximately 0.25 m/s. The second component is the current, which follows from table 6.2: 0.8 m/s. The third component is the wind drift, which is approximately 2 to 3% of the wind speed, i.e. 0.15 m/s. Thus, the total expected velocity should be around 1.2 m/s, which corresponds to the measured

average velocity of 1.2 m/s. Note that for the larger waves, the wind drift should not be taken into account as it only affects the top 10 cm of the ocean surface.

6.5.3 Interpretation of the Polarisation ratio diagrams

The polarisation ratio is less dependent on incidence angle then the power, which explains the absence of the banding pattern. However, its magnitude is too high for Bragg scattering. From composite surface theory, [68, 103], the polarisation ratio for LGA seaclutter is expected to be in the range of -30 to -20 dB, whereas the measurements show a polarisation ratio of -10 dB. This discrepancy is treated in detail in section 7.6.

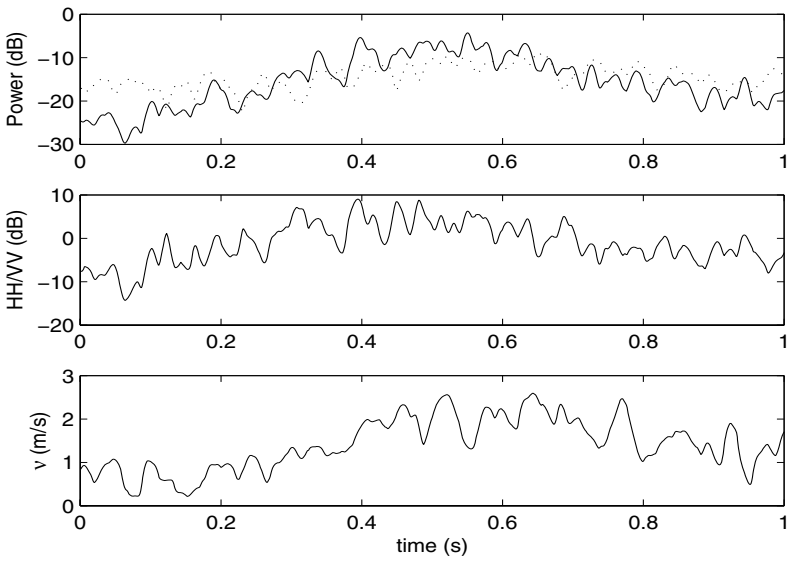

Figure 6.12: Properties of a spiking event. The top panel shows the power as a function of time. The solid line is HH and the dotted line VV polarisation. The middle panel is the polarisation ratio and the lower panel the Doppler velocity at HH.

6.6 Physical interpretation 2: The spikes

In section 6.4 a method was presented, that made it possible to separate the spikes from the background. This allows an advanced temporal analysis of these events as

well as a statistical analysis of the full set of spikes.

6.6.1 Temporal analysis of sea spikes

Consequently, one of the larger events was selected. A full Doppler-time analysis of this event was performed in the following manner. Firstly, the beginning of the event was determined by hand. The event was then tracked by estimating the radial shift over time from the Doppler velocity. Finally, a time-frequency analysis was applied to the data along the track. From this analysis the time behavior of the spiking events may be mapped in detail, as shown in figure 6.12. The power and the polarisation ratio follow directly from the track. The Doppler velocity is obtained from the Doppler-time analysis by taking the first moment in Doppler. To reduce contamination by the Bragg scattering, HH polarised data was used for this analysis. The current and the orbital velocity have been subtracted from the results shown in figure 6.12.

The event starts at t=0 s and over the first 0.35 s it is characterised by a slow increase of the power at HH and a corresponding increase in the polarisation ratio. Then from t = 0.30 s to about 0.40 s the power increases approximately 10 dB. At the same time the polarisation ratio reaches a maximum. Both the power and the polarisation ratio vary around this high level for approximately 0.30 s and then decay. From t = 0.20 s the velocity slowly increases, a process which accelerates around t = 0.30 s. Around t = 0.55 s the velocity reaches a peak, after which it remains high until t = 0.65 s. After this maximum all three properties decay and around t = 1.0 s they are almost at ambient level again.

Studying multiple events in a similar manner reveals that most of them exhibit similar behavior: all but the smallest events are characterised by an increase in power accompanied by an increase in polarisation ratio. After a plateau in the level of all three properties they slowly decrease to the background level. The Doppler velocity lags somewhat behind the two other properties, but essentially exhibits the same increase plateau and decay phases. Incidentally, the plateau at velocity seems to be accompanied by a broadening of the Doppler bandwidth. As was shown in section 6.3.2 the larger a spike, the stronger the peak in all three properties. Only the smallest spikes show little or no increase of the velocity after the peak in power and polarisation ratio.

6.6.2 Statistical interpretation of the spikes

Sea spikes have been linked to specular or multipath scattering on steepened or breaking waves by a number of researchers, see [30, 39, 58, 115, 116, 118]. It was shown that radar scattering on breaking wave profiles is characterised by a sudden strong increase in scattering power as well as in polarisation ratio. The high power

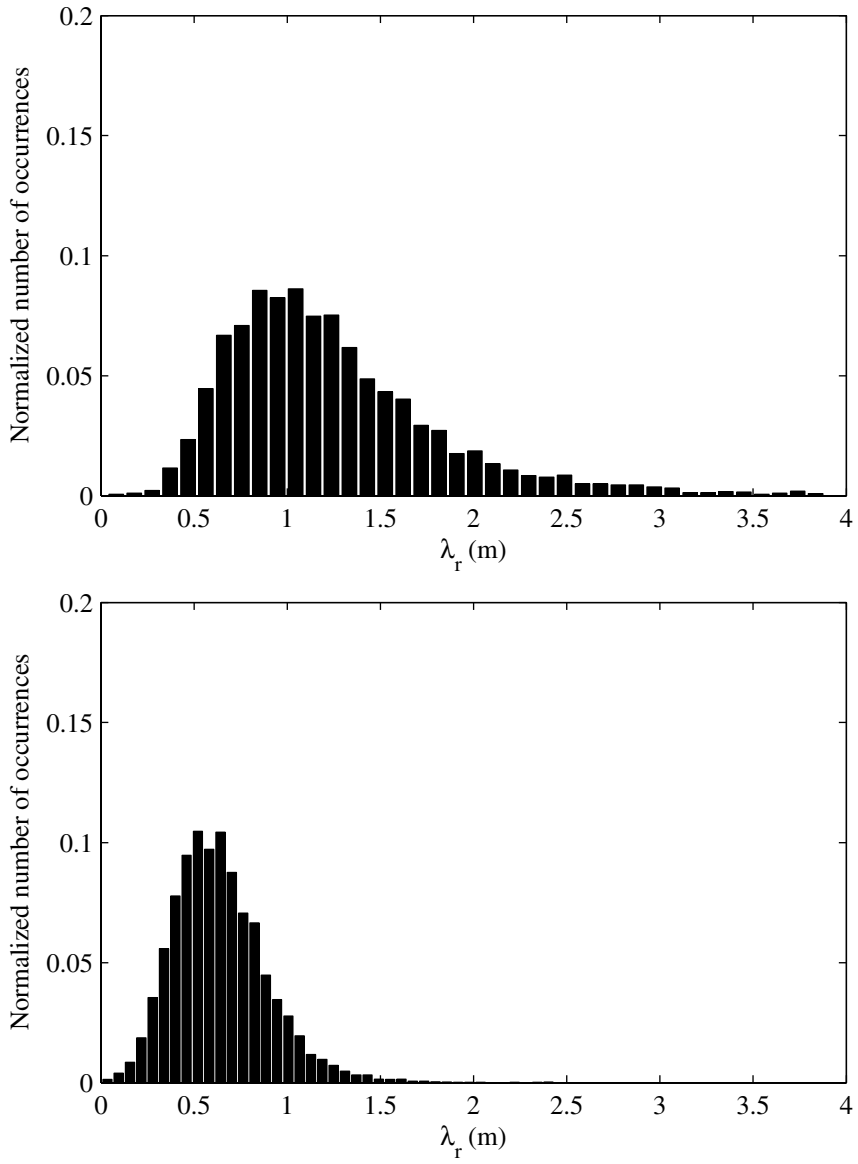

Figure 6.13: Statistics of the spiking events. The upper panel shows a histogram of the spike wavelengths from the data set 1, while the lower shows the same for data set 3.

and polarisation ratio are explained by the fact that the scattering on breaking waves is specular in nature. These breaking wave events have many sizes, the larger of which are a few meters in size. As will be shown in the next section, the intrinsic velocity of these spiking events is equal to or even greater than the phase velocity of the corresponding breaking waves. The breaking waves are larger than Bragg waves and thus possess higher radial velocities. This fact can be used to estimate the size of the breaking waves.

Because spikes occur mainly on the crests of dominant waves, the Doppler velocity of the spikes is composed of three components. These components are the current, the orbital velocity of the dominant waves and the intrinsic velocity of the breakers themselves. The current follows from table 6.2 and the orbital velocity was determined to be around 0.25 m/s. The intrinsic velocity could be calculated by subtracting these two components from the measured Doppler velocity. The Doppler velocity of each spike was estimated by calculating the median of the radial velocities of all pixels comprising the spike in the Doppler range-time diagram. The median was used to exclude contamination of pixels dominated by Bragg scattering or scattering from the jet. The resultant intrinsic velocity is a good approximation of the phase velocity, v_{ph}, of the breaker. Finally, the wavelengths, λ, of the breakers were determined from these phase velocities using the well-known relation:

$$v_{ph} = \sqrt{\frac{g\lambda}{2\pi}}, \rightarrow \lambda = \frac{2\pi v_{ph}^2}{g}, \tag{6.4}$$

where $g = 9.81$ m/s^2.

In figure 6.6.1 the results from this analysis for sets 1 (upper panel) and 3 (lower panel) are presented. The results of set 2 are almost equal to those of set 1 and are therefore not shown. Both panels present histograms of the wavelength distribution of the breakers as obtained from the spiking events in both data sets. The histograms were normalised by the total number of spikes in each set.

The results for set 1 reveal that most of the breakers giving rise to spikes have a wavelength around 1.0 m. Below 0.5 m there is a rapid fall-off of the number of spikes. This is probably due to the fact that smaller spikes become increasingly difficult to positively distinguish from the background. The distribution does have a long high tail end, showing wavelengths up to 4 m. This illustrates that, although they are less common, large breakers also occur. The results for set 3 exhibit the same general shape of the histogram, but the distribution is less broad and the maximum lies around 0.6 m. This reflects the observation, which was made in section 6.3, that the spikes were smaller for this set than for the other two. Also, the high tail end is much smaller, which shows that the largest events occurring in the other two sets do not occur in set 3.

The results from both data sets show that, although relatively large waves can break, the waves that do break are clearly not the dominant waves, but waves that

are at most one third as long as the dominant waves. Below that upper boundary, however, the breakers possess nearly every possible wavelength, even down to waves of only a few dm in size.

6.7 Conclusions

In this chapter the analysis of three sets of high-resolution, X-band, coherent and polarimetric radar data, obtained at LGA, was presented. From this analysis the following conclusions can be drawn. The seaclutter was found to consist of two parts, a tilt-modulated Bragg background, with superimposed on this background spiking events that are caused by the scattering on steepened and/or breaking waves.

The Bragg background completely dominates the VV polarised clutter and significantly contributes to the HH clutter. However, the HH is strongly influenced by the spikes, too. The Bragg background is characterised by a banding pattern, both in power and velocity. This pattern is caused by the tilt-modulation associated with the underlying swell. It could, therefore, be used to estimate the properties of the swell, such as the wavelength and velocity of the dominant waves and the water current.

The spikes are especially prominent in the HH diagrams and as such also stand out in the polarisation ratio. They are discrete events that are characterised by a heigthened Doppler velocity and polarisation ratio. Assuming that they are caused by scattering on breaking waves, the properties of these breakers could be estimated. This hypothesis is treated in detail in the next chapter, where the results of the current chapter are matched with the results of the modelling efforts of chapter 5.

Chapter 7

Validation of the model*

7.1 Introduction

In this chapter a comparison is made between the results of the model that was presented in chapter 5 and the measured data from chapter 6. It will be shown that the model is capable of simulating radar seaclutter data with a high level of confidence.

To allow the comparison of the model and the data, they have to be presented similarly. The outputs from the models are simulated range-time diagrams of the measurable properties: power, polarisation and measured (Doppler) velocity. This is equal to the way that the measured data is presented prior to the analysis. This means that the interpretation of the simulation results can mostly be performed in the same manner as that of the measured data.

It will also be shown that the model results, based on tilt-modulated Bragg scattering, predict a background polarisation ratio that is lower than its counterpart from the data. This result is explored and a number of solutions is presented.

This chapter is set up in the following manner. In section 7.2 the settings of the model are discussed, with which the simulated results were obtained. In section 7.3 the range-time diagrams mentioned above are presented and their general properties are discussed. In section 7.4 a statistical interpretation, similar to that in section 6.3.1, is performed. The spikes are studied in detail in section 7.5. Finally, in section 7.6 the polarisation ratio difference between the model and the data is discussed.

*Chapters 6 and 7 were published in an abridged version as [61].

Table 7.1: Meteorological parameters for the model

W_{10}	Wind speed	7 m/s
θ_i	Incidence angle	87°
ak_{crit}	Critical steepness value	0.36

7.2 Model fine-tuning

In this section the settings of the model are given that were used to obtain the simulated data presented in this chapter. Moreover, a number of fine-tuning issues of the model are resolved.

The model presented in chapter 5 uses a number of physical input parameters: the wind speed at 10 m anemometer height, W_{10}, which defines the equilibrium spectrum, the two breaking wave criterion parameters, $ak_{\text{crit}}, ak_{\text{width}}$ and the global incidence angle, θ_i. The wind speed and incidence angles can be derived from the radar set-up as described in section 6.2. An estimated value for ak_{crit} was obtained from the literature. These values are summarised in table 7.1. Only the value of ak_{width} has to be determined from the match with the data, which will be treated later on in this section. In the following subsection the various fine-tuning issues are discussed.

Spectral matching

In the model, presented in chapter 5, the ocean spectrum is simulated by an equilibrium spectrum. These types of spectra are generated by measuring ocean spectra over a wide range of circumstances and averaging them to obtain a smooth parameterisation of the true function. A sea spectrum will always deviate from that average due to local circumstances, which is also the case for the data that was presented in chapter 6. The processes that may cause this deviation are, for instance, bottom topography, wave reflection on the coast and changing weather conditions. Whatever the cause of the deviation, for a satisfactory comparison between the model and the data, a good spectral match is necessary. This implies a slight modification of the equilibrium spectrum as elaborated upon in this section.

Figure 7.1 presents the modified simulated spectrum (left panel) and the measured spectrum (right panel). Both spectra were obtained in the same manner. A spatial Fourier transform is applied to the VV polarised range-time data, after which an averaging over time is performed. The result is the wavenumber spectrum of the (simulated or measured) data. Studying the measured data spectrum it can be observed that the spectrum differs from an equilibrium spectrum in two ways. Firstly, the dominant waves in the measured data, which have a wavelength of 10

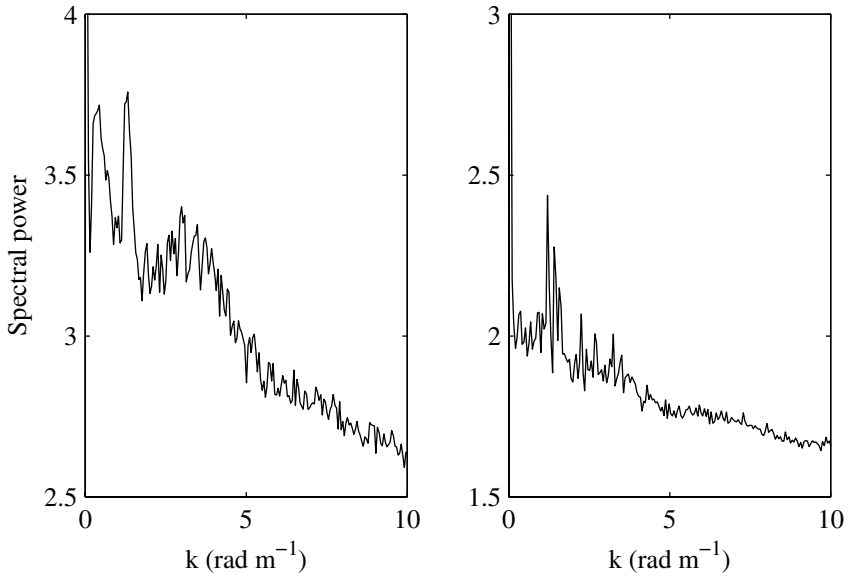

Figure 7.1: Ocean spectra. The left panel gives the spectrum from the simulated data and the right panel the spectrum from the measured data. Both spectra were obtained at VV polarisation.

m, are linked with a spectral peak around $k = 0.62$. Secondly, there are a large number of small peaks around $k = 1.57$. These two features were put into the model spectrum as can be seen in the left panel. Both features are modelled as Gaussian functions that are added to the equilibrium spectrum. The peak has a mean of $k = 0.62$, a variance of $2\pi/100$ and an amplitude of 0.25. The smaller peaks are modelled by a single feature with a mean of $k = 1.57$, a variance of $2\pi/10$ and an amplitude 0.03. The simulated spectrum shown in the left panel of figure 7.1 was obtained from the simulated power range-time diagram at VV polarisation in the same manner that the measured data spectrum (right panel) was. Comparing the simulated spectrum to the measured one, it is observed that the match between the two spectra is better than for the equilibrium case. The simulated spectrum retains more power at lower frequencies. This is due to the fact that bottom topography has not been included in the model.

Incidence angle

One of the unknowns of the observational parameters is the specific range at which the data was observed. All information that is available to the author is that the

observations were made over a range of one to two kilometres. The altitude of the antenna of the radar was approximately 50 m. The imprecise information about the observation configuration makes it difficult to precisely calculate the incidence angle on the surface. Given the height h and the range R the incidence angle follows from $\theta_i = \arccos \frac{h}{R}$. From this it follows that the incidence angle for a range of 1000 m would be approximately 87°, which is the value that was used for the simulations, and 88.5° for a range of 2000 m. Even though there is a slight uncertainty about the incidence angle, it will be shown that it does not seriously affect the results of the simulations.

Breaking wave criterion

In the model there are three parameters that govern the breaking rate and wavelength distribution of the resulting breaking waves: the threshold value for ak, the width of the ak synthesis and the duration of the spikes. Here, estimations for these three parameters as used in the model are presented.

Firstly, a number of values for the threshold value for ak were presented in chapter 5. The value of 0.36 from [8] was chosen for two reason. This value is the most recent one from the list and as such uses the most current insights in this topic. Moreover, it was compared to some of the other values, see [7], and found to best predict wave breaking.

Secondly, the width of the spectral band in the breaking criterion is one of the central parameters of the model. Given a value of ak_{crit} it governs the rate of breaking wave generation. Due to fact that the breaking wave model was derived during this PhD project, no values for this parameter can be obtained from literature. Therefore, a value for this parameter is derived in this chapter by matching the statistical properties of spikes in the data to those of from the model. It was found that the best results were obtained when the filter width in equation 5.12 was set to $N/4$, where N is the number of k values included in the spectrum.

Thirdly, the duration of a breaking wave event is derived in the following manner. Three stages of a breaker can be identified. Firstly, the onset is the period of time during which the wave steepens and forms a jet. Its duration can be derived from the analysis of [109]. In that article calculations are performed about the onset of a breaking event, which allows the matching of its duration to the wavelength of the breaker. For instance, the duration of the onset is approximately 200 ms for a 2.3 m wave. The second and third stages of the breaker, during which the whitecap is formed and the event fades away, can be derived from the data and it was found to be approximately four times the duration of the first stage.

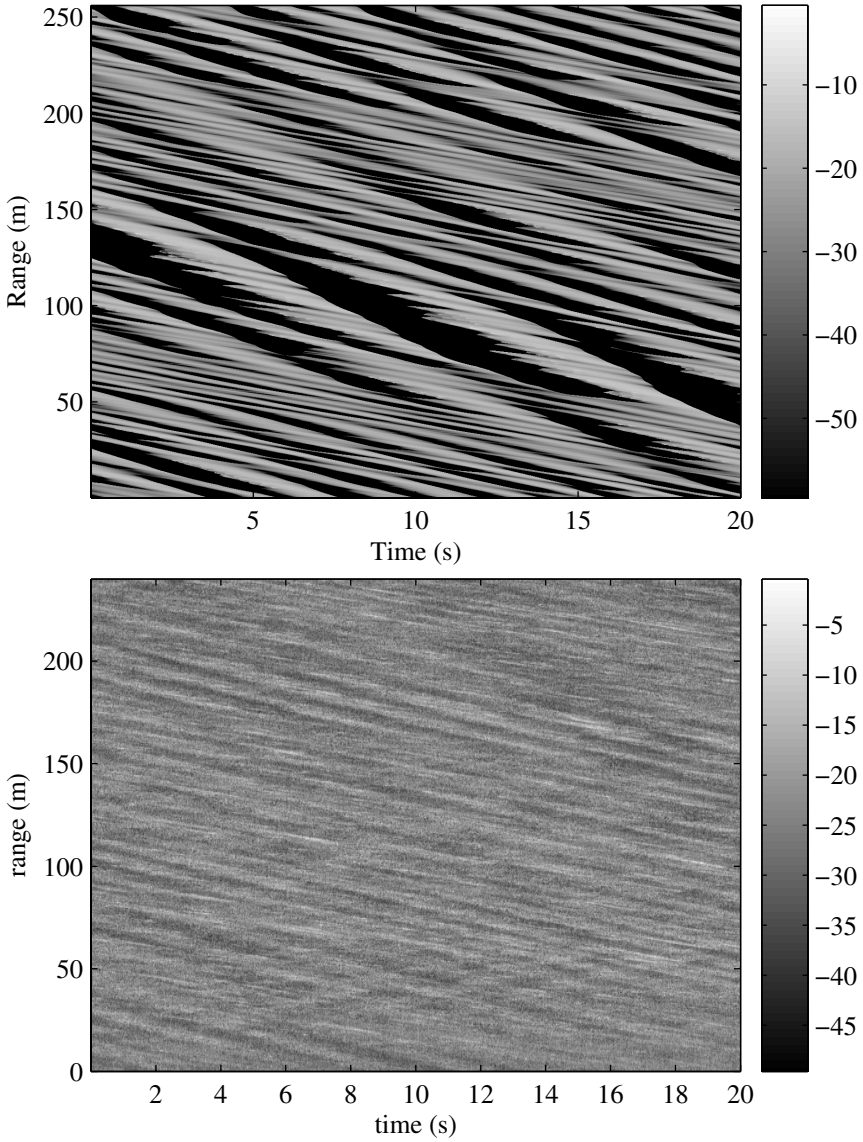

Figure 7.2: Power range-time diagrams for VV polarisation. The upper panel shows the RCS as a function of range and time obtained with our model, while the lower panel shows similar results for data set 1 from chapter 6. For both diagrams the gray-scale gives the RCS in dB scale.

7.3 Global comparison

In this section the simulated and measured data are compared on the basis of two representations: Range-time diagrams and histograms.

7.3.1 Range-time diagrams

The main outputs of the model of chapter 5 are range-time diagrams in Power and (Doppler) velocity for HH and VV polarisation. These are similar to the range-time diagrams of section 6.3.1. An example of a range-time diagram for VV power of the simulated data is compared to the corresponding diagram of the measured data in figure 7.2. Comparing the two panels reveals similar patterns in both diagrams, corresponding to the wavecrests. This suggests that the model is capable of modelling these types of structures with reasonable accuracy. A second observation that can be made is that the shadowing in the simulated diagram is stronger than in the measured data. The simulated shadowed regions possess a cross section which is set equal to an assumed 'dark current of -100dB, while the measured shadowed regions lie only some 10 to 20 dB below the non-shadowed regions. As explained in the previous section and in appendix C this is a feature of 2D models. The shadowing in a 3D model is usually modified by the directional spread of the wavefield. Only very high (cross-range) resolution observations will match 2D models.

The model is capable of generating the same diagrams that were presented for the measured data. However, for a good comparison between the simulations and the measurements a statistical analysis is needed, which is performed in the next section.

7.3.2 Histograms

Figure 7.3 presents histograms of the full simulated and measured data sets. The panels on the left give the model results, while those on the right give the data results. The properties presented are from top to bottom: power at HH, power at VV, Doppler velocity at HH and Doppler velocity at VV.

In the previous chapter a thorough analysis of the measured seaclutter data was made. Studying the histograms of HH and VV power, see figure 6.6, it may be observed that the data distributions are roughly Gaussian in shape in dB scale. The HH results, however, do exhibit a non-Gaussian high-tail. Nonetheless, for a good comparison between the model and the data results, Gaussian shapes are desirable. Therefore, the power distributions are compared in dB scale rather than in linear scale.

Studying the histograms in figure 7.3 for the power, it may be observed that

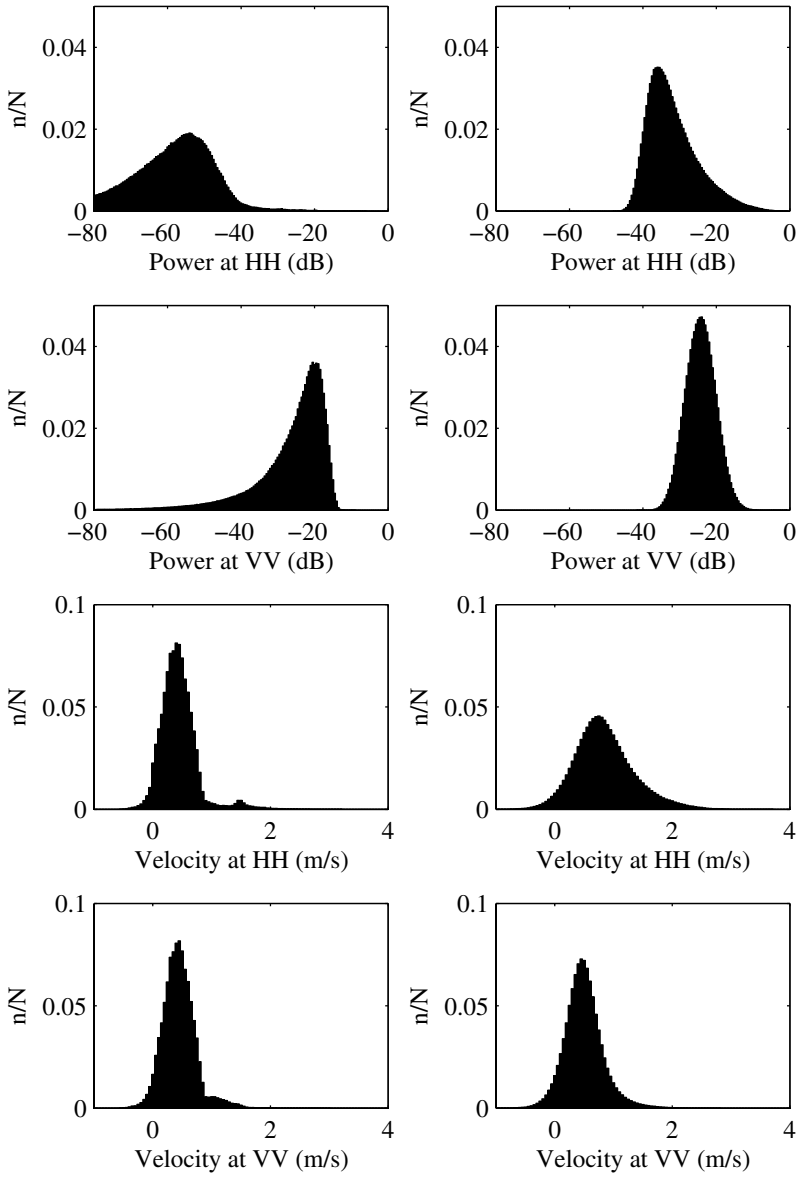

Figure 7.3: Statistical comparison of the model and data results. The panels on the left show histograms of the model results for power at HH and VV as well as the velocities at HH and VV. The panels on the right show similar diagrams for the data results. All results are for the entire data and model sets.

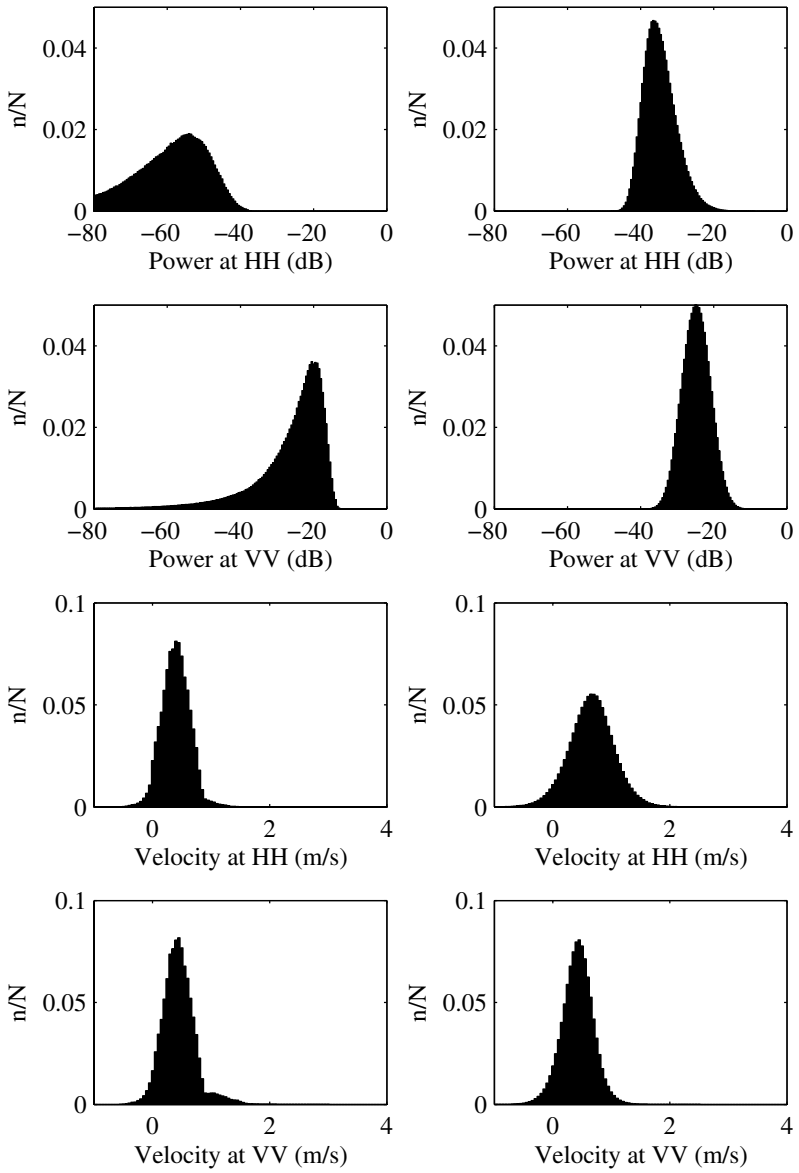

Figure 7.4: Statistical comparison of the model and data results. The panels on the left present histograms of the model results for power at HH and VV as well as the velocities at HH and VV. The panels on the right show similar diagrams for the data. All results are for the data and model sets without the detected spikes.

they indeed exhibit a Gaussian-like central peak. They also possess both left-hand, i.e. low-power, and right hand, i.e. high-power, non-Gaussian tails. Especially the simulated power diagrams both exhibit a strong low-power tail. This tail is a feature for LGA two-dimensional models, which is explained in detail in appendix C. For 2D models the effects of near-shadowing cause a wide spread of power, which, in turn, causes the tail. For 3D models the directional spread reduces the effects of the near-shadowing, which results in a weakening of the tail in the power diagrams. The measured data is of course 3D and as a result the tail is mostly absent, too.

Both the simulated and measured HH diagrams exhibit a right-hand tail. These tails are caused by the spiking events, which possess high, i.e. higher than Bragg, cross-sections. This becomes clear when studying figure 7.4, which gives the same results as figure 7.3 after exclusion of the spikes. In the model data, the positions of the spikes are known and as a result they can be removed precisely. In the case of the measurements, the spikes were first detected and then removed. This process is less precise and some spikes may have been missed. Still, many if not most spikes were thus removed from the data results. When comparing the HH results of this figure with those of the full data and model sets, it is clear that the right-hand tails have become much smaller. This indicates that the spikes are indeed responsible for the tail.

The right-hand tail is (nearly) absent in both VV diagrams. At VV the Bragg cross-section is much higher than at HH. The polarisation ratio of the spikes has a value around zero dB. Consequently, while the spikes stand out well at HH, at VV the Bragg dominates and few spikes are evident.

Finally, there is one additional difference between the simulated and the measured powers. The polarisation ratio in the measurements is approximately -10 dB, whereas the model results show clear evidence of a much lower polarisation ratio of approximately -30 dB. This observation will be discussed in more detail in section 7.6.

The velocity diagrams, the lower panels of figure 7.3, show a much better match between the simulated and the measured data. All four diagrams possess a right-hand tail. These tails are caused by the spikes, as is evidenced by figure 7.4, where the tails are much weaker. The shape of the distribution without the spikes is almost Gaussian. The mean of the distribution is equal to the sum of the velocity of the Bragg waves and the wind drift, as the current velocity of 0.75 m/s was subtracted prior to making the histograms. The variance of the distribution is defined by the orbital velocities of the large scale wavefield. The orbital velocities vary over the wavelength of the waves and as such cause a broadening of the velocity distribution. This could easily be verified in the models by subtracting the influence of the orbital velocities, which resulted in a very narrow distribution.

Table 7.2: Statistics of the full simulated and measured data

	Simulation			Measurement			Match	
quantity	μ	s^-	s^+	μ	s^-	s^+	χ^2	df.
P_{hh}	-54.00	11.89	7.22	-36.00	3.82	6.79	1.19	44
P_{vv}	-20.50	5.52	3.82	-24.00	4.67	3.82	1.34	23
v_{hh}	0.40	0.25	0.25	0.75	0.38	0.42	1.18	50
v_{vv}	0.45	0.25	0.21	0.45	0.25	0.25	0.06	50

7.4 Statistical comparison

In the previous section a global comparison on the basis of range-time diagrams and histograms was made. In this section the match between the simulations and measurements is determined statistically.

To thoroughly analyse the match between the distributions of the simulated and the measured data, the following analysis was performed. Firstly, since the distributions are mostly asymmetric after transformation to logarithmic (dB) scale, the mean, μ, was determined by finding the position of the maximum of the distribution. For a purely Gaussian distribution this position is equal to the mean. Secondly, the standard deviation was calculated by determining the half-height width and dividing it by log(2). Again, for a Gaussian distribution this corresponds to the standard deviation. Given the asymmetry of the distribution, this parameter was determined for the left-hand side, s^-, and the right-hand side, s^+, separately.

To determine the match between the simulated and the measured data, a χ^2 goodness-of-fit analysis, see e.g. [35], was performed on the distributions for each of the quantities. Because of the tails in the power diagrams only a right-sided match was determined. Prior to the fit the measured and simulated data diagrams were matched in peak position and height of the distribution. This was necessary because the measured power was not calibrated absolutely, which results in an arbitrary value of the mean. Moreover, the low-power tails in the simulations cause a difference in the heights of the peaks. For the velocity diagrams, this mismatch is not expected and visually the histograms show a better match between the simulation and measurement results. Therefore, for the velocity diagrams the matching of the peak positions and heights was not done.

The results of these analyses for the full data sets are presented in table 7.2 and for the histograms without the spikes in table 7.3. Comparing the s^- and s^+ for the simulated powers illustrates the strong tail: the left-hand tails of the simulations differ from those of the measurements. On the other hand, the right-hand tails are similar. This is reflected in χ^2: all right-side fits for the power show a match between the measured and the simulated data with a confidence level over 99%.

Table 7.3: Statistics of the full simulated and measured data without spikes

	Simulation			Measurement			Match	
quantity	μ	s^-	s^+	μ	s^-	s^+	χ^2	no.
P_{hh}	-54.00	11.89	6.79	-36.50	3.40	5.10	1.47	41
P_{vv}	-20.50	5.52	3.82	-25.00	3.82	4.25	1.37	23
v_{hh}	0.40	0.25	0.25	0.65	0.34	0.38	0.72	44
v_{vv}	0.45	0.25	0.21	0.45	0.25	0.21	0.12	20

The velocity diagrams are more symmetric, which is reflected in the closer match between s^- and s^+. In general the HH polarisation has a higher velocity than the VV polarisation. For the full data this is due to the stronger influence of the spikes. As explained above, the method of removing the spikes may have left some of the signature of the spikes, which in turn might have raised the velocity somewhat. Also, especially for the measured data, the HH distribution is broader than the VV distribution.

The χ^2 fit again had a confidence level over 99% for both polarisations. In fact the fit in Doppler velocity is better than in power, despite the fact that no matching of the peak was performed prior to the fit. This again suggest that velocity is a better indicator of the underlying physics than the power and the polarisation ratio. This will be illustrated further in the next section.

7.5 Spikes

In this section the comparison of the spiking events is treated. In the model they were generated by first calculating where on the surface breaking waves could occur and what their wavelengths would be. The wavelength was used to scale the breaker profiles, which were, subsequently, evaluated with the MoM code of chapter 4. Their intrinsic velocities are then defined by their wavelength. In this section, firstly the range-time properties of one of these modelled spikes are compared with those of one of the spikes from the data. Secondly, the statistical properties of the entire population of spikes from the model are compared to those from the data.

7.5.1 Dynamic properties of spiking events

Figure 7.5 presents the dynamic properties of a spike for the simulation, panels on the left, and the data, panels on the right. The two upper panels show the power, RCS, of the spike for HH (solid line) and VV (dotted line) polarisations. The two lower panels present the Doppler velocity at HH polarisation.

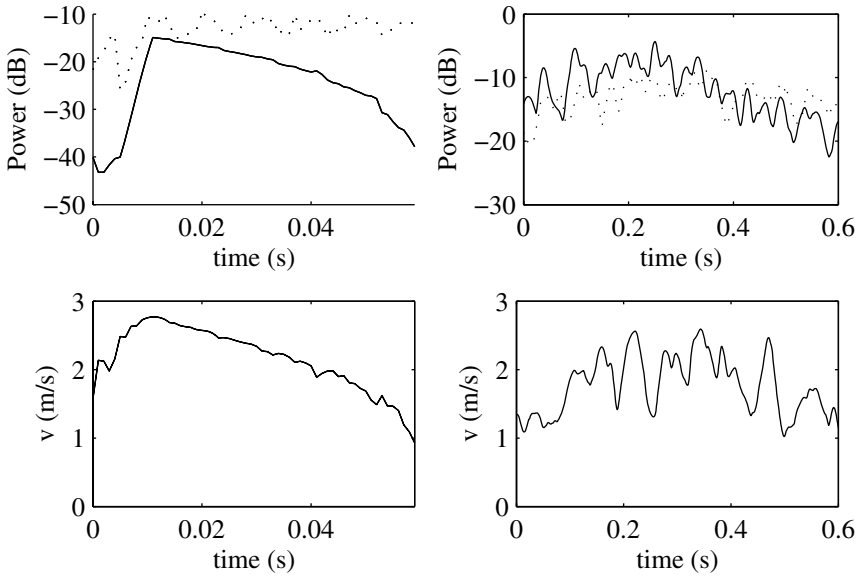

Figure 7.5: The dynamics of spikes: The panels on the left are for the simulation and the ones on the right for the measurements. The upper two panels present power at HH and VV polarisation and the lower panels the Doppler velocity at HH polarisation.

Comparing the two panels for the power, it can be observed that the HH results show a similar behaviour for both the model and the data. The event is characterised by a sudden sharp increase to a maximum, which is 10 to 20 dB higher than the background. Matching the model RCS to the corresponding breaker profiles, it could be derived that this maximum roughly coincides with the breaking stage, where the front face of the breaker first becomes vertical. The jet-formation stage retains a high, but variable, power, which is on average equal to the first peak. The model result is obviously smoother than the data, but the data roughly shows the same behaviour. After the final peak, the power slowly fades away to the background level.

The power at VV, however, behaves differently. The model results show that the spike power is almost completely lower than that of the Bragg background. There seems to be a slight heightening of the power level at the onset of the breaking event, but this is not very clear. In the measured data it can be observed that the spike is also much weaker than for HH, but it does exceed the background. It is not completely clear what processes govern this behaviour. Possibly, an explanation can be found in the unknown third dimension of the breaker. As explained in chapter

Table 7.4: Statistics of the spikes for the simulated and measured data

	Simulation			Measurement			Match	
quantity	μ	s^-	s^+	μ	s^-	s^+	χ^2	df.
v_{hh}	1.40	0.08	0.17	1.30	0.25	0.25	0.77	14
λ	1.30	0.17	0.17	1.00	0.34	0.51	0.76	14

5, the crest-length of a breaker is unknown. As a result the true three-dimensional RCS of such an event cannot be derived. This could mean that the RCS of the larger events might be underestimated by the presented methodology. This in turn would mean that the event can more easily exceed the background, even at VV.

The velocity diagrams are both for HH polarisation. Studying the diagrams it can be seen that the velocity roughly follows the power. The physical explanation for this is that the Bragg velocity is roughly equal to the phase velocity of the Bragg scatterers, i.e. 25 cm/s. The spikes should have a velocity equal to the phase velocity of the corresponding breaker, which can be much higher, even a few m/s. The resulting measured velocity is the weighed velocity of both these components. This means that as the power of a spike increases so does the contribution of its velocity. As a result, the velocity increases with the increase in power.

7.5.2 Statistics of the spiking events

Figure 7.6 gives the statistical results for the spikes of the data and the model. The panels on the left again present the model results, while those on the right give the corresponding data results. The results are the velocity distribution at HH and the corresponding wavelength distribution. The wavelengths were derived from the velocity through the phase velocity relation:

$$v_{ph} = \frac{\omega}{k} = \sqrt{\frac{g\lambda}{2\pi} + \frac{2\pi\gamma}{\lambda}}, \tag{7.1}$$

where ω is the frequency, k the wavenumber and λ the wavelength of the wave, g the gravitational acceleration and γ a surface tension parameter. See chapter 2 for the values of these constants. This is a quadratic equation in λ, which in general has two solutions, one in the capillary regime and one in the gravity-wave regime. Obviously, the latter is the desired solution. Table 7.4 gives the statistical results for these histograms.

For the velocity diagram HH polarisation was used. At this polarisation less influence from the Bragg background can be expected, which means that the velocity gives a better measure of the spike velocity. The presented velocities were also corrected for the current. However, since the spikes are all larger waves, they less

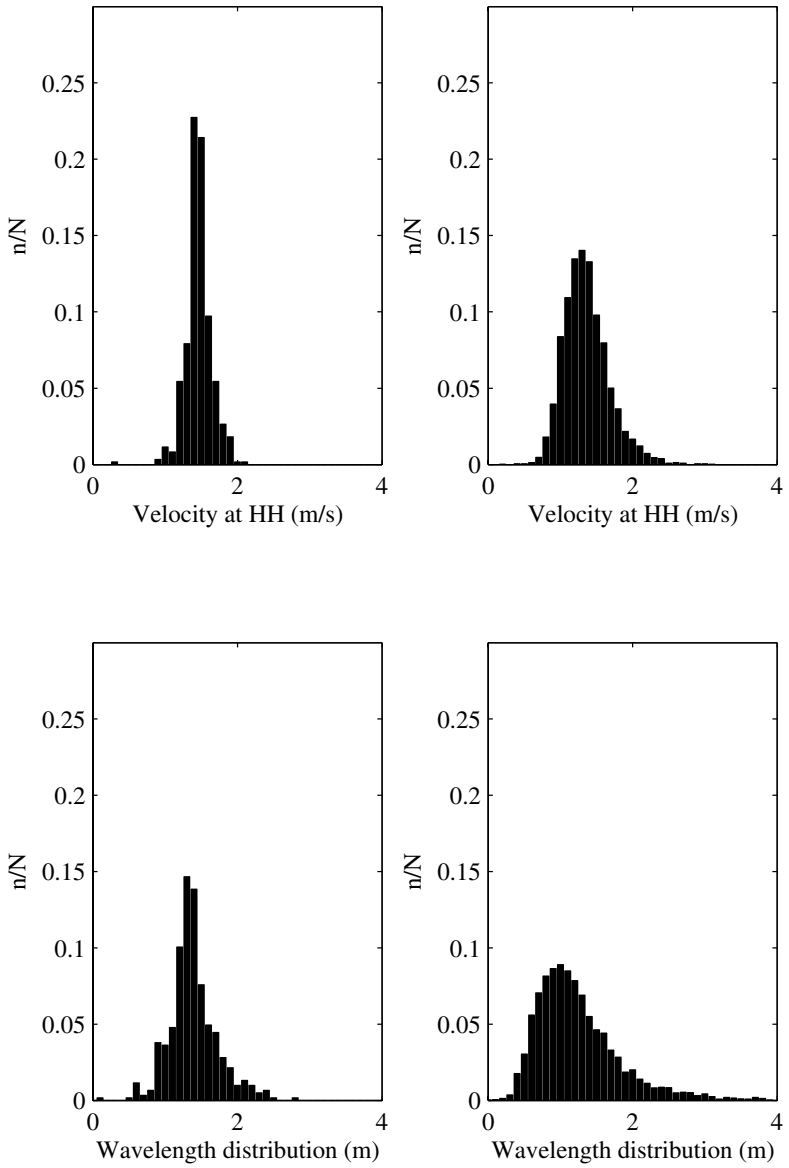

Figure 7.6: Histograms of the velocity and the wavelength of the spikes. The panels on the left show the model results, while the panels on the right present the data results. The upper two panels shows histograms of the velocity for HH polarisation. The lower two panels present the wavelength distributions as determined from the velocity distributions.

influenced by the wind drift. Hence, in the model the wind drift is not added to the spikes, even though it is added for the Bragg background. Comparing the model and the data results, a reasonable match in velocity is found. The shape of the histogram of the simulated data is reasonably close to that of the measured data. The match is even better in the wavelength distributions that could be inferred from the velocity distributions. The simulated data peaks at a somewhat higher value than the measured data, but the match is otherwise good. This is supported by the fact that the χ^2 fit gives a match with a probability of more than 99%.

Therefore, the model simulates the distribution of the spikes reasonably well. Only the average wavelength of the corresponding breakers is somewhat higher. This also explains the fact that the spike density for the simulations is somewhat lower than for the measurements. The larger spikes take up more space, which reduces their density. The reasons for the mismatch in average wavelength between the simulations and the measurements are not clear, but they may be related to bottom topography, which was not modelled.

7.6 Polarisation ratio and microbreakers

In the previous sections it was shown that although the simulated data exhibits a good match with the measured data for most properties, the polarisation ratio of the model is much lower than that of the data. The average polarisation ratio of the simulated data is -30 dB, while for the measured data it is -10 dB. In this section a number of possible explanations are proposed and one of those is expanded upon. A number of processes, which might raise the polarisation ratio, are not included in the model. They are discussed here and the most probable explanation is developed in more detail.

7.6.1 Hypotheses concerning the polarisation ratio difference

Five processes that might explain the difference in polarisation ratio are explored here:

- Bound capillary waves: These are waves that are bound to the longer underlying waves. The density of such waves is unclear and, therefore, they are not taken into account. Due to the fact that they are capillary waves, their resulting power and polarisation signature will be approximately equal to that of the normal Bragg background. Their velocity will be higher than that of the background and they, therefore, have sometimes been proposed as possible spiking candidates. Their low polarisation ratio, however, excludes them as a candidate both for raising the polarisation ratio and for causing the spikes.

- Whitecaps: These are the result of the larger breaking waves, that break visibly and result in the distinctive whitecap. They mainly consist of foam and a turbulent region, which often contains bound capillary waves. As far as I know, active imaging of foam has not been researched in detail, if at all and there are definitely no models of radar scattering on foam. As a result, it has not been included in the model. In my opinion it cannot be the explanation for the high polarisation ratio for two reasons. Firstly, it is relatively scarce, accompanying only the largest breakers and, therefore, cannot cause enough scattered power to significantly raise the polarisation ratio of the entire set. Secondly, the foam is relatively localised. It coincides with the larger breakers and as such does not occur on the entire surface. The enhanced polarisation ratio, however, does occur in the entire data set.

- Propagation effects: These are all kinds of effects, other than a straight-line propagation. They include effects such as refraction, ducting, multiple reflection and creeping waves. These effects are indeed capable of enhancing the radiation to and from the surface. Moreover, they are likely to occur for the entire surface. However, even though they enhance the radiation, the dominant scattering mechanism will still be Bragg scattering. Therefore, the polarisation ratio associated with these processes would still be around -30 dB.

- Incidence angle: As mentioned in section 7.2, there is some uncertainty about the precise incidence angle of the observations. At smaller incidence angles, Bragg scattering has a higher polarisation ratio than the model results shown in this chapter. However, only for incidence angles lower than 50° does Bragg scattering result in a polarisation ratio of -10 dB or higher. The uncertainty in incidence angle is only about 1 to 2 degrees, which means that the incidence angle of the measured data must be higher than 80°. For such high incidence angles Bragg scattering results in a polarisation ratio that is much lower than the observed -10 dB, which excludes the uncertainty in the incidence angle as a candidate.

- Microbreakers: As shown in the previous section, breakers occur over a wide range of wavelengths, mostly between 0.5 m and 3.0 m. However, it is safe to assume that significant numbers of breakers with a shorter wavelength exist. This has also been shown in a number of publications, [17, 29, 30]. In those articles evidence was presented that many very small breaking events with wavelengths of a few cm to a few dm occur. As these events are smaller than the resolution cell of the data, they cannot be distinguished from the Bragg background. They are also characterised by the fact that they do not break visibly. The water surface itself is hardly broken and as a result a whitecap is not formed, which means that they are also hard to detect visibly. They are, however, expected to contribute to the scattered radar power.

To test this hypothesis, the MoM code was used to evaluate the scattering from a number of small breaking waves with $\lambda \leq 50$ cm. The results showed that these events can indeed cause significant scattering, of the order of the Bragg scattered power. Moreover, since the scattering on such objects is specular, the maximum polarisation ratio will lie around 0 dB, a fact which was confirmed by the MoM code. This means that such objects are capable of raising the observed polarisation ratio. Furthermore, according to [17] they may occur everywhere on the surface. This means that the RCS of the entire surface is influenced by them. Finally, due to the fact that their wavelengths are fairly short, their corresponding radial velocity will also be low, typically of the order of 0.1 to 0.2 m/s. This means that they will not significantly raise the measured (Doppler) velocity.

The main problem with this hypothesis, however, is that little is known about microbreakers and, therefore, it cannot be stated with certainty that they cause the observed increase in polarisation ratio.

Recapitulating, a number of processes have been suggested that might raise the observed polarisation ratio. The best candidate is a significant population of micro-breakers, i.e. breakers with a wavelength of a few cm to a few dm. These events might indeed be capable of raising the polarisation ratio, while not unduly influencing the other observed properties. In the next subsection a simulation of the seaclutter with these microbreakers included is presented.

7.6.2 Modelling microbreakers

In the previous subsection the hypothesis was proposed that the increased polarisation ratios observed in the data, was caused by so-called microbreakers. In this subsection this assumption is used as a starting point and a simulation is made of seaclutter, including the effects of such events.

The most important assumption is that the events should have a polarisation ratio around 0 dB, similar to their larger counterparts. In appendix B it is shown that this assumption combined with the desired increase in polarisation ratio of 20 dB means that the microbreakers should possess a combined scattering amplitude $A^{m.b.}$ of:

$$A_{HH}^{m.b.} = A_{VV}^{m.b.} = \frac{9}{10}(\sqrt{(10)} - 1)^{-1} A_{VV}^{\mathrm{B}} \approx 0.416 A_{VV}^{\mathrm{B}}, \tag{7.2}$$

where $A_{VV}^{\mathrm{B}} = \sqrt{\sigma^{\mathrm{B}}}$ is the amplitude of the tilt-modulated Bragg scattering at VV polarisation.

As the average number of micro-breakers per resolution cell is unknown the model uses a statistical approach. To each illuminated cell in the simulation a microbreaker power is added, whose value is drawn from a random Gaussian distributed

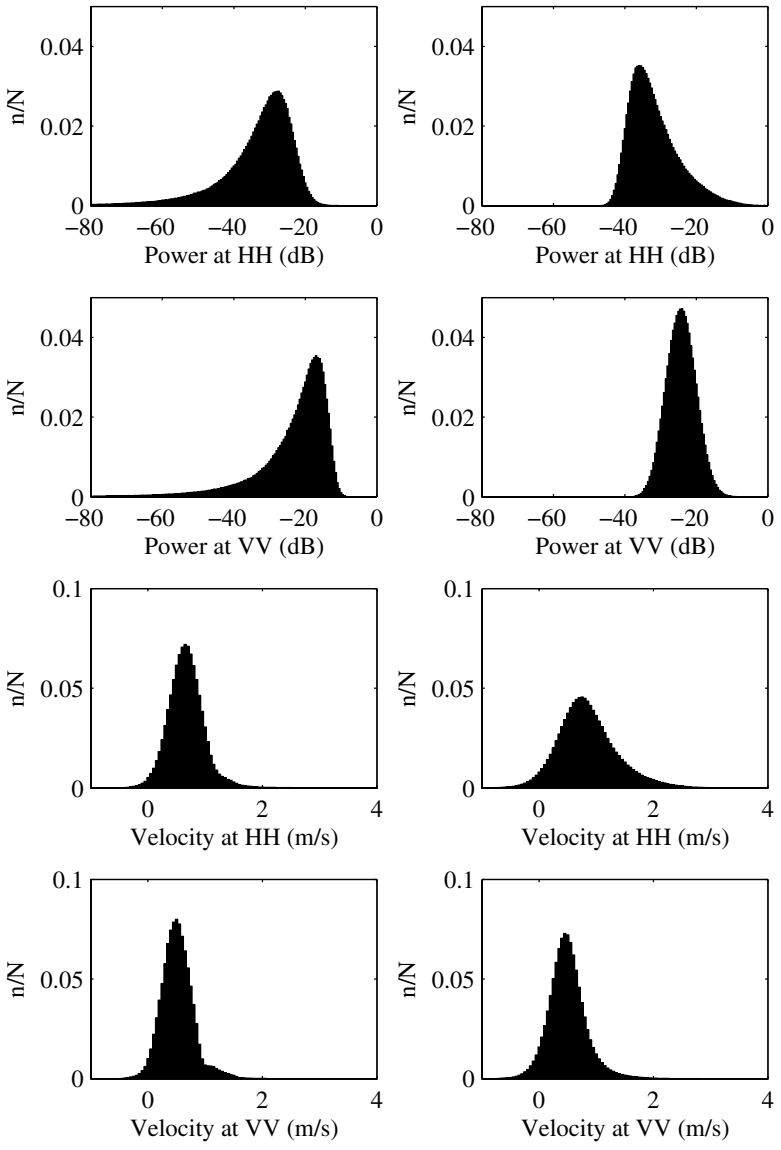

Figure 7.7: Histograms of power and velocity, including micro-breakers. The panels on the left show the model results, while the panels on the right present the data results. The upper two panels shows histograms of the power in dB scale for HH and VV polarisation, respectively. The lower two panels present the velocity distributions for both polarisation.

Table 7.5: Statistics of the full simulated and measured data with the inclusion of microbreakers

	Simulation			Measurement			Match	
quantity	μ	s^-	s^+	μ	s^-	s^+	χ^2	no.
P_{hh}	-27.50	8.07	4.25	-36.00	3.82	6.79	3.68	26
P_{vv}	-17.00	6.37	3.40	-24.00	4.67	3.82	1.40	21
v_{hh}	0.65	0.25	0.25	0.75	0.38	0.42	5.03	66
v_{vv}	0.50	0.25	0.25	0.45	0.25	0.25	0.26	20

set with $P_{HH}^{m.b.}$ as its mean. As the power distribution of the data exhibits a Gaussian shape in dB scale, the Gaussian of the microbreakers also uses a dB scale, with a variance of 3 dB. The velocity of the events was derived by assuming the collection of microbreakers is normally distributed around a wavelength of half a resolution cell, i.e. 25 cm, with a variance of 10 cm. This means that most (99%) of the microbreakers will be smaller than the resolution cell of 50 cm. From this Gaussian distributed set of wavelengths the velocity can be calculated through equation 7.1.

Figure 7.7 presents the results of this simulation and in table 7.5 the statistical results are given. The figure uses the same lay-out as figures 7.3 and 7.4. Comparing these results to the earlier results for the full set in figure 7.3, it can be concluded that most properties are roughly equal to those of the original results. Only now the difference in power between HH and VV for the model is roughly -10 dB. The shapes of the HH and VV power distributions of the model still exhibit the left-hand tail. The HH distribution retains the right-hand tail and it is slightly broader than the VV distribution. Also the shapes of the velocity diagrams roughly stay the same. The main difference is that the microbreakers seem to fill the gap between the Bragg and the spikes. This makes the match of the data and the models in velocity even better than before. This is further supported by the statistical results, which exhibit χ^2 values that are lower than those for the full model.

In all it can be concluded that the addition of microbreakers in the model seems to improve the match between the simulated (model) data and the observed data. This means that it may well be the desired solution for the polarisation ratio offset.

7.7 Conclusions

In this chapter a comparison was made between the results of the model, presented in chapter 5, and the observed data of chapter 6.

The comparison was made, firstly through range-time diagrams and secondly, in a statistical manner through histograms of the relevant properties. The range-time diagrams showed a reasonably good match between the model and the data. The

main difference was that the model results exhibited significant shadowing, which was much weaker in the data. This difference is caused by the width of the resolution cell in combination with the directional spread of the ocean wave spectrum. This results in a partial illumination of the otherwise shadowed cells, which plays an important role in the data, but which was not modelled.

The statistical analysis showed that the power diagrams exhibit a number of differences between the model and the data, mainly through a significant low-power tail and the lower polarisation ratio. The tail is caused by the fact that at low grazing angles the Bragg scattering has a very high dynamic range in power. In the data this feature is missing for the same reason that the shadowing is almost absent. The velocity diagrams exhibited a much better match, which is due to the fact that the Bragg scatterers all have similar velocities at the low grazing angles under consideration.

One significant difference between the data and the model was also observed. The polarisation ratio of the model was 20 dB lower than the polarisation ratio of the observed data. A number of physical processes were suggested that might cause this difference and it was found that microbreakers are the most probable explanation. A model of the microbreakers was presented and it was shown that they indeed improved the match between the model and the data.

The fact that the match between the model and the data was better in velocity than in power or polarisation suggests that velocity is the best indicator of the physical processes that cause the radar seaclutter.

Chapter 8

Summary, conclusions and recommendations

8.1 Summary

The three main goals of this thesis, stated in chapter 1, are used in this section as a framework for summarising this work. The first goal was:

1. Identify the gaps in knowledge of seaclutter through a literature study.

This goal was accomplished in section 1.2, which gave an overview of the entire field of radar seaclutter research and identified the most important hiati: 1) There are many models of tilt-modulated Bragg scattering and of the so-called sea spikes, but few models combine both these two components. 2) There are few, if any, dynamic models of radar seaclutter.

Chapter 2 treated both basic wave theory and spectral theory. The Romeiser-Alpers-Wisman spectrum, which is used in this thesis, was presented. Moreover, wave breaking was discussed, which illustrated the lack of a good link between the linear wave field and the breaking waves through a wave breaking criterion. Finally, the breaking wave profiles used in this thesis were presented.

Chapter 3 treated electromagnetic theory with a focus on the scattering of electromagnetic waves on (PEC) surfaces. Different techniques were discussed and it was shown that only full-wave methods are capable of fully evaluating the scattering on breaking waves.

The two hiati mentioned above allowed the definition of the second goal:

2a. The model must be a combination of composite surface theory, i.e. tilt modulated Bragg scattering, and sea spike theory, i.e. semi-specular scattering on breaking waves.

2b. The model must be dynamic.

To reach these goals a number of models were implemented and combined, which was described in chapters 4 and 5.

Chapter 4 presents a full-wave model for the evaluation of breaking wave profiles. First, the relevant electric field (EFIE) and magnetic (MFIE) field integral equations were defined, because they were needed to evaluate horizontally as well as vertically polarised radiation. The equations were then solved using the Method of Moments (MoM). The so-obtained method is capable of treating scattering on a wide range of objects. It was validated on a number of flat plates and cylinders of different sizes and then used for evaluating breaking wave profiles, as a part of the larger model.

In chapter 5 the combined model was treated, which consisted of six parts:

i. Spectral surface generation

ii. Breaking wave generation

iii. Surface evaluation

iv. Bragg calculation

v. Spike calculation

vi. RCS combination

These six steps generate one time step of the seaclutter simulation. By repeating this procedure, a time series of any desired length may be generated. The model combines tilt-modulated Bragg scattering and sea spikes, and is also dynamic, which means that it satisfies the demands stated in goal 2.

The third main goal of this thesis was:

3. Validate the model through a comparison with radar seaclutter data.

The data analysis required for this purpose was described in chapter 6 and also in [61]. Three sets of high resolution, coherent and polarimetric X-band radar data were analysed in a number of ways. The analysis of the data revealed that seaclutter is made up of 1) a global background caused by tilt-modulated Bragg scattering, and 2) so-called sea-spikes, caused by the semi-specular scattering on steepened

and/or breaking waves. Moreover, it was found that velocity is the best tool for the physical interpretation of the data.

The process of fine-tuning and validating the model was performed in chapter 7. The fine-tuning comprised of two main parts: spectral matching and tuning of the breaking criterion. Having fine-tuned the oceanographic part of the model, a simulated data set was obtained, which had the same form of the measured data. Therefore, the same analyses that had been performed on the measured data were also applied to the simulated data. It was found that the model results closely matched the measured data results. The main difference between the model and the measurement was a direct result of the 1D nature of the model. This match was further validated by a thorough statistical comparison of both sets of data.

8.2 Conclusions

From the results of the research reported in this thesis, the following conclusions can be drawn:

1. The model, presented in chapters 4, 5 and 7, simulates one dimensional low grazing angle radar seaclutter with a good accuracy.

2. The global background can be linked with tilt-modulated Bragg scattering. The spikes are well-modelled by the scattering on steepened and/or breaking waves.

3. Combining both physical processes mentioned in point 2 into one model was instrumental in the improvement of radar seaclutter models.

4. Velocity is the best quantity for physically interpreting radar seaclutter data. It is therefore advisable to include it in seaclutter models.

8.3 Recommendations for future research

During this research additional points of interest were identified, which might provide promising avenues for future research.

Firstly, the model presented in this thesis is one-dimensional. Extending the model to two dimensions would further improve understanding of this field of research. It would enable the modelling of the directional spread of the wave field, which could improve understanding of the shadowing as observed in the data and discussed in appendix C. Moreover, the 2D modelling of breaking waves and the scattering thereon is a relatively unexplored field of research. Some efforts along

these lines were made during this PhD research, see [58], where it was shown that this approach also gives information about the directional properties of spikes.

Secondly, one of the processes that has been proposed as the cause of the heightened background polarisation ratio is scattering on microbreakers. These are very small breaking waves, i.e. small enough to not cause whitecapping. This explains why they have not been visually associated with spikes. Nonetheless, given the fact that the larger breakers cause sea spikes, these smaller events can be expected to have a significant influence on the radar signature.

A final interesting avenue of future research is the extension of a full-wave method to incorporate velocity. As mentioned in the conclusions, velocity is the most important measurable quantity for physically interpreting seaclutter data. Therefore, velocities that have been determined with a full-wave method could significantly improve our understanding of the dynamic evolution of sea spikes.

Appendix A

Mathematics

A.1 Green′s function

An essential part in performing E.M. scattering calculations is the determining the relevant Green′s function. In this thesis we are mainly interested in the 3- and 2-dimensional Green′s functions for the Helmholtz equation. The full derivation is long and complicated and it falls outside the scope of this thesis. For a full treatment of this topic we refer to textbooks, such as [20]. Here a shortened derivation is given.

To find the desired Green′s functions, four steps are taken. Firstly, the 3-dimensional formulation for the wave equation is derived, which is integrated to find the 2D result for the wave equation. These results are then used to find the 3- and 2-dimensional Green′s functions for the Helmholtz equation.

A.1.1 Green′s function for the wave equation

Assume time-harmonic fields and let the corresponding Green′s function be, $G(\mathbf{r}, \mathbf{r}', t, t')$. This function must satisfy the wave equation,

$$(\nabla^2 - c^{-2}\frac{\partial^2}{\partial t^2})G(\mathbf{r}, \mathbf{r}', t, t') = -\delta(\mathbf{r} - \mathbf{r}'). \tag{A.1}$$

Define four dimensional coordinates:

$$x = (\mathbf{r}, x_0), \quad x_0 = ct, \tag{A.2}$$

and the corresponding spatial and temporal frequencies,

$$k = (\mathbf{k}, k_0), \quad k_0 = \frac{\omega}{c}. \tag{A.3}$$

Then introduce the 4D Fourier transform of the Green′s function,

$$G(x) = (2\pi)^{-4} \int\int\int\int e^{ik\cdot x}\tilde{G}(k)d^4k. \tag{A.4}$$

Applying this to the wave equation gives,

$$(\nabla^2 - c^{-2}\frac{\partial^2}{\partial t^2})G(x) = (2\pi)^{-4} \int\int\int\int (-\mathbf{k}^2 + k_0^2)e^{ik\cdot x}\tilde{G}(k)d^4k. \tag{A.5}$$

Now choose

$$\tilde{G}(k) = (\mathbf{k}^2 - k_0^2)^{-1}, \tag{A.6}$$

so that

$$(\nabla^2 - c^{-2}\frac{\partial^2}{\partial t^2})G(x) = (2\pi)^{-4} \int\int\int\int e^{ik\cdot x}d^4k. \tag{A.7}$$

This means that the Green′s function becomes,

$$G(x) = -(2\pi)^{-4} \int\int\int\int \frac{e^{ik\cdot x}}{k_0^2 - |k|^2}d^4k. \tag{A.8}$$

Solving this quadruple integral is a complicated process requiring integration along a complex contour, using Cauchy's theorem of residues and Jordan's Lemma. For the full derivation we refer to [20]. The result is given by,

$$G(x) = \frac{\delta(x_0 + r)}{4\pi r}. \tag{A.9}$$

Equation A.9 is translationally invariant so that we may write equation A.9 as,

$$G(\mathbf{r}, \mathbf{r}', t, t') = \frac{\delta(x_0 - x_0' + |r - r'|)}{4\pi|r - r'|}. \tag{A.10}$$

A.1.2 Green′s function for the wave equation in two dimensions

For the two-dimensional case it is assumed that the z-direction is the invariant. It is then convenient to introduce the following notations:

$$\mathbf{r} - \mathbf{r}' = \sqrt{P^2 + (z - z')}, \tag{A.11}$$

where

$$P = \rho - \rho', \qquad \rho = (x, y). \tag{A.12}$$

Also let $\tau = x_0 - x_0'$. The two dimensional Green′s function may now be determined by integrating equation A.10 in the z-direction,

$$G_{2D}(P, \tau) = \int_{-\infty}^{\infty} \frac{\delta(\tau + |r - r'|)}{4\pi|r - r'|}dz'. \tag{A.13}$$

This integral is easily solved by evaluating the δ-function, giving,

$$G_{2D}(P,\tau) = \frac{1}{2\pi\sqrt{\tau^2 - P^2}}. \tag{A.14}$$

A.1.3 Green′s function for the Helmholtz equation

In the previous subsections the 3- and 2-dimensional Green′s functions for the wave equation were obtained. However, especially for use in chapter 4, the Green′s function is needed, which satisfies the Helmholtz equation,

$$(\nabla^2 + k_0^2)G(\mathbf{r},\mathbf{r}',k_0) = -\delta(\mathbf{r}-\mathbf{r}'). \tag{A.15}$$

This equation is obtained when a temporal Fourier transform is applied to equation A.1. The Green′s function, $G(\mathbf{r},\mathbf{r}',k_0)$, which satisfies the Helmholtz equation is then obtained by applying the same temporal Fourier transform to the Green′s function for the wave equation,

$$G(\mathbf{r},\mathbf{r}',k_0) = \int_{-\infty}^{\infty} G(\mathbf{r},\mathbf{r}',t,t')\exp(ik_0\tau)d\tau. \tag{A.16}$$

Thus, substituting from equation A.10 and evaluating the δ-function, we obtain the classical formulation for the 3-dimensional Green′s function,

$$\begin{aligned} G(\mathbf{r},\mathbf{r}',k_0) &= \frac{e^{-jk_0R}}{R}, \\ \text{with } R &= |\mathbf{r}-\mathbf{r}'|. \end{aligned} \tag{A.17}$$

A.1.4 Green′s function for the Helmholtz equation in two dimensions

Similar to the three dimensional case of the previous section, the two-dimensional Green′s function for the Helmholtz equation is obtained by the temporal Fourier transform:

$$G_{2D}(P,k_0) = \int_{-\infty}^{\infty} G_{2D}(P,\tau)\exp(ik_0\tau)d\tau. \tag{A.18}$$

Introduce ψ according to,

$$\tau = P\cosh\psi, \qquad d\tau = P\sinh\psi d\psi. \tag{A.19}$$

Adopting ψ and substituting equation A.14 into equation A.18 gives,

$$G_{2D}(P,k_0) = -\frac{1}{4\pi}\int_{-\infty}^{\infty} e^{ik_0P\cosh\psi}d\psi. \tag{A.20}$$

This equation is an integral representation of the Hankel function, so that we finally obtain the well-known result,

$$G_{2D}(P, k_0) = -\frac{i}{4} H_0^{(2)}(k_0 P). \tag{A.21}$$

This is the form that will be used extensively in chapter 4.

A.2 Hankel functions

In this section the Hankel function is treated. Firstly, the general definitions of the Hankel functions are given. Secondly, series expansions of these functions are given and finally some recurrence relation. The material in this section was mainly taken from [1], chapter 9. Throughout this appendix we will refer to the relevant formulae as A&Sno, with no the relevant formula number from [1].

A.2.1 General definition

The Hankel functions, $H_\nu^{(1)}(z)$ and $H_\nu^{(2)}(z)$, are Bessel functions of the third kind, which means they are solutions of the differential equation (A&S9.1.1),

$$z^2 \frac{d^2 w}{dz^2} + z \frac{dw}{dz} + \left(z^2 - v^2\right) w = 0. \tag{A.22}$$

The more common solutions of this equation are the Bessel functions of the first kind, $J_\nu(z)$ and of the second kind, $Y_\nu(z)$. The Bessel functions are related in the following manner (A&S9.1.2-4):

$$\begin{aligned} H_\nu^{(1)}(z) &= J_\nu(z) + iY_\nu(z), \\ H_\nu^{(2)}(z) &= J_\nu(z) - iY_\nu(z). \end{aligned} \tag{A.23}$$

A.2.2 Series expansion

The $J_n(z)$ and $Y_n(z)$ may be written as ascending series according to (A&S9.1.10-11):

$$\begin{aligned} J_n(z) &= \left(\frac{z}{2}\right)^n \sum_{k=0}^{\infty} \frac{\left(-\frac{1}{4}z^2\right)^k}{k!(n+k)!}, \\ Y_n(z) &= -\frac{\left(\frac{1}{2}z\right)^{-n}}{\pi} \sum_{k=0}^{n-1} \frac{(n-k-1)!}{k!} \left(\frac{1}{4}z^2\right)^k + \frac{2}{\pi} \ln\left(\frac{z}{2}\right) J_n(z) \end{aligned}$$

$$-\frac{\left(\frac{1}{2}z\right)^n}{\pi}\sum_{k=0}^{\infty}\left\{\psi(k+1)+\psi(n+k+1)\right\}\frac{\left(-\frac{1}{4}z^2\right)^k}{k!(n+k)!}. \qquad \text{(A.24)}$$

Here $\psi(n)$ is defined according to A&S6.3.2:

$$\psi(1)=-\gamma, \qquad \psi(n)=-\gamma+\sum_{k=1}^{n-1}k^{-1}$$
$$\gamma=0.5772156649 \qquad \text{(A.25)}$$

Substituting equations A.24 and A.24 into equation A.23 gives the following series for the $H_n^{(2)}(z)$:

$$\begin{aligned} H_n^{(2)}(z) &= i\frac{\left(\frac{1}{2}z\right)^{-n}}{\pi}\sum_{k=0}^{n-1}\frac{(n-k-1)!}{k!}\left(\frac{1}{4}z^2\right)^k \\ &+\left\{1-\frac{2i}{\pi}\ln\left(\frac{z}{2}\right)\right\}\left(\frac{z}{2}\right)^n\sum_{k=0}^{\infty}\frac{\left(-\frac{1}{4}z^2\right)^k}{k!(n+k)!} \\ &+i\frac{\left(\frac{1}{2}z\right)^n}{\pi}\sum_{k=0}^{\infty}\left\{\psi(k+1)+\psi(n+k+1)\right\}\frac{\left(-\frac{1}{4}z^2\right)^k}{k!(n+k)!}. \end{aligned} \qquad \text{(A.26)}$$

The two Hankel functions of interest in this work are $H_0^{(2)}(z)$ and $H_2^{(2)}(z)$. For $H_0^{(2)}(z)$ the series reduces to:

$$H_0^{(2)}(z)=\frac{2i}{\pi}\sum_{k=0}^{\infty}\left\{\frac{\pi}{2i}+\psi(k+1)-\ln\left(\frac{z}{2}\right)\right\}\frac{\left(-\frac{1}{4}z^2\right)^k}{(k!)^2} \qquad \text{(A.27)}$$

and $H_2^{(2)}(z)$ reduces to:

$$\begin{aligned} H_2^{(2)}(z) &= \frac{4i}{\pi z^2}+\frac{i}{\pi} \qquad \text{(A.28)} \\ &+\frac{iz^2}{2\pi}\sum_{k=0}^{\infty}\left\{\frac{\pi}{i}-2\ln\left(\frac{z}{2}\right)+\psi(k+1)+\psi(k+3)\right\}\frac{\left(-\frac{1}{4}z^2\right)^k}{(k!)^2} \end{aligned}$$

A.3 Recurrence relations

The following recurrence relations are valid for J, Y, $H^{(1)}$ and $H^{(2)}$. They are denoted by $G_n(z)$ here, where n is the order, see A&S9.1.27-28:

$$G_{n-1}(z)+G_{n+1}(z) = \frac{2n}{z}G_n(z) \qquad \text{(A.29)}$$

$$G_{n-1}(z) - G_{n+1}(z) = 2G'_n(z) \tag{A.30}$$

$$G_{n-1}(z) - \frac{n}{z}G_n(z) = G'_n(z) \tag{A.31}$$

$$-G_{n+1}(z) + \frac{n}{z}G_n(z) = G'_n(z) \tag{A.32}$$

$$G'_0(z) = -G_1(z) \tag{A.33}$$

Appendix B

Derivation of equations 4.17 and 7.2

B.1 Derivation of equation 4.17

The problems to be solved are:

$$\left[\frac{\partial^2}{\partial x^2}+k^2\right]H_0^{(2)}(k\mathbf{R}) = \frac{k^2}{2}\left[H_0^{(2)}(k\mathbf{R})+H_2^{(2)}(k\mathbf{R})\cos(2\phi)\right] \quad \text{(B.1)}$$

$$\frac{\partial^2}{\partial x\partial y}H_0^{(2)}(k\mathbf{R}) = \frac{k^2}{2}H_2^{(2)}(k\mathbf{R})\sin(2\phi), \quad \text{(B.2)}$$

where

$$\mathbf{R}=|\rho-\mathbf{x}|=\sqrt{(x-x)^2+(y-y)^2}. \quad \text{(B.3)}$$

For convenience the $_{(2)}$ is implied in the following. Writing out the double derivatives gives:

$$\left[\frac{\partial^2}{\partial x^2}+k^2\right]H_0(k\mathbf{R}) = H_0''(k\mathbf{R})\left(\frac{\partial k\mathbf{R}}{\partial x}\right)^2+H_0'(k\mathbf{R})\frac{\partial^2 k\mathbf{R}}{\partial x^2} + k^2H_0(k\mathbf{R}) \quad \text{(B.4)}$$

$$\frac{\partial^2}{\partial x\partial y}H_0(k\mathbf{R}) = H_0''(k\mathbf{R})\frac{\partial k\mathbf{R}}{\partial x}\frac{\partial k\mathbf{R}}{\partial y}+H_0'(k\mathbf{R})\frac{\partial^2 k\mathbf{R}}{\partial x\partial y}, \quad \text{(B.5)}$$

where the primes denote derivatives of the Hankel functions to their argument.

Before going on, some relations need to be derived. From the geometry of figure 4.1 it follows that:

$$x-x' = \mathbf{R}\cos(\phi), \quad \text{(B.6)}$$

$$y - y' = \mathbf{R}\sin(\phi). \tag{B.7}$$

Using the recurrence relations from A.3 we can calculate $H_0'(k\mathbf{R})$ and $H_0''(k\mathbf{R})$:

$$H_0'(k\mathbf{R}) = -H_1(k\mathbf{R}) = \frac{z}{2}H_0(k\mathbf{R}) + \frac{z}{2}H_2(k\mathbf{R}) \tag{B.8}$$

$$H_0''(k\mathbf{R}) = -H_1'(k\mathbf{R}) = -\frac{1}{2}H_0(k\mathbf{R}) + \frac{1}{2}H_2(k\mathbf{R}) \tag{B.9}$$

Writing out the derivatives of $k\mathbf{R}$ and substituting equations B.6 and B.7 gives,

$$\frac{\partial k\mathbf{R}}{\partial x} = \frac{k(x-x')}{\sqrt{(x-x)^2+(y-y)^2}} = \frac{k(x-x')}{\mathbf{R}} = k\cos(\phi) \tag{B.10}$$

$$\frac{\partial k\mathbf{R}}{\partial y} = \frac{k(y-y')}{\sqrt{(x-x)^2+(y-y)^2}} = \frac{k(y-y')}{\mathbf{R}} = k\sin(\phi) \tag{B.11}$$

$$\begin{aligned}\frac{\partial^2 k\mathbf{R}}{\partial x^2} &= \frac{\partial}{\partial x}\left\{\frac{k(x-x')}{\mathbf{R}}\right\} = \frac{1}{\mathbf{R}^2}\left\{k\mathbf{R}k(x-x)\frac{\partial \mathbf{R}}{\partial x}\right\} \\ &= \frac{k}{\mathbf{R}} - \frac{k(x-x')^2}{\mathbf{R}^3} = \frac{k(1-\cos^2(\phi))}{\mathbf{R}}\end{aligned} \tag{B.12}$$

$$\begin{aligned}\frac{\partial^2 k\mathbf{R}}{\partial x \partial y} &= \frac{\partial}{\partial x}\left\{\frac{k(y-y')}{\mathbf{R}}\right\} = -\frac{k(x-x')(y-y')}{\mathbf{R}^3} \\ &= -\frac{k\sin(\phi)\cos(\phi)}{R} = -\frac{k\sin(2\phi)}{R}\end{aligned} \tag{B.13}$$

Substituting equations B.8, B.9, B.10 and B.12 into equation B.4 gives

$$\begin{aligned}\left[\frac{\partial^2}{\partial x^2} + k^2\right] H_0(k\mathbf{R}) &= -\frac{k^2}{2}\cos^2(\phi)\left\{H_0(k\mathbf{R}) - H_2(k\mathbf{R})\right\} \\ &- \frac{k^2\mathbf{R}(1-\cos^2(\phi))}{\mathbf{R}}\left\{H_0(k\mathbf{R}) + H_2(k\mathbf{R})\right\} + k^2 H_0(k\mathbf{R}) \\ &= \frac{k^2}{2}H_0(k\mathbf{R})\left\{-\cos^2(\phi) - 1 + \cos^2(\phi) + 2\right\} \\ &+ \frac{k^2}{2}H_2(k\mathbf{R})\left\{\cos^2(\phi) - 1 + \cos^2(\phi)\right\} \\ &= \frac{k^2}{2}H_0(k\mathbf{R}) + \frac{k^2}{2}H_0(k\mathbf{R})\left\{2\cos^2(\phi) - 1\right\} \\ &= \frac{k^2}{2}\left[H_0^{(2)}(k\mathbf{R}) + H_2^{(2)}(k\mathbf{R})\cos(2\phi)\right]\end{aligned}$$

Substituting equations B.8, B.9, B.11 and B.13 into equation B.5 gives

$$\frac{\partial^2}{\partial x \partial y}H_0(k\mathbf{R}) = -\frac{k^2}{2}\sin(\phi)\cos(\phi)\left\{H_0(k\mathbf{R}) - H_2(k\mathbf{R})\right\}$$

$$
\begin{aligned}
&+ \quad \frac{k^2\mathbf{R}\sin(2\phi))}{4\mathbf{R}}\left\{H_0(k\mathbf{R}) - H_2(k\mathbf{R})\right\} \\
&= \quad -\frac{k^2}{4}\sin(2\phi)\left\{H_0(k\mathbf{R}) - H_2(k\mathbf{R})\right\} \\
&+ \quad \frac{k^2}{4}\sin(2\phi)\left\{H_0(k\mathbf{R}) + H_2(k\mathbf{R})\right\} \\
&= \quad \frac{k^2}{2}\sin(2\phi)H_2(k\mathbf{R})
\end{aligned}
$$

This proves equation 4.17.

B.2 Derivation of equation 7.2

As explained in section 7.6 the premises of this derivation are as follows. The (Bragg) polarisation ratio is approximately -30dB, while the combined Bragg and microbreaker polarisation ratio is about -10 dB. Finally, the polarisation ratio of the microbreakers is 0 dB. From this it is possible to find the average amplitude, i.e. square root of the radar cross section, of the microbreakers compared to the average amplitude of the Bragg background. First a few definitions are needed. Let the amplitudes of the Bragg background at HH and VV polarisation be H and V respectively. Also, because the polarisation ratio of the microbreakers is 0 dB, the amplitudes of both polarisations are equal to say M. Then from the polarisation ratio of the Bragg background, PR_0, follows:

$$
\begin{aligned}
PR_0 &= 20^{10}\log\left(\frac{H}{V}\right) = -30 \rightarrow \\
\frac{H}{V} &= (10\sqrt{10})^{-1} \rightarrow \\
H &= (10\sqrt{10})^{-1}V, \qquad \text{(B.14)}
\end{aligned}
$$

and from the desired polarisation ratio, PR_1:

$$
\begin{aligned}
PR_1 &= 20^{10}\log\left(\frac{H+M}{V+M}\right) = -10 \rightarrow \\
\frac{H+M}{V+M} &= (\sqrt{10})^{-1} \rightarrow \\
H+M &= (\sqrt{10})^{-1}(V+M). \qquad \text{(B.15)}
\end{aligned}
$$

Substituting relation B.14 into equation B.15 gives:

$$(10\sqrt{10})^{-1}V + M = (\sqrt{10})^{-1}(V+M). \qquad \text{(B.16)}$$

Multiplying both sides by $\sqrt{10}$ and regrouping then gives:

$$\begin{aligned}
\sqrt{10}(10\sqrt{10})^{-1}V + \sqrt{10}M &= \sqrt{10}(\sqrt{10})^{-1}(V+M) \\
10^{-1}V + \sqrt{10}M &= V + M \\
(1-\sqrt{10})M &= (1-10^{-1})V \\
M &= \frac{9}{10}(1-\sqrt{10})^{-1}V, \qquad \text{(B.17)}
\end{aligned}$$

which is equal to equation 7.2.

Appendix C

Statistics of 1D versus 2D Composite surface models

In section 7.3 histograms of the scattered power for the simulated and measured data were presented. One difference between the simulations and the measurements was a strong left-hand (low power) tail in the former, which was absent in the latter. It was proposed that this difference is explained by the fact that the simulations are purely 1D, while the measurements are 2D. In this appendix it is shown that this proposal is indeed plausible.

The physical background for this explanation is as follows. According to composite surface theory the ocean surface can be described as a collection of slopes with a distribution dependent on the spectral composition of the surface. Given the global incidence angle of radiation scattering on this surface, the local incidence angle of the radiation will have a similar distribution with as a mean the global incidence angle. At low grazing angles Bragg scattering is asymptotically dependent on incidence angle. The distribution of powers for Bragg scattering on the surface at low grazing angles will therefore result in the characteristic, skewed distribution presented in section 7.3. For 2D surfaces, however, the finite width of the radar bundle means that the contributions of a number of slopes will be combined. Due to the asymptotic behaviour of Bragg scattering at LGA, the lowest local incidence angle will dominate the resolution cell. This means that the extremely low powers that occur for a 1D surface, in general will not occur for a 2D surface.

To illustrate this a simplified 2D seaclutter model was implemented. The spikes almost certainly do not cause the low power tail and as such were excluded from the 2D model. Therefore, taking the directional spread of the ocean spectrum into account, a number of timesteps of an evolving 2D stretch of surface were generated. This surface was then divided into a number of 1D 'rangelines'. For each of these

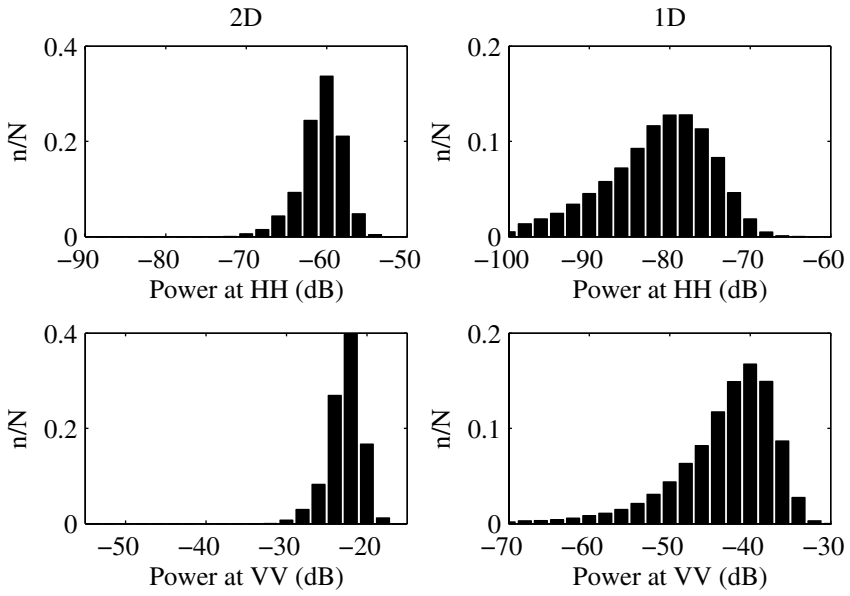

Figure C.1: Histogram of power at HH and VV polarisation for the 1D and 2D simulations.

lines the Bragg scattered power was determined with the 1D model presented in chapter 5. The 2D results were then obtained by coherently summing the rangelines to obtain one 2D timestep. The 1D results were obtained by taking the first rangeline from the 2D results. As mentioned, the surface was evolved for a large number of timesteps to obtain a good statistic.

The results of this simulation are presented in figure C.1. The panels on the left give the results for the 2D simulation for HH (upper panel) and VV (lower panel) polarisations and the panels on the right give the corresponding results for the 1D simulation. Studying the results it is obvious that for the 2D model the strong low power tail is nearly absent, while it indeed occurs for the 1D results. This illustrates the validity of the explanation given in this appendix. Note that the 2D model does retain the strong polarisation ratio of -30 dB that is characteristic for Bragg scattering.

Bibliography

[1] *Handbook of mathematical functions*, edited by Abramowitz, M., Segun, I.A., Dover Publications, Inc., New York, USA, 1965.

[2] Apel, J.R.: *Principles of ocean physics*, International geophysics series, vol. 38, Academic press limited, Londen, UK, 1987.

[3] Apel, J.R.: An improved model of the ocean surface wave vector spectrum and its effects on radar backscatter, *Journal of Geophysical Research*, vol. 99, no. C8, pp. 16269-16291, 1994.

[4] Babanin, A.V., Young, I.R., Banner, M.L.: Breaking probability for dominant waves on water of finite constant depth, *Journal of Geophysical Research*, vol. 106, no C6, pp. 11659-11676, 2001.

[5] Baker, C.J., Ward, K.D., Watts, S.: The significance and scope of the compound K-distribution model for sea clutter, *Proceedings of Radar 87*, 19-21 October 1987, London, UK.

[6] Balanis, C.A.: *Advanced engineering electromagnetics*, John Wiley & Sons Inc., New York, 1989.

[7] Banner, M.L., Peregrine, D.H.: Wave breaking in deep water, *Annual Review of Fluid Mechanics*, vol. 25, p. 373-397, 1993.

[8] Banner, M.L., Tian, X.: On the determination of the onset of breaking for modulating surface gravity water waves, *Journal of Fluid Mechanics*, vol. 367, pp. 107-137, 1998.

[9] Banner, M.L., Babanin, A.V., Young, I.R.: Breaking probability for dominant waves on the sea surface, *Journal of Physical Oceanography*, vol. 30, pp. 3145-3160, 2000.

[10] Barrick, D.E.: Rough surface scattering based on the specular point theory, *IEEE Transactions on Antennas and Propagation*, vol. 17, pp. 590-597, 1969.

[11] Barrick, D.E.: Near-grazing illumination and shadowing of rough surfaces, *Radio Science*, vol. 30, no. 3, pp. 563-580, 1995.

[12] Bonmarin P., Geometric properties of deep-water breaking waves, *Journal of Fluid Mechanics*, vol. 209, pp. 405-433, 1989.

[13] Booij, N., Ris, R.C., Holthuijsen, L.H.: A third-generation wave model for coastal regions 1. Model description and validation, *Journal of Geophysical Research*, vol. 104, no C4, pp. 7649-7666, 1999.

[14] Brand, M.G.E., Ewijk, L.J. van: *Validation and results of the high-frequency radar cross section prediction model*, TNO-Report, FEL-93-A017, TNO Physics and Electronics Laboratory, The Hague, The Netherlands, 1993.

[15] Brand, M.G.E.: *Radar Signature Analysis and Prediction by Physical Optics and Ray Tracing. The RAPPORT Code for RCS Prediction*, TNO-Report, FEL-95-A097, TNO Physics and Electronics Laboratory, The Hague, The Netherlands, 1996.

[16] Chen, F.: Computer simulation of wave scattering from three-dimensional conducting random surfaces, *International Journal of Remote Sensing*, vol. 21, no. 4, pp. 777-790, 2000.

[17] Cointe, R., Tulin, M.P.: A theory of steady breakers, *Journal of Fluid Mechanics*, vol. 276, pp. 1-20, 1994.

[18] Creamer, D.B., Henyey, F., Schult, R., Wright, J.: Improved linear representation of ocean surface waves, *Journal of Fluid Mechanics*, vol. 205, pp. 135-161, 1989.

[19] Crombie, D.D.: Doppler spectrum of sea echo at 13.56 Mc/s, *Nature*, vol. 175, pp. 681-682, 1955.

[20] DeSanto, J.A.: *Scalar Wave Theory - Green's Functions and Applications*, Springer-Verlag Berlin Heidelberg, 1992

[21] Donelan, R., Pierson, W.J.: Radar scattering and equilibrium ranges in wind-generated waves with application to scatterometry, *Journal of Geophysical Research*, vol. 92, pp. 4971-5029, 1987.

[22] Donohue, D.J., Ku, H.C., Thompson, D.R., Sadowsky, J.: Direct numerical simulation of electromagnetic rough surface and sea scattering by an improved banded matrix iterative method, *Johns Hopkins APL Technical Digest*, vol. 18, no. 2, pp. 204-216, 1997.

[23] Eldeberky, Y., Battjes, J.A.: Spectral modeling of wave breaking: Application to Boussinesq equations, *Journal of Geophysical Research*, vol. 101, no. C1, pp. 1253-1264, 1996.

[24] Elfouhaily, T., Chapron, B., Katsaros, K.: A unified directional spectrum for long and short wind-driven waves, *Journal of Geophysical Research*, vol. 102, no. C7, pp. 15781-15796, 1997.

[25] Ericson, E.A., Lyzenga, D.R., Walker, D.T.: Radar backscatter from stationary breaking waves, *Journal of Geophysical Research*, vol. 104, no. C12, pp. 29679-29695, 1999.

[26] Ewijk, L.J. van: *Technical Formulation of the High-Frequency Radar Cross Section Prediction Model*, TNO-Report, FEL-92-A286, TNO Physics and Electronics Laboratory, The Hague, The Netherlands, 1992.

[27] Feynman, R.P., Leighton, R.B., Sands, M.L.: *The Feynman lectures on physics, Volume I*, Addison-Wesley Publishing Co., Inc., Reading, Massachusetts, 1964.

[28] Feynman, R.P., Leighton, R.B., Sands, M.L.: *The Feynman lectures on physics, Volume II*, Addison-Wesley Publishing Co., Inc., Reading, Massachusetts, 1964.

[29] Fuchs, J., Lamont-Smith T. ,Tulin, M.P.: Laboratory measurements of LGA Doppler spectral components and their physical sources unveiled, *Proceedings of IGARSS*, 6-10 July 1998, Seattle, WA, USA.

[30] Fuchs, J., Regas, D., Waseda, T., Welch, S. ,Tulin, M.P.: Correlation of hydrodynamic features with LGA radar backscatter from breaking waves, *IEEE Transactions on Geoscience and Remote Sensing*, vol. 37, no. 5, p. 2442-2460, 1999.

[31] Fung, A.K., Chan, H.L.: Backscattering of waves by composite rough surfaces, *IEEE Transactions on Antennas and Propagation*, vol. 17, pp. 590-597, 1969.

[32] Greco, M., Bordoni, F., Gini, F.: X-band sea-clutter nonstationarity: Influence of long waves, *IEEE Journal of oceanic engineering*, vol. 29, no. 2, pp. 269-283, 2004.

[33] Greidanus, H., Melief, H.W., Genderen, P. van, Hoogeboom, P.: Doppler polarimetry of high resolution radar sea clutter, *Proceedings of IGARSS*, 9-13 July 2001, Sydney, Australia

[34] Harrington, R.F.: *Field computation by moment method*, The MacMillan Company, New York, USA, 1968.

[35] Hays, W.L.: *Statistics*, Harcourt Brace College Publishers, Fort Worth, Texas, USA,1994.

[36] Holliday, D., St-Cyr, G.J., Woods, N.E.: A radar ocean imaging model for small to moderate incidence angles, *International journal of remote sensing*, vol. 7, no. 12, p. 1809-1834, 1986.

[37] Holliday, D., DeRaad, Jr., L.L., St-Cyr, G.J.: Forward-Backward: A new method for computing low-grazing angle scattering, *IEEE Transactions on Antennas and Propagation*, vol. 44, no. 5, p. 722-729, 1996.

[38] Holliday, D., DeRaad, Jr., L.L., St-Cyr, G.J.: Forward-Backward method for scattering from imperfect conductors, *IEEE Transactions on Antennas and Propagation*, vol. 46, no. 1, p. 101-107, 1998.

[39] Holliday, D., DeRaad, Jr., L.L., St-Cyr, G.J.: Sea-spike backscatter from a steepening wave, *IEEE Transactions on Antennas and Propagation*, vol. 46, no. 1, p. 108-113, 1998.

[40] Holthuijsen, L.H., Herbers, T.H.C.: Statistics of breaking waves observed as white-caps in the open sea, *Journal of Physical Oceanography*, vol. 16, pp. 290-297, 1986.

[41] Janssen P.A.E.M., Wallbrink, H., Calkoen, C.J., van Halsema, D., Oost, W.A., Snoeij, P.: VIERS-1 scatterometer model, *Journal of Geophysical Research*, vol. 103, no. C4, pp. 7807-7831, 1998.

[42] Jessup, A.T., Keller W.C. , Melville, W.K.: Measurements of sea spikes in microwave backscatter at moderate incidence, *Journal of Geophysical Research*, vol. 95, no. C6, pp. 9679-9688, 1990.

[43] Jessup, A.T., Melville, W.K., Keller W.C.: Breaking waves affecting microwave backscatter 1. Detection and verification, *Journal of Geophysical Research*, vol. 96, no. C11, pp. 20547-20559, 1991.

[44] Jessup, A.T., Melville, W.K., Keller W.C.: Breaking waves affecting microwave backscatter 1. Detection and verification, *Journal of Geophysical Research*, vol. 96, no. C11, pp. 20561-20569, 1991.

[45] Kapp, D.A., Brown, G.S.: A new numerical method for rough-surface scattering calculations, *IEEE Transactions on Antennas and Propagation*, vol. 44, p. 711-721, 1996.

[46] Kinsman, B.: *Wind waves*, Dover publications, New York, USA, 1965.

[47] Lee, P.H.Y., Barter, J.D., Beach, K.L., Hindman, C.L., Lake, B.M., Rungaldier, H., Shelton, J.C., Williams, A.B., Yee, R., Yuen, H.C., X band microwave backscattering from ocean waves, *Journal of Geophysical Research*, vol. 100, no. C2, p. 2591-2611, 1995.

[48] Lee, P.H.Y., Barter, J.D. Caponi, E., Caponi, M., Hindman, C.L., Lake, B.M., Rungaldier, H.: Wind speed dependence of small-grazing angle microwave backscatter from sea surfaces, *IEEE Transactions on Antennas and Propagation*, vol. 44, p. 333-340, 1996.

[49] Lee, P.H.Y., Barter, J.D., Beach, K.L., M., Hindman, C.L., Lake, B.M., Rungaldier, H., Yee, R.: Experiments on Bragg and non-Bragg scattering using single-frequency and chirped radars, *Radio Science*, vol. 32, no. 5, pp. 1725-1744, 1997.

[50] Lee, P.H.Y., Barter, J.D., Beach, K.L., Lake, B.M., Rungaldier, H., Thompson, H.R., Yee, R.: Scattering from breaking gravity waves without wind, *IEEE Transactions on Antennas and Propagation*, vol. 46, no. 1, p. 14-26, 1998.

[51] Lee, P.H.Y., Barter, J.D., Lake, B.M., Thompson, H.R.: Lineshape analysis of breaking-wave Doppler spectra, *IEE Proceedings Radar, Sonar, Navigation*, vol. 145, no. 2, pp 135-139, 1998

[52] Liu, Y., Frasier, S.J., McIntosh, R.E., Measurement and classification of low-grazing-angle radar sea spikes, *IEEE Transactions on Antennas and Propagation*, vol. 46, no.1, p. 27-40, 1998.

[53] Longuet-Higgins, M.S.: Integral properties of periodic gravity waves of finite amplitude, *Proceedings royal society London A*, vol. 342, pp. 157-174, 1975.

[54] Longuet-Higgins, M.S., Cokelet, E.D.: The deformation of steep gravity waves on water. II Growth of normal-mode instabilities, *Proceedings royal society London A*, vol. 364, pp. 1-28, 1978.

[55] Longuet-Higgins, M.S.: Crest instabilities of gravity waves. II The almost highest wave, *Journal of Fluid Mechanics*, vol. 258, pp. 115-129, 1994.

[56] Lyzenga, D.R.: Ocean wave spectrum and dissipation rate derived from CMOD4 model function, *Journal of Geophysical Research*, vol. 109, no. C07019, pp. 1-9, 2004.

[57] McLaughlin, D.J., Allan, N., Twarog, E.M., Trizna, D.B., High resolution polarimetric radar scattering measurements of low grazing angle sea clutter, *IEEE Journal of Oceanographic Engineering*, vol. 20, no. 3, p. 166-178, 1995.

[58] Melief, H.W., Greidanus, H., Genderen, P. van, Hoogeboom, P.: Low grazing angle sea clutter modelled by ray tracing and physical optics, *RTO Meeting Proceedings 60*, RTO-MP-60 AC/323(SET)TP/12, 2000.

[59] Melief, H.W., Greidanus, H., Genderen, P. van, Hoogeboom, P.: Doppler and polarimetric analysis of sea spikes, *Proceedings of URSI-F symposium*, 12-14 Februari 2002, Garmisch- Partenkirchen, Germany

[60] Melief, H.W., Greidanus, H., Genderen, P. van, Hoogeboom, P.: Modelling radar backscatter from breaking waves on the surface, *Proceedings of IGARSS*, 21-25 July 2003, Toulouse, France

[61] Melief, H.W., Greidanus, H., Genderen, P. van, Hoogeboom, P.: Analysis of sea spikes in radar sea clutter data, *IEEE Transaction on Geoscience and Remote Sensing*, Vol. 44, No. 4, pp. 985-993, 2006

[62] Milder, D.M.: An improved formalism for electromagnetic scattering from a perfectly conducting rough surface, *Radio Science*, vol. 31, no. 6, pp. 1369-1376, 1996.

[63] Ngo, H.D., Rino, C.L.: The application of beam simulation to scattering at low grazing angles - Part I: Methodology and validation, *Radio Science*, vol. 29, no. 6, pp. 1365-1379, 1994.

[64] Nohara, T.J., Hayin, S.: Canadian east coast radar trials and the K-distribution, *IEE Proceedings-F*, vol. 138, no 2, pp.80-88, 1991.

[65] Peake, W.H.: Theory of radar return from terrain, *IRE National Convention Record*, vol. 7, pp. 27-41, 1959.

[66] Pierson, W.J., Moskowitz, L.: A proposed spectral form for fully developed wind seas based on the similarity theory of S.A. Kitaigorodskii, *Journal of Geophysical Research*, vol. 69, pp. 5181-5190, 1964.

[67] Phillips, O.M.: Radar returns from the sea surface - Bragg scattering and breaking waves, *Journal of physical oceanography*, vol. 18, pp. 1065-1074, 1988.

[68] Plant, W.J.: Bragg scattering of electromagnetic waves from the air/sea interface, *Surface waves and fluxes*, vol. II, Geernaert, G.L., Plant, W.J. (editors), Kluwer Academic Publishers, Dordrecht, The Netherlands, pp. 41-108, 1990

[69] Plant, W.J., Dahl, P.H., Keller, W.C.: Microwave and acoustic scattering from parasitic capillary waves, *Journal of Geophysical Research*, vol. 104, no. C11, pp. 25852-25866, 1999.

[70] Plant, W.J., Dahl, P.H.: Bound and free surface waves in a large wind-wave tank, *Journal of Geophysical Research*, vol. 109, no. C10002, pp. 1-14, 2004.

[71] Rao, S.M., Wilton, D.R., Glisson A.W.: Electromagnetic scattering by surfaces of arbitrary shape, *IEEE Transactions on Antennas and Propagation*, vol. 30, no. 3, pp. 409-418, 1982.

[72] Rice, S.O.: Reflection of electromagnetic waves from slightly rough surfaces, *Communications on Pure and Applied Mathematics*, vol. 4, pp. 351-378, 1951.

[73] Rino, C.L., Crystal, T.L., Koide, A.K., Ngo, H.D., Guthart, H.: Numerical simulation of backscatter from linear and nonlinear ocean surface realization, *Radio Science*, vol. 26, no. 1, pp. 51-71, 1991.

[74] Rino, C.L., Ngo, H.D.: The application of beam simulation to scattering at low grazing angles - Part II: Ocean-like surfaces, *Radio Science*, vol. 29, no. 6, pp. 1381-1391, 1994.

[75] Rino, C.L., Ngo H.D.: Numerical simulation of low-grazing angle ocean microwave backscatter and its relation to sea spikes, *IEEE Transactions on Antennas and Propagation*, vol. 46, no. 1, p. 133-141, 1998.

[76] Ris, R.C., Holthuijsen, L.H., Booij, N.: A third-generation wave model for coastal regions 2. Verification, *Journal of Geophysical Research*, vol. 104, no C4, pp. 7667-7681, 1999.

[77] Romeiser, R., Alpers, W., Wismann, V.: An improved composite surface model of the ocean surface 1. Theory of the model and optimization/ validation by scatterometer data, *Journal of Geophysical Research*, vol. 102, no. C11, pp. 25237-25250, 1997.

[78] Romeiser, R., Alpers, W.: An improved composite surface model of the ocean surface 2. Model response to surface roughness variations and the radar imaging of underwater bottom topography, *Journal of Geophysical Research*, vol. 102, no. C11, pp. 25251-25267, 1997.

[79] Rozenberg, A.D., Ritter, M.J., Melville, W.K., Gottschall, C.C., Smirnov, A.V.: Free and bound capillary waves as microwave scatterers: Laboratory studies, *IEEE Transactions on Geoscience and Remote Sensing*, vol. 37, no. 2, p. 1052-1065, 1999.

[80] Rozenberg, A.D., Ritter, M.J.: Laboratory study of the fine structure of short surface waves due to breaking: Two-directional wave propagation, *Journal of Geophysical Research*, vol. 110, no. C02011, pp. 1-14, 2005.

[81] Ruck, G.T. (ed.), Barrick, D.E., Stuart, W.D., Krichbaum, C.K.: *Radar cross section handbook, Volume 1*, Plenum press, New York, USA, 1970.

[82] Ruck, G.T. (ed.), Barrick, D.E., Stuart, W.D., Krichbaum, C.K.: *Radar cross section handbook, Volume 2*, Plenum press, New York, USA, 1970.

[83] Shaw, W.T., Dougan, A.J.: Green's function refinement as an approach to radar backscatter: General theory and applications to LGA scattering from the ocean, *IEEE Transactions on Antennas and Propagation*, vol. 46, no. 1, p. 57-66, 1998.

[84] Skolnik, M.: *Radar Handbook Second Edition*, McGraw-Hill, Boston, Massachusetts, USA, 1990.

[85] Sletten, M.A., Wu, J.: Ultrawideband, polarimetric radar studies of breaking waves at low grazing angles, *Radio Science*, vol. 31, no. 1, pp. 181-192, 1996.

[86] Sletten, M.A.: Multipath scattering in ultrawide-band radar sea spikes, *IEEE Transactions on Antennas and Propagation*, vol. 46, no. 1, p. 45-56, 1998.

[87] Sletten, M.A., West, J.C.: Radar investigations of breaking water waves at low grazing angles with simultaneous high-speed optical imagery, *Radio Science*, vol. 38, no. 6, pp. 18 1-17, 2003.

[88] Spivack, M.: A numerical approach to rough-surface scattering by the parabolic equation method, *Journal of the Optical Society of America*, vol. 87, no. 5, pp. 1999-2004, 1990.

[89] Smith, M.J., Poulter, E.M., McGregor, J.A.: Doppler radar measurements of wave groups and breaking waves, *Journal of Geophysical Research*, vol. 101, no. C6, pp. 14269-14282, 1996.

[90] Smith, R.A.: The operator expansion formalism for electromagnetic scattering from rough dielectric surfaces, *Radio Science*, vol. 31, no. 6, pp. 1377-1385, 1996.

[91] Stevens C.L., Poulter, E.M., Smith, M.J., McGregor, J.A.: Nonlinear features in wave-resolving microwave radar observations of ocean waves, *IEEE Journal of oceanic engineering*, vol. 24, no. 4, pp. 470-480, 1999.

[92] Stokes, G.G.: Considerations relative to the greatest height of oscillatory irrotational waves which can be propagated without change of form, *Mathematical & Physics Papers 1*, pp. 225-228, 1880.

[93] Tatarskii, V.I., Charnotskii, M.I.: On the universal behavior of scattering from a rough surface for small grazing angles, *IEEE Transactions on Antennas and Propagation*, vol. 46, no. 1, p. 67-72, 1998.

[94] Thomas, G.P., Klopman, G.: Wave-current interactions in the nearshore region, *Advances in fluid mechanics, gravity waves of finite depth*, Hunt, J.N. (editor), Southampton: Computational mechanics publications, ISBN 1-85312351-X, chapter 7, pp. 255-319, 1997.

[95] Thorsos, E.I.: The validity of the Kirchhoff approximation for rough surface scattering using a Gaussian roughness spectrum, *Journal of the Acoustical Society of America*, vol. 83, no. 1, pp. 78-92, 1988.

[96] Toporkov, J.V., Awadallah, R.S., Brown, G.S.: Issues related to the use of a Gaussian-like incident field for low-grazing-angle scattering, *Journal of the Optical Society of America*, vol. 16, no.1, pp. 176-187, 1999

[97] Trizna, D.B., Hansen, J.P., Hwang, P., Wu, J., Laboratory studies of radar sea spikes at low grazing angles, *Journal of Geophysical Research*, vol. 96, no. C7, p. 12529-12537, 1991.

[98] Trizna D.B.: Statistics of low grazing angle radar sea scatter for moderate and fully developed ocean waves, *IEEE Transactions on Antennas and Propagation*, vol. 39, no. 12, p. 1681-1690, 1991.

[99] Trizna D.B.: A model for Brewster angle damping and the multipath effects on the microwave radar sea echo at low grazing angles, *IEEE Transactions on Geoscience and Remote Sensing*, vol. 35, no. 5, p. 1232-1244, 1999.

[100] Ulaby, F.T., Moore, R.K., Fung, A.K.: *Microwave remote sensing: active and passive, Volume I*, Artech House, Norwood, Massachusetts, 1981.

[101] Ulaby, F.T., Moore, R.K., Fung, A.K.: *Microwave remote sensing: active and passive, Volume II*, Artech House, Norwood, Massachusetts, 1982.

[102] Ulaby, F.T., Moore, R.K., Fung, A.K.: *Microwave remote sensing: active and passive, Volume III*, Artech House, Norwood, Massachusetts, 1986.

[103] Valenzuela, G.R.: Depolarization of E.M. waves by slightly rough surfaces, *IEEE Transactions on Antennas and Propagation*, vol. 15, pp. 552-557, 1967.

[104] Valenzuela, G.R.: Theories for the interaction of electromagnetic and oceanic waves - A review, *Boundary-layer Meteorology*, vol. 13, pp. 61-85, 1978.

[105] Vogelzang, J.: *Radar imaging of sea bottom topography*, Ph.D. thesis, Universiteit Utrecht, 1998.

[106] Voronovich, A.G.: On the theory of electromagnetic waves scattering from the sea surface at low grazing angles, *Radio Science*, vol. 31, no. 6, pp. 1519-1530, 1996.

[107] Walker D.: Experimentally motivated model for low grazing angle radar Doppler spectra of the sea surface, *IEE Proceedings Radar, Sonar, Navigation*, vol. 147, no. 3, pp 114-120, 2000

[108] Walker D.: Doppler modelling of radar sea clutter, *IEE Proceedings Radar, Sonar, Navigation*, vol. 148, no. 2, pp 73-80, 2001

[109] Wang P., Yao, Y., Tulin, M.P.: An efficient numerical tank for non-linear water waves, based on the multi-subdomain approach with BEM, *International Journal for Numerical Methods in Fluids*, vol. 20, pp. 1315-1336, 1995.

[110] Ward, K.D., Baker, C.J., Watts, S.: Maritime surveillance radar part 1: Radar scattering from the ocean surface, *IEE Proceedings-F*, vol. 137, no. 2, pp. 51-62, 1990.

[111] Watts, S., Baker, C.J., Ward, K.D.: Maritime surveillance radar part 1: Detection performance prediction in sea clutter, *IEE Proceedings-F*, vol. 137, no. 2, pp. 63-72, 1990.

[112] Werle, B.O., Sea backscatter, spikes and wave group observations at low grazing angles, *IEEE International Radar Conference*, p. 187-195, 1995.

[113] Werle, B.O., Directional characteristics of sea-wave scattering observed at lows grazing angles, *IEEE Transactions on Antennas and Propagation*, vol. 46, no. 1, p. 41-44, 1998.

[114] West J.C.: Effect of shadowing on electromagnetic scattering from rough ocean wavelike surfaces at small grazing angles, *IEEE Transactions on Geoscience and Remote Sensing*, vol. 35, no. 2, p. 293-301, 1997.

[115] West J.C., Sturm, J.M., Ja, S.J.: Low-grazing-angle scattering from breaking water waves using an impedance boundary MM/GTD approach, *IEEE Transactions on Antennas and Propagation*, vol. 46, no. 1, p. 93-100, 1998.

[116] West J.C.: Ray analysis of low-grazing scattering from a breaking water wave, *IEEE Transactions on Geoscience and Remote Sensing*, vol. 37, no. 6, p. 2725-2727, 1999.

[117] West J.C.: Integral equation formulation for iterative calculation of scattering from lossy rough surfaces, *IEEE Transactions on Geoscience and Remote Sensing*, vol. 38, no. 4, p. 1609-1615, 2000.

[118] West J.C.: Low-grazing-angle (LGA) Sea-Spike backscattering from plunging breaker crests, *IEEE Transactions on Geoscience and Remote Sensing*, vol. 40, no. 2, p. 523-526, 2002.

[119] Wright, J.W.: Backscattering from capillary waves with application to sea clutter, *IEEE Transactions on Antennas and Propagation*, vol. 14, pp. 749-754, 1966.

[120] Young, I.R., Rosenthal, W., Ziemer, F.: A three-dimensional analysis of marine radar images for the determination of ocean wave directionality and surface currents, *Journal of Geophysical Research*, vol. 90, p. 1049-1059, 1985.

[121] Zavorotny, V.U., Voronovich, A.G., Two-scale model and ocean radar Doppler spectra at moderate- and low-grazing angles, *IEEE Transactions on Antennas and Propagation*, vol. 46, no. 1, p. 84-92, 1998.

[122] Zhang, S., Yuan, Y.: Energy and momentum dissipation through wave breaking, *Journal of Geophysical Research*, vol. 110, no. C09021, pp. 1-13, 2005.

[123] Zwamborn, A.P.M.: *Scattering by objects with electric contrast*, Ph.D. Thesis, Delft University Press, Delft, The Netherlands, 1991.

[124] Zwamborn, A.P.M.: Private communications, 2004.

Samenvatting

Dynamische modellering van radar-zeeclutter

Sinds het einde van de Koude Oorlog is er in toenemende mate behoefte aan radarsystemen voor de detectie van kleine en/of zwakke doelen (bijvoorbeeld kleine schepen). Een radar is een systeem dat elektromagnetische straling uitzendt, die vervolgens op objecten in de omgeving reflecteert. Vervolgens neemt de radar deze echo's waar en bouwt daarmee een beeld op van de omgeving. Radar wordt gekenmerkt door drie eigenschappen, vermogen, polarisatie en Doppler-snelheid. Vermogen is een maat voor de sterkte van de ontvangen reflecties en wordt ook wel radar-doorsnede genoemd. Polarisatie geeft de richting aan van het elektromagnetische veld. Doppler-snelheid vertelt hoe snel een object zich naar de radar toe beweegt. Het probleem met de detectie van kleine doelen is dat ze lastig te onderscheiden zijn van de reflecties van het zeeoppervlak, de zogenaamde zeeclutter. Dit proefschrift heeft als doel om een verbeterd model van zeeclutter te ontwerpen, dat gebruikt kan worden voor de detectie van kleine en/of zwakke doelen.

Tegen deze achtergrond worden in hoofdstuk 1 de drie voornaamste doelen van dit proefschrift gedefinieerd. Het eerste doel is het vinden van hiaten in de kennis over zeeclutter door middel van een literatuurstudie. Zeeclutter wordt voornamelijk op drie manieren bestudeerd: 1) door het meten en interpreteren van zeeclutterdata; 2) door het opstellen van statistische modellen; en 3) door het opstellen van fysische modellen. In dit proefschrift ligt de nadruk op de derde methode, waarbij de eerste methode wordt gebruikt als validatie van het model.

Uit het literatuuronderzoek bleek dat er twee soorten fysische modellen van zeeclutter bestaan, die beiden echter slechts een deelproces beschrijven. Aan de ene kant zijn er de 'composite surface' modellen. Deze modellen beschrijven het globale zee-oppervlak door middel van een collectie platte vlakjes. Dit kan analytisch gebeuren, zoals in dit proefschrift, waarbij een realisatie van het oppervlak wordt gemaakt, of statistisch, waarbij de verdeling van de hellingen van de vlakjes wordt

berekend. In beide gevallen worden de kleine rimpelingen op het oppervlak statistisch beschreven. De zeeclutter wordt vervolgens bepaald door voor elk vlakje de reflecties uit te rekenen, gegeven de lokale invalshoek op het vlakje en de statistische eigenschappen van de rimpelingen op het vlakje.

Het tweede type model beschrijft de zogenaamde 'sea spikes'. Dit zijn plotselinge gebeurtenissen in de zeeclutter, die gekarakteriseerd worden door simultane pieken in vermogen, polarisatie-ratio en Doppler-snelheid. Deze gebeurtenissen blijken goed gemodelleerd te kunnen worden door de reflectie aan (bijna) brekende golven.

Deze twee typen modellen zijn ieder in staat om een deel van radar-zeeclutter te beschrijven, maar er zijn weinig tot geen modellen die de gehele zeeclutter goed simuleren. De bovengenoemde 'composite surface modellen' beschrijven de clutter van het globale oppervlak. Hoewel het mogelijk is om modellen van 'sea spikes' (brekende golven) te maken, is niet goed bekend waar deze gebeurtenissen op het oppervlak voorkomen. Dit is het voornaamste probleem bij het combineren van de beide type modellen. Om dit op te lossen, is een golfbrekingscriterium nodig, wat dus juist één van de voornaamste hiaten is in de kennis van zeeclutter. Een tweede ontbrekende factor in de meeste zeeclluttermodellen is de dynamica van zeeclutter. Dit houdt in dat meestal noch de Doppler-snelheid van de clutter noch de ontwikkeling van de clutter in de tijd gemodelleerd worden.

Het tweede doel van dit proefschrift was het bouwen van een algemeen zeeclluttermodel dat deze hiaten opvult. Dit model combineert een aantal oceanografische en elektromagnetische modellen en breidt ze, waar nodig, uit om zo de belangrijkste processen te modelleren die bijdragen aan zeeclutter. Dit is de voornaamste bijdrage die dit proefschrift levert aan dit onderzoeksgebied. De verschillende componenten zijn beschreven in de hoofdstukken 2 en 3. In hoofdstuk 2 worden oceanografische modellen besproken en in hoofdstuk 3 komen elektromagnetische modellen aan bod.

Hierbij bleek dat voor de berekening van reflectie aan brekende golven een gevanceerde elektromagnetische methode nodig was. De afleiding en implementatie van een dergelijk model wordt beschreven in hoofdstuk 4. Dit werd gedaan met behulp van de 'Method of Moments' (MoM). Dit model is in staat om de reflecties op verschillende objecten te berekenen, waaronder brekende golven.

Om de verschillende modellen aan elkaar te knopen is dus één extra component nodig: een golfbrekingscriterium. Uit de literatuur blijkt dat er geen consensus is over hoe golfbreking op volle zee optreedt. Wat wel duidelijk is, is dat breking optreedt als een golf te steil wordt. De steilheid kan afgeleid worden uit twee grootheden, de orbitaal-snelheid en de voortplantingssnelheid van de golf. Orbitaalsnelheid ontstaat doordat de waterdeeltjes een cirkelbeweging maken bij het passeren van een golf. Door deze twee snelheden te combineren kunnen de tijd, de plaats en de grootte van de brekende golven op het zeeoppervlak bepaald worden.

De verschillende componenten, zoals gepresenteerd in de hoofdstukken 2 tot en met 4, zijn vervolgens gecombineerd om het algemene model te verkrijgen dat aan

het tweede doel van het proefschrift voldoet. Dit model is beschreven in hoofdstuk 5 en bestaat uit 6 delen:

i. Simulatie van het zeeoppervlak: Deze simulatie wordt verkregen door een Fourier-synthese van het golfspectrum van het zeeoppervlak. Hierbij wordt het oppervlak beschreven als een collectie van kleine vlakjes met een bepaalde helling.

ii. Simulatie van brekende golven: Het golfbrekingscriterium wordt toegepast op dit oppervlak om de de tijd, de plaats en de grootte van de brekende golven op het oppervlak te vinden.

iii. Ray-tracing: Dit is een techniek om uit te vinden (i) welke delen (vlakjes) van het oppervlak niet zichtbaar zijn voor de radar, en (ii) wat de lokale invalshoeken zijn op de rest van het oppervlak.

iv. Bragg-berekening: Deze lokale invalshoeken worden gecombineerd met een statistische beschrijving van de rimpelingen op het oppervlak om het ontvangen vermogen van het oppervlak uit te rekenen. De stappen iii) en iv) vormen samen een zogenaamd 'composite surface' model.

v. Spike-berekening: Door middel van stap ii) zijn de tijd, de plaats en de grootte van de brekende golven bekent. Vervolgens wordt de MoM-code gebruikt om de radar-doorsnede van de brekende golven te berekenen. Dit levert een 'sea spike' op waarvan de snelheid ongeveer gelijk is aan de voortplantingssnelheid van de brekende golf.

vi. RCS-combinatie: De resultaten van de Bragg- en spike-berekeningen worden opgeteld om de totale radar-doorsnede (RCS) van elk vlakje te verkrijgen.

Deze zes stappen genereren één tijdstap van de zeeclutter-simulatie. Door deze procedure te herhalen, kan een tijdserie van elke gewenste lengte worden verkregen. De zodanig verkregen zeeclutter-simulatie combineert een 'composite surface' model met 'sea spikes'. Bovendien worden ook de snelheid en de ontwikkeling van de zeeclutter in de tijd bepaald, wat betekent dat het voldoet aan tweede doel van dit proefschrift.

Het derde doel van dit proefschrift was het valideren van het model door een vergelijking met gemeten zeeclutter-data. De data-analyse die is uitgevoerd om dit doel te bereiken wordt beschreven in hoofdstuk 6 en in [61]. Drie sets van zeeclutter data zijn hierbij geanalyseerd op een aantal manieren. De analyse liet zien dat zeeclutter is opgebouwd uit 1) een globale achtergrond die veroorzaakt wordt door het proces dat ten grondslag ligt aan de 'composite surface' modellen, en 2) sea spikes, die veroorzaakt worden door reflectie op brekende golven. Bovendien bleek dat de Doppler-snelheid de beste grootheid is voor de fysische interpretatie van

de data. Concluderend laten de data het beeld zien van zeeclutter dat vanuit de literatuur voorspeld wordt.

Het afstemmen en valideren van het model wordt beschreven in hoofdstuk 7. Door het afstemmen kon een gesimuleerde dataset verkregen worden die vergelijkbaar was met de gemeten data. Dit maakte het mogelijk om de analyses die op de gemeten data waren uitgevoerd ook toe te passen op de gesimuleerde data. De simulatieresultaten kwamen goed overeen met de resultaten van de metingen. De enige significante verschillen zaten in histogrammen van de radardoorsnede. De histogrammen van de gesimuleerde data bleken namelijk een staart te hebben aan de kant van de lage vermogens. Dit was een direct gevolg van het feit dat het model 1-dimensionaal is.

Een tweede verschil zat in de polarisatie-eigenschappen, die volgen uit deze histogrammen. Op grond van de literatuur voorspelt het model een zogenaamde polarisatieratio van -30 dB, terwijl de gemeten data een ratio van -10 dB liet zien. In hoofdstuk 7 word dieper op dit verschil ingegaan en werd een mogelijke oplossing, het toevoegen van microbreakers aan het model, verder uitgewerkt. De resultaten hiervan toonden aan dat het toevoegen van microbreakers, hele kleine brekende golven, de polarisatieratio van het model kan verhogen naar het gemeten niveau.

Concluderend kan gesteld worden dat het in dit proefschrift gepresenteerde model voldoet aan de doelen die gesteld werden in hoofdstuk 1. Het draagt met name bij aan onderzoek van radar-zeeclutter door de combinatie van oceanografische en elektromagnetische modellen.

Summary

Dynamic modelling of radar seaclutter

Since the end of the Cold War, there is an increasing need for radar systems with higher resolutions and sensitivities to detect small and/or weak targets (e.g. small ships). This requirement, however, has also led to increasing difficulty with so-called radar seaclutter, i.e. scattering from the ocean surface. This thesis aims at the development of an improved model of seaclutter, which may be employed for detecting small and/or weak targets.

Against this background, chapter 1 states the three main goals of this thesis. The first of these was to identify the gaps in knowledge of seaclutter through a literature study. The results of this study identified two main gaps: 1) There are many models of tilt-modulated Bragg scattering and of the so-called sea spikes, but few models combine both these components. 2) There are few, if any, dynamic models of radar seaclutter.

The second goal of this thesis was to build a comprehensive seaclutter model that fills these gaps. This model combines and extends a number of (known) hydrodynamic and electromagnetic models to capture most of the processes that lead to the seaclutter. This is the main contribution that this thesis makes to the field of seaclutter research. The different components are described in chapters 2 (ocean surface models) and 3 (electromagnetic models). These include ocean surface spectral analysis, breaking wave models, ray tracing and Bragg scattering. In particular, for the hydrodynamic simulations of breaking wave profiles the results of the LONGTANK simulator were used.

During this research it became apparent that a full-wave electromagnetic model was needed to evaluate scattering on these breaking wave profiles. The derivation and implementation of such a model is described in chapter 4. Both the electric (EFIE) and magnetic (MFIE) integral equations were defined, because they were needed to evaluate horizontally as well as vertically polarised radiation. The equations were then solved using the Method of Moments (MoM). The so-obtained method is capable of treating scattering on a wide range of objects. It was vali-

dated on a number of flat plates and cylinders of different sizes and then used for evaluating breaking wave profiles, as a part of the larger model.

One additional component was needed to complete the model: a breaking wave criterion. It was found that no clear consensus exists about which criteria lead to wave breaking. What is clear is that wave breaking occurs when the steepness of a wave becomes too large. Also, there is evidence that this can occur during wave interactions in wave groups. To model these types of processes a wave breaking criterion was devised in this thesis, which was based on the ratio between the cumulative orbital velocity experienced by a wave and its phase velocity. The cumulative orbital velocity is defined by the sum of the orbital velocities of all the waves in a spectral band around the wavenumber of the wave under consideration. This criterion was capable of predicting the size and temporal and spatial location of the generated breaking waves.

The different components presented in chapters 2 to 4 were then combined with the breaking wave criterion to obtain the comprehensive model desired by the second goal. This was described in detail in chapter 5 of this thesis. This model consists of six parts:

i. Spectral surface generation: A simulation of the ocean surface is generated through a Fourier transformation of a parameterisation of an ocean surface spectrum.

ii. Breaking wave generation: The breaking wave criterion is applied to the spectral surface to obtain the locations and wavelengths of the breaking waves on that surface. A useful side result of this algorithm is that it allows the calculation of the radial component of the orbital velocity at each point of the surface.

iii. Surface evaluation: The surface is divided into separate patches. A backward ray-tracing algorithm is employed to find whether any of the patches are shadowed and if not, what the local incidence angles on the patches are.

iv. Bragg calculation: Given the local incidence angle on the patches a Bragg scattering algorithm is used to determine the composite surface radar cross section of each patch. The Doppler velocity of each patch is defined as the sum of the phase velocity of the Bragg waves and the total orbital velocities of the underlying surface waves.

v. Spike calculation: Having obtained the size and the location of the breaking wave events, the MoM code is employed to calculate the cross section of the corresponding breaking wave profiles. The velocity of these events is defined as the sum of the phase velocity of the breaking waves and the total orbital velocities of the underlying surface waves.

vi. RCS combination: The Bragg and spike results are summed to obtain the full radar cross section of each part of the surface. Moreover, the final velocity is calculated as the weighed sum of the Bragg and spike velocities.

These six steps generate one time step of the seaclutter simulation. By repeating this procedure, a time series of any desired length may be generated. The so-obtained seaclutter simulation combines tilt-modulated Bragg scattering and sea spikes, and is also dynamic, which means that it satisfies the demands stated in goal 2.

The third main goal of this thesis was to validate the model through a comparison with radar seaclutter data. The data analysis required for this purpose was described in chapter 6 and also in [61]. Three sets of high resolution, coherent and polarimetric X-band radar data were analysed in a number of ways. The analysis of the data revealed that seaclutter is made up of 1) a global background caused by tilt-modulated Bragg scattering, and 2) so-called sea-spikes, caused by the semi-specular scattering on steepened and/or breaking waves. Moreover, it was found that velocity is the best tool for the physical interpretation of the data.

The process of fine-tuning and validating the model was discussed in chapter 7. The fine-tuning comprised of two main parts: spectral matching and tuning of the breaking criterion. Having fine-tuned the oceanographic part of the model, a simulated data set was obtained, which had the same form as the measured data. Therefore, the same analyses that had been performed on the measured data, were also applied to the simulated data. It was found that most of the simulation results closely matched the measurement results, but two differences between the two remained in histograms of the radar cross section. The first was a low-end tail which is a direct result of the 1D nature of the model. The second was a difference in the polarisation ratio. The model predicts, in line with literature, a much lower HH/VV ratio than the measurements show. This difference was discussed and one possible explanation, micro-breakers, was expanded upon. It was shown that inclusion of these objects could indeed raise the polarisation ratio to the measured level.

Concluding, the model presented in this thesis satisfies the goals set in chapter 1. Therefore, it contributes to radar seaclutter research by combining different oceanographic and electromagnetic models.

Dankwoord

Ik wil deze pagina gebruiken om de mensen te bedanken, die mij bij dit werk geholpen hebben.

Ten eerste wil ik mijn promotors, Piet van Genderen en Peter Hoogeboom, bedanken voor de begeleiding en hun geduld gedurende dit lange proces. Harm Greidanus heeft mij in de eerste periode goed op weg geholpen en is me vervolgens blijven begeleiden vanuit Italië. Een belangrijk deel van het proefschrift was het ontwikkelen van de MoM code, waarbij Peter Zwamborn mij geholpen heeft.

Verder wil ik TNO bedanken voor het feit dat zij dit onderzoek mogelijk hebben gemaakt en zelfs zijn blijven steunen nadat ik daar vertrokken was. Ook wil ik mijn oud-collega's daar bedanken. In het bijzonder: Ronald en Eric, jullie waren gezellige kamergenoten. Jan, onze discussies hebben mij altijd bij dit werk gestimuleerd. Arthur en Jacco, bedankt voor jullie steun en adviezen over de TU. Wim, je stond altijd open om tal van onderwerpen te bespreken en ik wil je vooral bedanken dat je mij hebt geleerd cryptogrammen te maken.

Ook wil ik mijn vrienden bedanken: je kan immers niet al je vrije tijd vullen met het schrijven van een proefschrift. Frodo, Petra, Remon, David en Vincent, bedankt voor alle gezellige (spelletjes)avonden. Vincent, onze fietstochten na het werk zijn voor mij altijd een goede manier (geweest) om stoom af te blazen.

Tenslotte wil ik ook vooral mijn familie bedanken: Piet, dank je dat je altijd voor me klaar staat, zelfs tijdens de verdediging; Zusje, de avonden met slechte films waren altijd een welkome afleiding; Pap en mam, bedankt voor jullie onvoorwaardelijke steun. Willemijn: bedankt dat je dit hele boek meermalen hebt doorgelezen. Ik ben blij dat we nu allebei eindelijk klaar zijn.

About the author

The author was born in Huissen, The Netherlands, at the 23^{th} of August 1974. Soon after he moved to Leiden, where he followed his primary and secondary (Gymnasium) education. In 1992 he started a study of astronomy at the University of Leiden. During this study he did an internship at the European Southern Observatory in La Silla, Chile. He obtained his Doctorandus (M.Sc.) degree in 1998 on the topic of the dynamics of elliptical galaxies.

At the end of 1998 he started working at TNO Physics and Electronics Laboratory (TNO-FEL) on the Ph.D. research reported in this thesis. For this Ph.D. a cooperation was set up with the Delft University of Technology, in particular with the International Research Centre for Telecommunications-transmission and Radar (IRCTR).

Subsequently, he worked at TNO-FEL as a researcher, where his work included several topics on radar propagation and detection. He is currently employed as a statistical researcher at the Central Bureau of Statistics in the Netherlands.